UC San Diego
UC San Diego Electronic Theses and Dissertations

Title
Direct electron detection in transmission electron microscopy

Permalink
https://escholarship.org/uc/item/94x000kv

Author
Jin, Liang

Publication Date
2009

Peer reviewed|Thesis/dissertation

eScholarship.org Powered by the California Digital Library
University of California

UNIVERSITY OF CALIFORNIA, SAN DIEGO

Direct Electron Detection in Transmission Electron Microscopy

A dissertation submitted in partial satisfaction of the requirements for the degree

Doctor of Philosophy

in

Physics

by

Liang Jin

Committee in charge:

Professor Xuong Nguyen-Huu, Chair
Professor Timothy S. Baker
Professor Mark H. Ellisman
Professor Melvin Y. Okamura
Professor José N. Onuchic

2009

Copyright

Liang Jin, 2009

All rights reserved

The dissertation of Liang Jin is approved, and it is acceptable in quality and form for publication on microfilm and electronically:

____

____

____

____

____
Chair

University of California, San Diego

2009

To my love, Jing Cai.

TABLE OF CONTENTS

SIGNATURE PAGE iii

DEDICATION iv

TABLE OF CONTENTS v

LIST OF FIGURES ix

LIST OF TABLES xiv

ACKNOWLEDGEMENTS xv

VITA xvii

ABSTRACT xix

Chapter 1 Background and Introduction 1

1.1 The History of Transmission Electron Microscopy 1

1.2 The recent development of Transmission Electron Microscopy 4

1.2.1 Electron Tomography 4

1.2.2 Cryo-Electron Microscopy 6

1.3 The Current Imaging Solutions for Transmission Electron Microscopy .. 9

1.3.1 Electron Micrographs (Film) 9

1.3.2 Charge-coupled Device (CCD) 11

1.4 What we need in an optimal detector for electron microscopy 14

Chapter 2 Basics of the Direct Detection Device 17

2.1 Basic Concept 17

2.1.1 Physics of charge generation in the silicon detector in general 17

2.1.2 Signal charge in the DDD 19

2.2 The Five Generations of the DDD ... 22
2.2.1 Overview ... 22
2.2.2 EM1 ... 23
2.2.3 EM2 ... 24
2.2.4 EM3 ... 25
2.2.5 EM4 ... 27
2.2.6 EM5 ... 28
2.3 Electronics and Mechanical Designs ... 29
2.4 Microscopes ... 30
Chapter 3 Experimental Results from EM3 ... 31
3.1 EM3 System ... 31
3.1.1 Readout Electronics ... 31
3.1.1.1 Timing for EM3 ... 32
3.1.1.2 Computer System ... 35
3.1.2 Mechanical Assembly and Cooling System ... 37
3.1.3 Mechanical Shutter ... 39
3.1.4 Faraday Plate (Electron Beam Intensity Measurement) ... 41
3.2 EM3 Sensor Characterization ... 44
3.2.1 Leakage Current (Dark Current) ... 44
3.2.2 Pixel Gain Variations ... 50
3.2.3 Noise in the DDD ... 51
3.2.3.1 Random Telegraph Signal (RTS) Noise ... 53
3.2.3.2 Measured Total Noise after Correction ... 55
3.2.4 Device Calibration Using X-ray Photons ... 56
3.3 Detector Responses from Beam Electrons ... 61
3.3.1 Uniform Electron Illumination ... 61
3.3.2 Single Electron Hits ... 65
3.3.3 MTF Measurements Using Edge Method ... 68

3.3.3.1 Modulation Transfer Function (MTF) 68

3.4 Radiation Damage.. 73

Chapter 4 Experimental Results from EM5.. 79

4.1 EM5 System.. 79

4.1.1 EM5 Sensor.. 79

4.1.2 Supporting Electronics Board.. 81

4.1.3 Mechanical Assembly and Cooling System 82

4.1.4 Peripheral Control Box 83

4.1.5 Computer System.. 84

4.1.6 Timing for EM5 85

4.1.6.1 Rolling CDS Mode 85

4.1.6.2 Pseudo-CDS Mode.. 87

4.1.7 Single Read Difference Mode... 88

4.1.8 Readout Frame Rate.. 93

4.2 EM5 Calibration.. 95

4.2.1 Gain and Offset Calibration for the On-chip Op Amps.................... 95

4.2.2 Leakage Current Calibration.. 97

4.2.3 Measured Total Noise after Correction... 99

4.2.4 Device Calibration Using X-ray Photons 102

4.3 Detector Responses from Beam Electrons.. 104

4.3.1 Uniform Electron Illumination 104

4.3.2 Single Electron Hits 106

4.4 High Speed 2-D Electron Counter Imaging using EM5 110

4.4.1 Optimized Operation Mode for Electron Counting 110

4.4.2 Cluster Analysis and Selection 115

4.4.3 Image Reconstruction and Super-resolution.................................... 119

4.4.4 Noise in the Final Image.. 120

4.4.5 Beam Stop Image using the Electron Counter Mode...................... 122

4.4.6 MTF Comparison 124

Chapter 5 Monte Carlo Simulation for DDD 127

5.1 Monte Carlo Approach to the Electron Transport Problem 127

5.2 Simulation for the EM5 128

5.3 Faraday Plate Simulation 131

Chapter 6 Applications of DDD 133

6.1 Image Comparison between CCD and DDD 133

6.2 Image Comparison between Integrating Imaging Method and Electron Counting Method 135

6.3 Specimen Drift Correction 137

6.3.1 Fast Wide-field Mosaic 140

6.3.2 Electron Tomography 144

Chapter 7 Summary 146

7.1 Imaging Benefits from the DDD 146

7.2 Future Improvements 147

References 148

LIST OF FIGURES

Figure 1. Different components of a modern electron microscope. 2

Figure 2. Photo of the JEOL JEM-3200EF microscope in NCMIR. 3

Figure 3. Monte Carlo simulation of the trajectories of 25 primary electrons at 120keV in a 10 µm thick P43 phosphor layer. 12

Figure 4. SEM photo of the top surface of the EM5, showing 10µm of epitaxial layer as well as nearby 10µm of the top circuitry layer. 20

Figure 5. Pixel Structure of the DDD sensor chip. 21

Figure 6. Chip layout of EM 1. 23

Figure 7. Block diagram of EM1. 24

Figure 8. Block diagram of EM2. 25

Figure 9. Chip layout of EM3. 26

Figure 10. Block diagram of EM3. 26

Figure 11. Chip layout of EM4. 27

Figure 12. Chip layout of EM5. 28

Figure 13. Block diagram of EM5. 29

Figure 14. Timing diagram showing the clocking of the first 3 rows of the sensor. 33

Figure 15. Global reset CDS mode flowchart diagram showing the readout sequence of one frame. 34

Figure 16. LABVIEW control interface for the EM3 system. 37

Figure 17. Mechanical mounting of the DDD sensor on a JEOL microscope. 39

Figure 18. The CSDA ranges for 100-400keV electrons in selected materials. 40

Figure 19. Schematic of the amplifier circuit for the Faraday plate. 42

Figure 20. Measured electron beam flux from the Faraday plate and the microscope viewing screen at 400keV on the JEOL JEM-4000 EX. 43

Figure 21. Histogram of all the pixel values in an image taken in total darkness. Only CDS subtraction was performed. Integration time was 58ms.............................. 46

Figure 22. Histogram of all the pixel values in an image taken in total darkness. Only CDS subtraction was performed. Integration time was 309ms............................ 47

Figure 23. Leakage current measurement using the most probable peak values from the histogram of pixel values in dark exposure images with different integration periods. 48

Figure 24. Temperature dependence of the measured leakage current. 49

Figure 25. Gain variations shown in the bright field image. 51

Figure 26. The readings of (a) a normal pixel and (b) a noisy pixel showing RTS noise, in 500 continuous frames. 54

Figure 27. The histogram of a dark frame after CDS subtraction and pedestal correction. 56

Figure 28. Cross sections of coherent, incoherent scattering and photoelectric absorption for silicon and photons with energies in the range of 1keV to 500keV. 57

Figure 29. The peak value histogram for events detected in EM3. The peak around 84 ADC was fitted with a Gaussian and the mean value corresponded to the 5.9keV ^{55}Fe photon calibration. 59

Figure 30. Average ADC values in the DDD detector for different uniform electron dose at 200keV. 62

Figure 31. Average ADC values in the DDD detector for different uniform electron dose at 400keV. 63

Figure 32. Average ADC values in the DDD detector for different uniform electron dose at 120keV, 200keV, 300keV and 400keV beam energy. 64

Figure 33. (a) the typical pixel readings of a single 300keV electron event and (b) the average distribution of all the detected events. 67

Figure 34. The image from EM3, showing the edge transition. Image was a 52x100 pixels crop from the original image. 69

Figure 35. Oversampled edge profile from raw data as well as the fitted edge profile using an analytical function. 70

Figure 36. MTFS curve of the EM3 at 300keV using the edge method. 71

Figure 37. MTF curves from the edge method at different incident beam electron energies. The LSF curves were fitted with a Gaussian shape, so the MTF curves in this plot were for qualitative comparison purposes only. 73

Figure 38. The increase of the leakage current at different levels of radiation. The room temperature and the low temperature results were plotted together but with different y-scales. (a) black squared at 33°C; (b) red triangles at -15°C. The lines were the linear fit to the data. 75

Figure 39. Distribution of pixel readings for single incident electron events at 300 keV (a) before and (b) after the radiation damage test. The chip was maintained at -15 °C. 76

Figure 40. Photo of the EM5 carrier board with mounted sensor chip. 80

Figure 41. Photo of the supporting electronics board with the carrier board mounted. The mechanical shutter and the copper link between the sensor chip and the water cooling pipe were marked. 82

Figure 42. EM5 vacuum interface with water cooling pipes. 83

Figure 43. Rolling CDS mode timing diagram. 86

Figure 44. Pseudo CDS mode timing diagram. 88

Figure 45. Changes in the output voltage of a specific pixel in the first and second reads of multiple frames. An incident electron hit the pixel in the 22nd frame. 89

Figure 46. Values of each frame after CDS subtraction for the same data in Figure 45. . 90

Figure 47. Single read difference values for the same pixel as shown in Figure 45. 92

Figure 48. Histogram of the gains of the per-column op amps before the on-chip ADC. 96

Figure 49. Histogram of the offset voltages of the per-column op amps before the on-chip ADC. 97

Figure 50. Histogram of the pixel values in the average image obtained in rolling reset CDS mode at -20°C. Only CDS subtraction was performed before averaging the 250 frames together. 99

Figure 51. Histogram of all the standard deviation values for all the pixels in the EM5 sensor. Data was acquired at -29°C. 100

Figure 52. Histogram of all the standard deviation values for all the pixels in the EM5 sensor. Data was acquired at +16°C. 101

Figure 53. The histogram of the peak pixels in detected ^{55}Fe X-ray photon hits. The plot on the right showed the values around the 5.9keV signal peak. 102

Figure 54. The average response of the EM5 sensor to uniform 200keV electron illumination at different intensities. 105

Figure 55. The average response of the EM5 sensor to uniform 120keV electron illumination at different intensities. 105

Figure 56. The normalized number of remaining events after filtering out the events with different threshold values, expressed in multiples of the RMS noise. 108

Figure 57. Histogram of the peak values from single electron events at 200keV. 109

Figure 58. The percentage of events with an electron nearby, in respect to the matrix size, which would be equivalent to an electron dose of 1 electron in (matrix size)^2 pixels. 112

Figure 59. Histogram of the number of pixels in each cluster, from ^{55}Fe photon data in EM5.. 116

Figure 60. Histogram of the number of pixels in each cluster, from 120keV electrons in EM5.. 117

Figure 61. Histogram of the bounding box ratios obtained from ^{55}Fe photon data in EM5. 118

Figure 62. Histogram of the bounding box ratios obtained from 120keV electrons in EM5.. 118

Figure 63. Histogram of the sum values from the 7x7 matrix around the peak pixels of detected single 200keV electron hits. 121

Figure 64. Beam stop image (top) reconstructed using electron counting method at 200keV. The histogram (bottom) of the pixel values in the image was shown at the bottom. 123

Figure 65. The line spread functions from the beam stop images using, a) integrating method, b) electron counting method. Data was taken with 200keV electrons.. 125

Figure 66. The MTF plots for both the integrating method and the electron counting. . 126

Figure 67. Electron trajectories in aluminum, with a backscattering electron in a dotted line.. 132

Figure 68. Images of myelin samples from the EM3 (top) and the Tietz 2k x 2k CCD camera (b. Both images were taken at an EM magnification of 2500 with 200 keV electron beam. 134

Figure 69. Images of the same specimen using integrating imaging method (top) and electron counting (bottom) method... 136

Figure 70. The improvement of image quality by digitally summing up more and more frames. On the first row, 1 frame, 5 frames, and 20 frames were used, and the second row was for 20, 50 and 100 frames (left to right). 138

Figure 71. Estimated specimen drift amplitudes in both x- and y- direction of the imaging sensor, calculated using normalized cross correlation applied to the averages of every 5 sequential frames. The x-direction graph shows a substantial drift over time while the y-direction graph shows only slight deviations.......................... 139

Figure 72. The mosaic image (~2k x 2k) of longitudinal mice cardiac muscle specimen from 44 individual EM3 images, taken at 2500 magnification. 142

Figure 73. The 1.5k x 3k image mosaic from 27 individual EM5 images constructed using electron counting method. 143

Figure 74. One of the 27 individual images used in the image mosaic in Figure 73...... 144

Figure 75. A central x-y slice through the reconstructed cross-sectional cardiac muscle tomographic volume. The total dose at each tile angle is <200 electrons/pixel. 145

LIST OF TABLES

Table 1. Summary of the different features of the five generations of DDD prototypes. 22

Table 2. The 7x7 average matrix from the ^{55}Fe events. 60

Table 3. The 7x7 average matrix from the ^{109}Cd events. 60

Table 4. Comparing the EM3 MTF values to the public datasheet from commercially available scientific CCD manufacturers 72

Table 5. The 7x7 average matrix from the ^{55}Fe events in EM5..................................... 104

Table 6. The 7x7 average matrix from detected 120keV single electron events in EM5. 107

Table 7. The 7x7 average matrix from detected 200keV single electron events in EM5. 108

Table 8. The 7x7 average matrix from detected 200keV single electron events using the single read difference mode. 114

Table 9. The 5x5 average matrix from the simulation results at 200keV. 129

Table 10. The 5x5 average matrix from the simulation results at 120keV. 130

Table 11. The 5x5 average matrix from the simulation results at 200keV 131

ACKNOWLEDGEMENTS

This work would not have been possible without the continuous support and guidance of Dr. Xuong Nguyen-Huu. I sincerely appreciate his attitude towards science, being enthusiastic, curious, and optimistic. I also would like to thank the members of my dissertation committee, Dr. Timothy S. Baker, Dr. Mark H. Ellisman, Dr. Melvin Y. Okamura, and Dr. José N. Onuchic, for their comments and suggestions. I am especially indebted to Dr. Ellisman, not only for use of the microscopes in the National Center for Microscopy and Imaging Research (NCMIR) where he directs, but also for his insightful suggestions over the years.

Special thanks are given to other members in our research group: Dr. Anna-Clare Milazzo, for her initial introduction to this great project and her valuable inputs in many of our discussions; Mr. Fred Duttweiler, for his discussion and support mainly on all things electronics; Mr. Philippe Leblanc, for his wonderful mechanical designs that worked so well; and Mr. Ron Quillin, for his all-mighty ability to solve electronics and computer problems. I'd like to thank Mr. Allen White from the Physics Electronics Shop for the CPLD firmware design and especially for his patience with me in the debugging process.

I would also like to express my appreciation to our collaborators at the University of California, Irvine, including Dr. Shengdong Li, Dr. Yandong Cheng, Mr. Shiuh-hua Wood Chiang, Mr. Jeff Sloan and Mr. Di Wang, from the research laboratory of Dr. Stuart Kleinfelder. I feel especially indebted to Dr. Kleinfelder who not only oversaw the

design of the sensor prototypes used in the work but also helped me understand the device characteristics.

I am also grateful to many members of NCMIR: Dr. James C. Bouwer, for his assistance on the microscope as well as his comments in many discussions; Mr. Steve Peltier, for his support and patience in proof reading manuscripts; Mr. John Crum and Mr. Mason Mackey, for microscope training and troubleshooting; Ms. Masako Terada and Mr. James Obayashi, for assistance in tomography reconstruction; Dr. Takeharu Hayashi and Ms. Andrea Thor, for providing the mouse cardiac muscle specimen; Ms. Ying Jones and Mr. Tom Deerinck, for their suggestions in specimen preparation; Tristan Shone, for designing the lead shield; Tomas Molina, for help with computer control of the microscopes; and Dr. Hiroyuki Hakozaki, for his discussion on high speed image acquisition hardware. I would also like to thank Mr. Ryan Anderson in the Nano3 facility in CalIT2 for the assistance in the SEM images; Dr. James L. Matteson and Dr. Tomas Skelton from Center for Astrophysics & Space Sciences for discussions on the radiation effects; Dr. Howard S. Matis from Lawrence Berkeley National Lab for discussions on experimental results from high energy electrons; Dr. Hans Bichsel from the University of Washington for discussions on energy straggling functions in thin silicon detectors. Finally, my sincere gratitude goes to my family and my friends who have always been extremely supportive.

Funding for the research was provided by NIH Grants RR018841 and RR004050.

VITA

2002	Bachelor of Science, Physics Nanjing University, Nanjing, China
2003	Master of Science, Physics University of California San Diego, San Diego, USA
2009	Doctor of Philosophy, Physics University of California San Diego, San Diego, USA

PUBLICATIONS

Jin L, Milazzo AC, Kleinfelder S, Li S, Leblanc P, Duttweiler F, Bouwer JC, Peltier ST, Ellisman MH, Xuong NH. Applications of direct detection device in transmission electron microscopy. J Struct Biol. 2008;161(3):352-8.

Jin L, Milazzo AC, Kleinfelder S, Li S, Leblanc P, Duttweiler F, Bouwer JC, Peltier S, Ellisman MH, Xuong NH. The intermediate size direct detection detector for electron microscopy. Proc. SPIE Int. Soc. Opt. Eng. 2007;6501:65010A.

Xuong NH, Jin L, Kleinfelder S, Li S, Leblanc P, Duttweiler F, Bouwer JC, Peltier ST, Milazzo AC, Ellisman MH. Future Directions for Camera Systems in Electron Microscopy. Methods Cell Biol. 2007;79:721-39.

Milazzo AC, Leblanc P, Duttweiler F, Jin L, Bouwer JC, Peltier S, Ellisman M, Bieser F, Matis HS, Wieman H, Active pixel sensor array as a detector for electron microscopy. Ultramicroscopy 2005;104:152-159.

CONFERENCE PRESENTATIONS

Jin L, Milazzo AC, Kleinfelder S, Li S, Leblanc P, Duttweiler F, Bouwer JC, Peltier S, Ellisman MH, Xuong NH., "Characterization of the Direct Detection Detector for Electron Microscopy", 2008 Annual Meeting of the Microscopy Society of America, Albuquerque, NM

Jin L, Milazzo AC, Kleinfelder S, Li S, Leblanc P, Duttweiler F, Bouwer JC, Peltier S, Ellisman MH, Xuong NH., "A New Direct Detection Detector for Electron Microscopy", 2007 IS&T/SPIE Electronic Imaging, San Jose, CA

Jin L, Milazzo AC, Kleinfelder S, Li S, Leblanc P, Duttweiler F, Bouwer JC, Peltier S, Ellisman MH, Xuong NH., "Direct Digital Imaging Detectors", 2006 The 4th International Congress on Electron Tomography, San Diego, CA

Jin L, Milazzo AC, Kleinfelder S, Li S, Leblanc P, Duttweiler F, Bouwer JC, Peltier S, Ellisman MH, Xuong NH., "Direct Electron Imaging for Electron Microscopy", 2005 Workshop on Advanced Topics in Electron Microscopy Structure Determination, San Diego, CA

ABSTRACT OF THE DISSERTATION

Direct Electron Detection

in Transmission Electron Microscopy

by

Liang Jin

Doctor of Philosophy in Physics

University of California, San Diego, 2009

Professor Xuong Nguyen-Huu, Chair

Since the first prototype of a transmission electron microscope was built in 1931 by Ernst Ruska and Max Knoll, Transmission Electron Microscopy (TEM) has proved to be an essential imaging tool for physicists, material scientists, and biologists.

To record the TEM images for analysis, electron microscopists have used specialized electron micrograph film for a long time, until the new developments in TEM, such as electron tomography and cryo-electron microscopy, pushed for the needs of digital imaging. Recent years has seen the widespread use of the charge coupled device (CCD) in all fields of TEM. Although it does provide digital readout, its spatial resolution and sensitivity are fundamentally limited by the use of an indirect detection method based on scintillator screens to convert high energy electrons into photons. To realize the full imaging potential of the TEM, a new imaging detector for TEM, called the Direct Detection Device (DDD), was designed, built and characterized.

The DDD is capable of directly detecting high energy electrons with a high signal to noise ratio, ensuring single electron sensitivity. Thanks to the small 5μm pixel size, the spatial resolution of the DDD exceeds any current imaging detectors in the TEM. Additionally, with the recent development of the fifth generations DDD prototype, the imaging performance of the DDD was further improved by using the DDD as a high speed 2-dimensional electron counter. The Modulation Transfer Function (MTF) of the DDD at half Nyquist frequency (50 lp/mm) reached 50% using the noiseless electron counter operation. The unique features of the DDD also enabled the possibility of specimen drift correction and fast wide-field image mosaic acquisition.

With the advantages of direct electron detection, the DDD is expected to improve the image quality and resolution of all fields of TEM, especially for low dose imaging.

Chapter 1 Background and Introduction

In this chapter, a brief history of Transmission Electron Microscopy (TEM) will be given, followed by the recent developments in TEM that have introduced the new detectors, such as the charged-coupled device (CCD) and the prototype Direct Detection Device (DDD).

1.1 The History of Transmission Electron Microscopy

In 1928, the young German scientist, Ernst Ruska, joined the cathode-ray oscillographs project, headed by the researcher, Max Knoll. By studying the high voltage cathode ray system, they came up with the idea of adapting the possible use of electromagnetic lenses to focus electron beam bundles. This idea was further developed by the group and eventually led to the first construction of an electron microscope prototype in 1931(Ruska 1987), which later won the two men the Nobel Prize in Physics in 1986.

By calculating the resolution limit for a 75keV electron beam, Earnst Ruska found out that using the "materials wave" theory of de Broglie and the Abbe's resolution limit equation, the electron microscope has a potential of reaching a resolution much higher than light microscopy. To prove this, in 1933, Ernst Ruska was able to construct a two-stage electron microscope that surpassed the resolution of the light microscopy.

Using the same electron optics idea, Max Knoll, in 1935, succeeded in obtaining an image of silicon steel showing electron channeling contrast using a scanning imaging method, which was later developed into the Scanning Electron Microscopy. To differentiate the scanning method from the original method, we use the term Transmission Electron Microscopy to define the original idea of having the electron beam passing through the specimen.

This exciting new way of imaging materials using electron optics was further developed over the years and became an essential imaging tool. The typical components of a modern electron microscope are depicted in Figure 1 (Frank 2006).

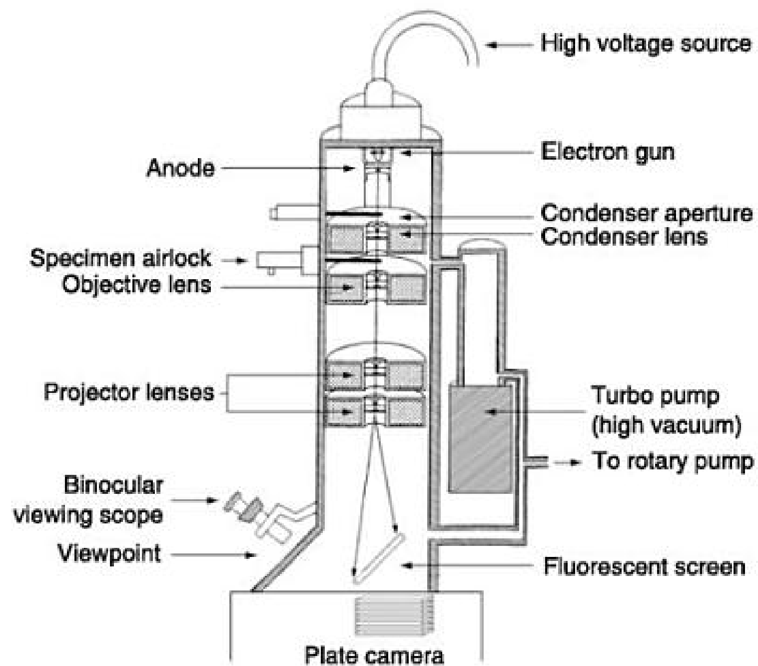

Figure 1. Different components of a modern electron microscope.

As shown in Figure 2, the electron beam is generated in the gun compartment at the top of the microscope column. Electrons emitted from the filament are accelerated by the high voltage and enter a series of electromagnetic lenses and apertures. The beam is focused on the specimen on the specimen holder in the middle of the column and the transmitted electron beam forms a final image after the projection lens and is relayed onto the viewing chamber and any imaging systems available on microscopes.

The beam energy of a modern electron microscope usually comes in the range of 120-400keV. These microscopes are mentioned as Intermediate Voltage Electron Microscopes (IVEM). Figure 2 is a photo of the JEOL 300keV IVEM in the National Center for Microscopy and Imaging Research (NCMIR) at University of California San Diego. All the experimental data from electron microscopes in the thesis were taken on the various microscopes in the facility.

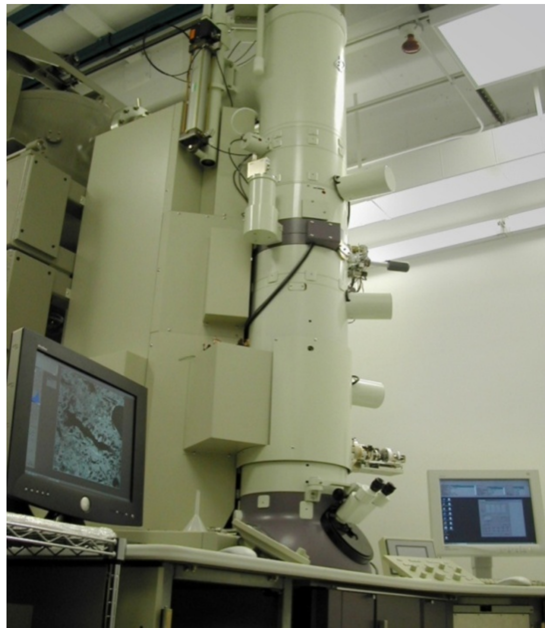

Figure 2. Photo of the JEOL JEM-3200EF microscope in NCMIR.

There are also Ultra-High Voltage Electron Microscopes (UHVEM) that have accelerating voltages up to 3 million volts. The higher energy of the electron beam provides the penetration power to use thicker specimen sections than IVEM. However, the advantages of UHVEM come at the cost of some tradeoffs, such as the complex electron optics at such a high voltage.

1.2 The Recent Development of Transmission Electron Microscopy

There are many fields in Transmission Electron Microscopy (TEM) today. For materials science and solid state physics, ultra-high speed and ultra-high resolution imaging (nano-imaging) have become very popular. However, in this thesis, we are going to focus on two of the TEM fields that are becoming extremely important to make TEM an essential tool for structural biologists. These two fields, Electron Tomography and Cryo-Electron Microscopy, are re-defining the applications of TEM in life sciences and will serve as the target for our custom designed Direct Detection Device technology.

1.2.1 Electron Tomography

Structural biology aims to understand cell structures and functions from the macro-scale of the complete organism to the mesoscale level of cells, and sub-cellular organelles, to the micro-scale of molecules, proteins and protein complexes. The interconnections of these interwoven units are of great interest to structural biologists. However, traditional TEM images are only 2D and lack the information that can be essential to understand the 3D cell structures.

Electron Tomography (Crowther, DeRosier et al. 1970; Frank 1992) opens up the opportunity of using a series of 2D TEM images to obtain 3D information from biological samples. The idea is to obtain a series of images by tilting the sample through multiple angles. The resulting tilt series are then used in a back projection calculation to mathematically reconstruct the 3D density map of the sample.

To compensate for the “missing wedge” in the 3-D Fourier space when only a single tilt angle is used for tomographic reconstruction, multiple tilt axes can be used. The most common case is to use two orthogonal axes. The tomograms computed from each tilt series can be aligned to each other and are then selectively combined to yield a single tomogram. Unlike a single-axis tomogram, a dual-axis or multiple-axis tomogram can yield good resolution in the reconstruction at any orientation in the plane of the specimen.

The electron tomography technique relies on recording many images of the same sample at different tilt angles. With a single-axis tomogram, 121 images need to be taken from -60 to +60 degrees at 1 degree intervals. Performing multiple-axis tomograms will require even more images to be taken. Therefore, the total electron dose on the sample can be quite high and the final resolution of the tomogram can be affected by the radiation damage in the specimen.

If the images were taken on film, they will need to be developed and digitized before the reconstruction step, which makes the whole process very time-consuming. The developing and digitization process could also introduce unnecessary risks if the films

were not properly handled. All in all, these features of electron tomography push for the need of a digital imaging solution.

1.2.2 Cryo-Electron Microscopy

A modern electron microscope is fully capable of reaching atomic resolution on suitable non-biological specimens. For example, the plane spacing of 0.204nm, 0.143nm and 0.102nm in a single crystal gold foil specimen can be observed on a well-aligned high resolution Transmission Electron Microscope. However, biological materials are much more difficult to image. First of all, unlike the gold foil specimen, the biological specimen is subject to substantial radiation damage in the high energy electron beam and could change part of its structure over time. Secondly, the atoms and molecules in a biological specimen are much lighter in atomic weight than heavy-metals commonly found in materials science specimens and therefore produce much lower imaging contrast. One way to boost the contrast is to prepare the specimen by staining with a heavy metal salt, which can also provide some radiation stability.

The tradeoff of the staining method is that it limits the amount of details that can be obtained. It is well-suited if the targeted resolution or the resolution of the region of interest is in tens of angstroms or larger, but it is not possible to get closer to atomic resolution.

The introduction of cryo-electron microscopy in the late 1980s brought the resolution of particular specimens, such as viruses and ribosomes, to a level that certain structural features can be seen (Speir, Munshi et al. 1995; Bottcher, Wynne et al. 1997;

Frank, Penczek et al. 2000; Thuman-Commike and Chiu 2000). The cryo-electron microscopy (cryo-EM) sample preparation technique freezes an unstained sample in a very rapid process, allowing the water molecules only to form amorphous vitreous ice, therefore preventing the crystallization of water that can damage the structures of the specimen. The frozen specimen embedded in the solid vitreous ice is then inserted into a special holder that can maintain the low temperature of the specimen. To image the sample, only a low dose of electrons is allowed, as the induced electron beam will damage the specimen. The resulting images from cryo-EM samples contain very little information on their own as the contrast is extremely low due to the low dose condition and the weak inherent contrast from the specimen. However, with the assumption that the specimen contains a large number of identical copies of the specimen and they are frozen in random orientations, it is possible to average and reconstruct a 3-D density map of the specimen using extensive computer processing on the individual 2-D images.

While protein X-ray crystallography is still the premier method to determine the 3D structures of large proteins and viruses, cryo-electron microscopy is gaining more and more popularity in recent years. The advantage of cryo-EM over protein crystallography is that it does not depend on growing large crystals, a very time consuming and, in many cases, impossible task. Its main drawback however is the low resolution of the structures obtainable. For virus particles, cryo-EM can yield a resolution < 4 Å, while for a large protein complex such as the ribosome the cryo-EM resolution is < 10 Å range. Even at the 10 Å level, cryo-EM has proved to be extremely useful for structural biologists, as the level of details can still provide enough information to answer questions about the

structural changes that can happen in a dynamic process. Because it does not require growing crystals, cryo-EM has a drastically higher throughput than protein crystallography. With cryo-EM, it is now possible to obtain the structures for intermediate protein products in a dynamic process within a reasonable time frame. One such example is the study of the "Maturation Dynamics of a Viral Capsid" (Lata, Conway et al. 2000), where the determination of molecules associated with some key stages were obtained using cryo-EM.

By docking the 2-3 Å structures of subunits obtained using protein crystallography into the 10-20 Å density maps from cryo-EM, even more information can be learned from the structures of the large molecule complexes. And this powerful combination will continue to shed new light on the mechanism of the molecular machinery in the cell.

Cryo-EM would surely be more useful if it could yield higher resolution structures, closer to the protein crystallography resolution of 3Å. However, there are two main limitations:

First, the frozen specimen needs to be stable enough for imaging in order to yield high resolution details, and the imaging condition of the electron microscope also creates radiation damage in the specimen that can make the structures intrinsically unstable and eventually damage the specimen after an accumulated dose of 10-20 electrons/Å^2. New generations of electron microscopes tackle the stability issue by dedicated low temperature stages, which hold the specimen at either liquid nitrogen or liquid helium temperatures. And limiting the imaging acquisition to the 10-20 electrons/Å^2 dose also

helps to reduce the damage. At such a low dose, the acquired images have very low contrast.

Secondly, the averaging of individual images is essential to the final resolution obtainable by cryo-EM. The estimated number of individual particle images that are needed to reach a sub-10 Å resolution can well be in the range of 10,000 to 1,000,000 (Henderson 2004). It is possible to use film for the purpose (assuming several hundred particles per micrograph, we will need at least 100 micrographs to get 10,000 particles), but it can be very time-consuming. It would be a much easier solution if a digital imaging solution can be used instead.

1.3 The Current Imaging Solutions for Transmission Electron Microscopy

1.3.1 Film

From the early times of the electron microscopy, film has been used for recording the electron images in TEM.

The emulsions of the TEM film are essentially suspensions of silver halide grains in a gel, supported on a polymer film (such as the 0.178mm thick polyester film used in KODAK Electron Microscope Film 4489). The high energy electrons in the TEM strike the halide, ionize it, and transform it to silver, which can be developed and processed later on using chemicals in the dark room.

The film grains are typically <1µm in size. The finest film grains offer the best spatial resolution, but need longer exposure time. The full size of the TEM film is

approximately 8.25cm x 10cm. Considering the nonlinear response of a single film grain (it cannot distinguish multiple electron hits from a single electron hit), more than one silver grain will be needed to produce pixel information with certain dynamic range in the final image. Multiple layers of emulsions can be used to help increase the dynamic range, but the total range is still limited and the responses to incident electrons are nonlinear. The TEM films are normally scanned and digitized at a resolution better than 20 μm per pixel, to extract all the information.

While film does provide a good spatial resolution and contrast, the requirements of chemical developing and post processing steps (such as scanning) limit its application in the new fields of electron tomography as well as in cryo-electron microscopy, since most of these techniques can benefit a lot from a high throughput digital recording solution.

1.3.2 Charge-Coupled Device (CCD)

A standard detector option commonly used instead of film is the direct digital readout, charged coupled device (CCD), which started to be used in electron microscopy in the late 1980s (Spence and Zuo 1988; Aikens, Agard et al. 1989; Chapman, Craven et al. 1989; Krivanek, Mooney et al. 1991). CCD systems have enabled the immediate access to images in real-time, and have significantly increased efficiency and throughput in the electron microscopy field. CCD systems also surpass film in many major aspects, including sensitivity, linearity and dynamic range (Fan and Ellisman 2000).

Each pixel in the CCD array is essentially a small ionization chamber that can integrate the signal charges and store in its capacitor. At the completion of a frame, to read out the pixel array, control signals transfer the signal charge in each pixel one by one to its neighbor in the same column. At the end of each column, an output register holds the signal charge from the current pixel from that column. The charges in the output registers are then transferred one by one to the output amplifier (there can be more than one amplifier to speed up the readout). This process is repeated until all the pixels in the sensor array are read out.

Due to radiation damage and charge saturation, the CCD sensor cannot be used in the direct beam path in electron microscopes (Roberts, Chapman et al. 1982). A phosphorescent scintillation screen is thus needed to convert the electron image to a photonic image, which is then relayed to the CCD cameras for image acquisition. The thickness of the scintillation layer determines how many photons will be created for each incident beam electron. Thicker scintillation layers will produce more photon signals but it will also introduce more lateral scattering by the incident electron as well as the secondary electrons and light scattering in the scintillation layer, which makes the spatial resolution worse. On the other hand, depending on the quantum efficiency of the CCD cameras and the relay method from the scintillation screen to the CCD, a number of photons will be lost during the process, and to achieve a useful signal to noise ratio, the thickness of the scintillation screen cannot be too thin (Fan and Ellisman 1996).

With an optimized scintillation screen based on the tradeoffs outlined above, a scintillation layer of around 10-20 microns is typically used. With each beam electron

event, the "spot" created within the scintillation screen is measured to be around 60 microns (full width at half maximum) in the phosphor at 120 keV beam energy (Faruqi and Andrews 1997). As shown in the Monte Carlo simulation in Figure 3 with 25 primary electron trajectories in 10 microns of P43 phosphor layer, the lateral scattering of the primary electron is only a few microns, which indicates the secondary electrons and light scattering in the phosphor screen dominate the scattering that broadens the spot to nearby 60 microns. With the CCD cameras having a typical pixel size of 15 - 25 microns, a tapered fiber optics or demagnification lens optics is needed to de-magnify the scintillator image to match the pixel size of the CCD cameras. As a side note, film emulsion layers are typically also around 10-15 μm thick and do not suffer the lateral scattering as badly as the scintillation screen does. Therefore, in terms of spatial resolution, film has an edge over the current CCD systems.

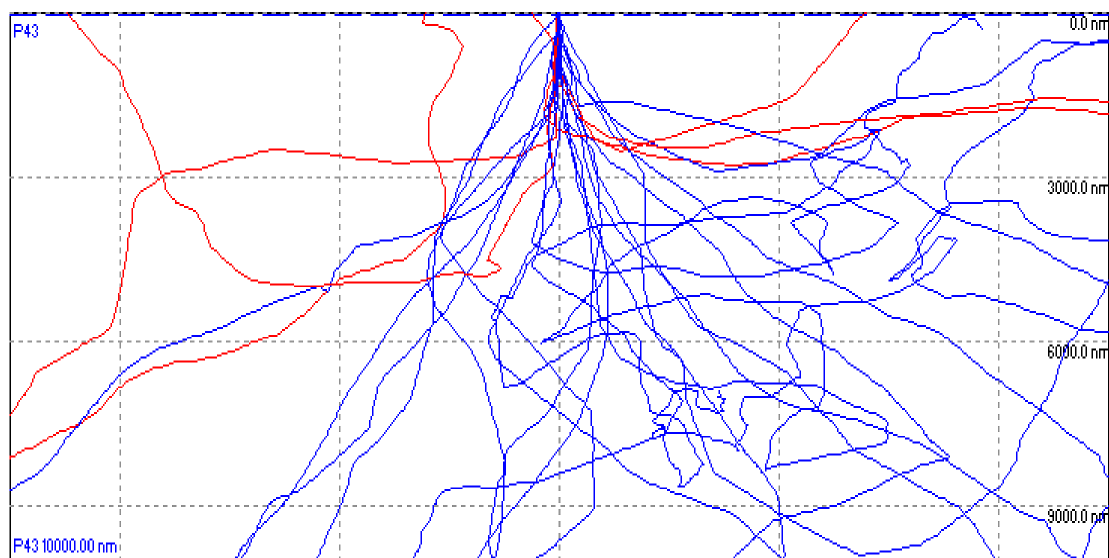

Figure 3. Monte Carlo simulation of the trajectories of 25 primary electrons at 120keV in a 10 μm thick P43 phosphor layer.

With tapered fiber optics, large spatial distortions and non-uniformities are introduced that are difficult to fully correct in post-processing. With demagnification lens optics, the poor coupling efficiency dramatically reduces the number of photons reaching the CCD, which would limit the signal-to-noise ratio of the system even when costly high quality optics and high efficiency back-thinned backside-illuminated CCDs are being used.

The scintillation screen based CCD system offers a decent digital imaging solution that is quite successful in the applications in electron microscopy, especially in electron tomography and cryo-electron microscopy where digital imaging is a necessity for high throughput. However, the fundamental properties of the scintillator screen limits the ultimate spatial resolution that can be achieved in the system, and that is why we have pursued an alternative imaging solution that can eliminate the scintillation screen altogether and achieve higher performances that are not possible with the current CCD systems.

1.4 What We Need in an Optimal Detector for Electron Microscopy

To summarize this chapter, a wish list is compiled to outline the requirement for an optimal imaging detector for electron microscopy. The list is intended to provide some guidelines to better understand the limitations of current imaging solutions.

Digital Imaging

From the applications in electron tomography and cryo-electron microscopy, a digital imaging solution is very important. Digital readout will open up many new

possibilities and is likely to further develop electron microscopy into an even better technology. The Telemicroscopy developed in NCMIR is one of the many examples of how digital imaging is helping microscopists to do what they can never achieve using film. With Telemicroscopy, the user not only can remotely control electron microscopes thousands of miles away over the computer network, but can also see near real-time images of the sample in the remote microscope from the CCD camera, so that the user can choose the region of interest and acquire images.

High Sensitivity

The sensitivity of the detection system is essential for low dose imaging. An ideal imaging solution would be able to utilize every single beam electron in the electron image to form the final image. The sensitivity of the system can be quantified in terms of the detection efficiency and signal to noise ratio. Here, the gain in signal to noise ratio of the system is usually tied with tradeoffs in the spatial resolution.

High Spatial Resolution

The electron image that is formed by the beam electrons after passing through the specimen layer and the magnetic lens system contains spatial information at different frequencies. The resolving power of an ideal imaging solution will need to distinguish not only the low frequency structures but also the high frequency details from the electron image. Because of the finite pixel size, the spatial resolution at any detector is limited by the sampling spacing or the pixel size (unless super-resolution methods can be applied). However, one will need to consider the pixel crosstalk effect coming from charge spread

in the imaging system as well to determine the true spatial resolution. A common method to quantify the spatial resolution is to measure the Modulation Transfer Function, which is explained in detail in section 3.3.3.

Because the imaging devices are mounted at the very end of the electron optics, the electron image from the specimen is actually magnified to a certain ratio. With a magnification of 10,000, a spacing of 2Å on the specimen translates to 2μm at the imaging plane. Increasing the magnification to 100,000 would make that spacing 20 μm at the imaging plane. If we don't consider imperfections in the electron optics, using a magnification of 10,000 or 100,000 would make no difference in terms of the imaging details in the final image, but at the imaging plane, a spacing of 2μm is much harder to resolve than a spacing of 20μm. To fully understand why it is necessary to optimize the imaging system to detect high frequency details even at lower magnification, we will have to look at the field of view and total pixel count.

Wide Field

The real problem of imaging at very high magnification lies in the fact that the imaging area is limited at the imaging plane. With higher magnification, the electron image becomes so large at the imaging plane that only a portion of it can be imaged at a time. Wide field of view is a feature that is important for most electron microscopy fields. It is especially important in electron tomography where a wider field of view will benefit the studies of the large 3-dimensional ultra-structure of tissues, cells and macromolecules (McEwen and Frank 2001). For single particle cryo-electron microscopy, wide field imaging can help to increase the number of single particles on a single image, thus

reducing the number of total images to take. For cryo-electron microscopy of 2-dimensional crystals, wide field imaging would allow more averaging to be done in each image thus improving the resolution of the final reconstruction.

Chapter 2 Basics of the Direct Detection Device

In pursuit of a better digital imaging solution for Transmission Electron Microscopy, we have been developing the Direct Detection Device (DDD) for the past few years(Xuong, Milazzo et al. 2004; Milazzo, Leblanc et al. 2005; Jin, Milazzo et al. 2007; Xuong, Jin et al. 2007; Jin, Milazzo et al. 2008).

In this chapter, the fundamentals of the DDD will be outlined along with a development roadmap for the five generations of the DDD prototypes.

2.1 Basic Concept

2.1.1 Physics of Charge Generation in the Silicon Detector in General

Once the high energy electron (usually in the range of 120-400keV in transmission electron microscopy) enters any medium, it will interact with the medium in one of the following ways:

Elastic scattering: the trajectory of the beam electron is changed but the energy it carries remains unchanged. Elastic scattering is caused by the interaction between the negatively charged beam electron and the positively charge nucleus in the medium.

Inelastic scattering: both the trajectory and the energy of the beam electron can be changed during inelastic scattering. The causes of the energy loss can be quite complicated, and the most common ones include: the incoming electron knocks out an inner-shell electron and causes emission of a characteristic x-ray or an ejected Auger

electron (ionization electron); the incoming electron can also produce a secondary electron if it knocks out an outmost-shell (valance) electron; the incoming electron can also interact with the crystal lattice and generate phonons.

Bremsstrahlung emission: the de-acceleration of the charged beam electron in the field of the atoms will emit Bremsstrahlung radiation. The Bremsstrahlung photon emitted can carry an energy from 0 to the total energy of the incident electron.

Depending on the thickness of the medium, the beam electron can undergo a large number of interactions before losing all of its energy or exit the surface of the medium. The secondary electrons or X-ray photons generated by the beam electron are also likely to interact with the medium in similar fashion before coming to a stop or leaving the medium.

In silicon detectors, the charges that can be collected are the ionization electrons produced in the sensing volume. The contributions to the total number of ionization electrons will come from the beam electrons as well as the secondary electrons and the X-ray photons.

Energy conservation rules indicate that the total energy of the ionization electrons will be equal to the total energy loss of the beam electron, if all the secondary electrons or X-ray photons are absorbed in the medium. Therefore, the higher the energy loss of the incident beam electron in the sensing volume, the more ionized electrons will be collected in the silicon detector.

2.1.2 Signal Charge in the DDD

The DDD is based on Monolithic Active Pixel Sensor (MAPS) technology that was originally designed for high energy particle physics(Claus, Colledani et al. 2001; Turchetta, Berst et al. 2001), but is optimized for Transmission Electron Microscopy.

The DDD sensor is fabricated in standard Complementary Metal–Oxide–Semiconductor (CMOS) process. The device can be divided into three major regions. At the very top of the surface is the circuitry layer that has pixel transistors and photodiode as well as interconnects between all the components (metallization layers). The middle layer is a p-epitaxial layer (about 8 to 10μm thick) that is epitaxially grown with very low defect levels and highly doped. The rest of the 300μm silicon substrate is used mainly for mechanical support.

Since the epitaxial layer is rather thin, most of the incident high energy beam electrons will pass through that layer, generating many ionized electrons along the path. The lack of a bias voltage means that the depletion region around the center diode is very thin and the device relies on the collection of ionized electrons in the epitaxial layer that diffuse to the diode in a certain collection time. On average, a single incident electron of 200 keV will generate about 2000 ionization electrons in the 10μm epitaxial layer, which is significantly larger than the noise level of the device (less than 50 electrons). Each pixel integrates the collected electrons during an exposure period and at the conclusion of a frame, the contents of the sensor array are read out, digitized and stored.

To determine the thickness of each of the layers in the DDD, we have broken a sensor (EM5) in half and looked at the cross section under a Scanning Electron Microscope (SEM). Figure 4 shows the top surface of a DDD sensor, and the epitaxial layer is measured to be 10μm, while the top circuitry is also measured to be around 10μm. The boundary between the epitaxial layer and the substrate can be seen because the two layers have different doping levels that affect the surface structure.

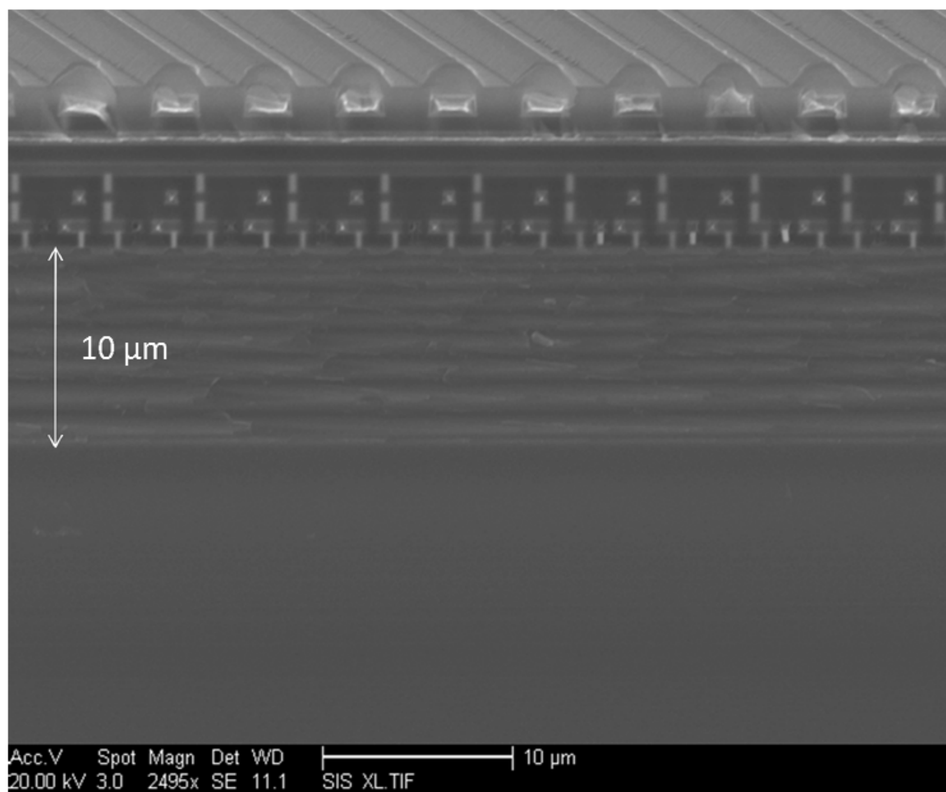

Figure 4. SEM photo of the top surface of the EM5, showing 10μm of epitaxial layer as well as nearby 10μm of the top circuitry layer.

Selective region Energy Dispersive X-ray Spectroscopy (EDS) at the top circuitry layer showed that aluminum, silicon and oxygen are being used. The aluminum is used

for conducting and interconnection between components and the silicon dioxide is used as insulation. EDS in the epitaxial layer and the substrate showed mostly traces of silicon, as the dopant concentration is relatively low compared to the silicon in the layer.

Please note that the thickness of each layer and its composition will serve as the foundation for the Monte Carlo simulation of the DDD to be described in Chapter 5.

2.1.3 DDD Pixel Structure

The DDD pixels use the three transistor design, as shown in Figure 5. The n-well photodiode in the center of the pixel collects the signal charge and forms a voltage signal at the buffer transistor (source follower), and the “row select” transistor is a switch that controls which pixels are connected to the column registers for read out. The accumulated charge in the photodiode will only be cleared out when the “reset” switch is activated and the pixel is then ready for the next frame.

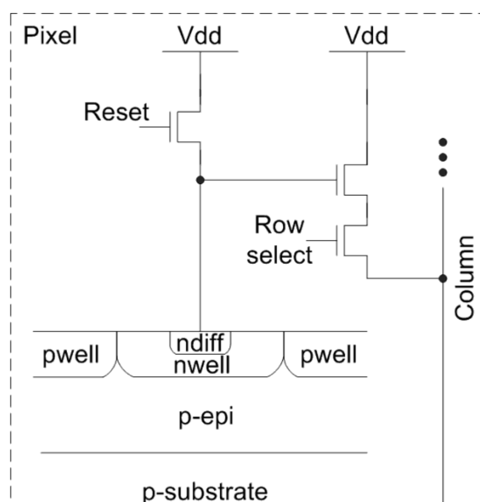

Figure 5. Pixel Structure of the DDD sensor chip.

2.2 The Five Generations of the DDD

In collaboration with Professor Stuart Kleinfelder's group in University of California, Irvine, a total of five generations of the DDD have been designed, fabricated and tested.

2.2.1 Overview

The basic features of all five generations of the DDD sensor are outlined in the Table 1, while the details of each generation are described in the following section.

Table 1. Summary of the different features of the five generations of DDD prototypes.

	EM1	EM2	EM3	EM4	EM5
Pixel Pitch	20 μm	5,10,20,30 μm	5 μm	5 μm	5 μm
Array size	128x128	360x360,180x180,45x45,30x30, respectively	550x512	1024x1024	560x460
Output	1 Analog	1 Analog	4 Analog	16 Analog	20bit Digital
Feature	4 quadrants	4 different sectors	Reasonable Imaging format	Large imaging format	Per-column ADC on-chip

2.2.2 EM1

EM1 is the first generation DDD sensor chip, aiming to explore the effects of different diode sizes. As shown in the layout (Figure 6) as well as the schematic (Figure 7), the pixel arrays consist of four sectors, with 20 μm pixel pitch. The difference between different sectors lies mainly in the size of the diode area: (a) sector 1: minimum size nwell/p-epi photodiode; (b) sector 2: medium size nwell/p-epi photodiode; (c) sector 3: large size nwell/p-epi photodiode; (d) sector 4: large size nwell/p-epi photodiode with additional capacitance between photodiode cathode and the ground.

The chip was fabricated using TSMC 0.5 μm CMOS process.

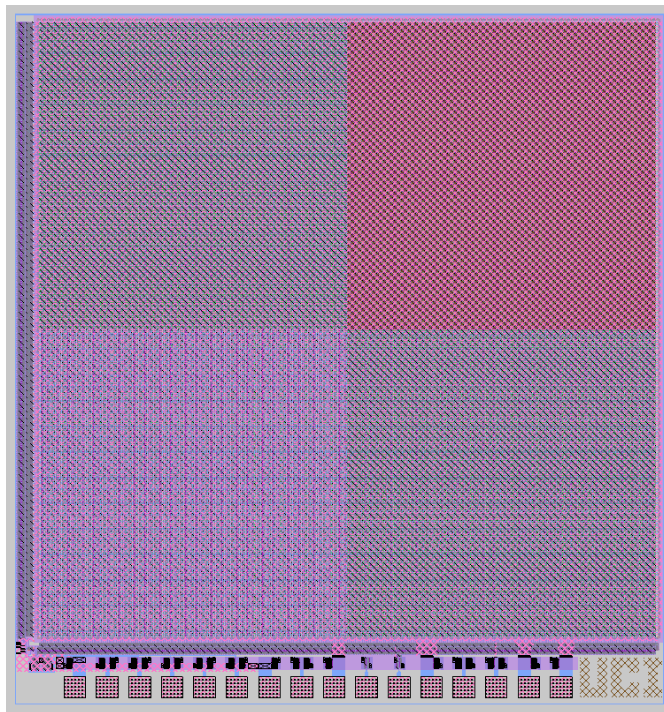

Figure 6. Chip layout of EM 1.

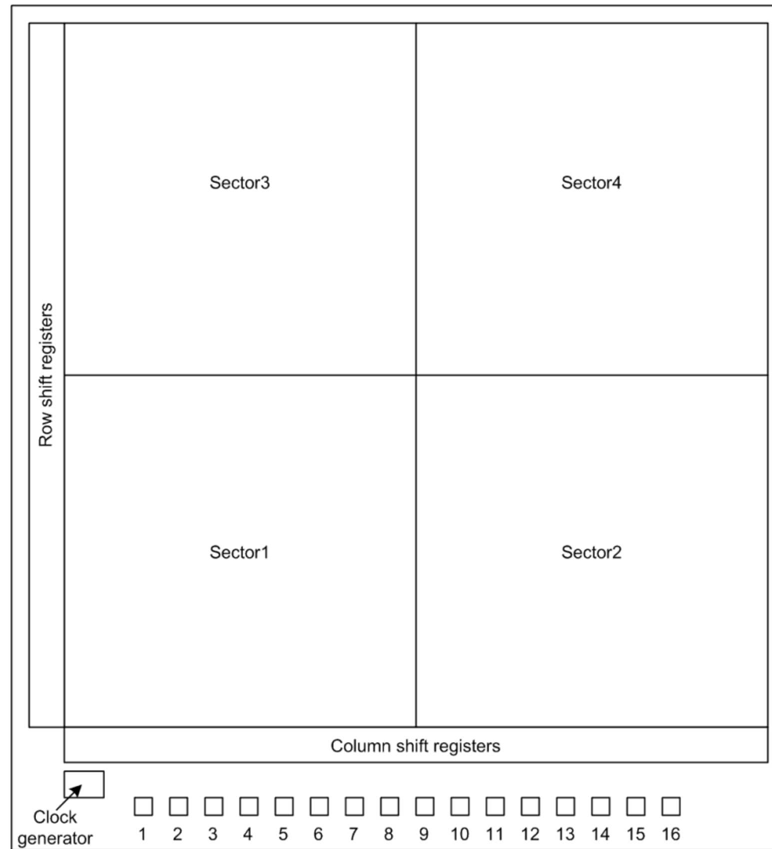

Figure 7. Block diagram of EM1.

2.2.3 EM2

EM2, the second generation DDD sensor, consists of 4 sub-regions with different pixel sizes, ranging from 30 μm to 5 μm pixel pitch. Its block diagram is shown in Figure 8. The 5 μm region has 360 x 360 pixels, the 10 μm region has 180 x 180 pixels, the 20 μm region has 45 x 45 pixels, and the 30 μm region has 30 x 30 pixels.

The sensor was fabricated in TSMC 2.5V 0.25 μm process.

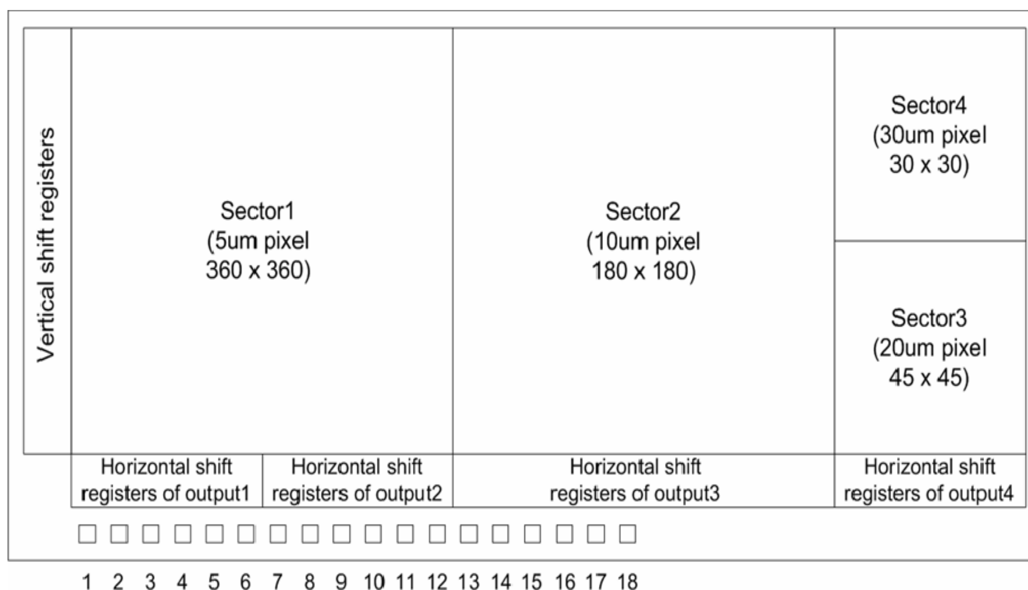

Figure 8. Block diagram of EM2.

2.2.4 EM3

EM3, a third generation DDD sensor, consists of 512 x 550 pixels with 5 µm pixel pitch and the entire area of the chip is 3002 µm x 3156 µm.

As shown in the layout (Figure 9) and block diagram (Figure 10), the pixel array is divided into 4 sectors, 128 x 512 pixels each for parallel and faster signal output (analog). Each sector has its own output bias.

The sensor was fabricated in TSMC 2.5V 0.25 µm process.

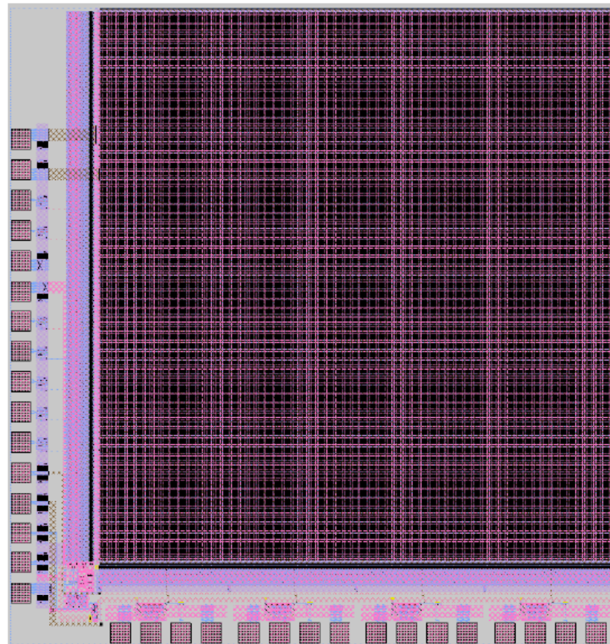

Figure 9. Chip layout of EM3.

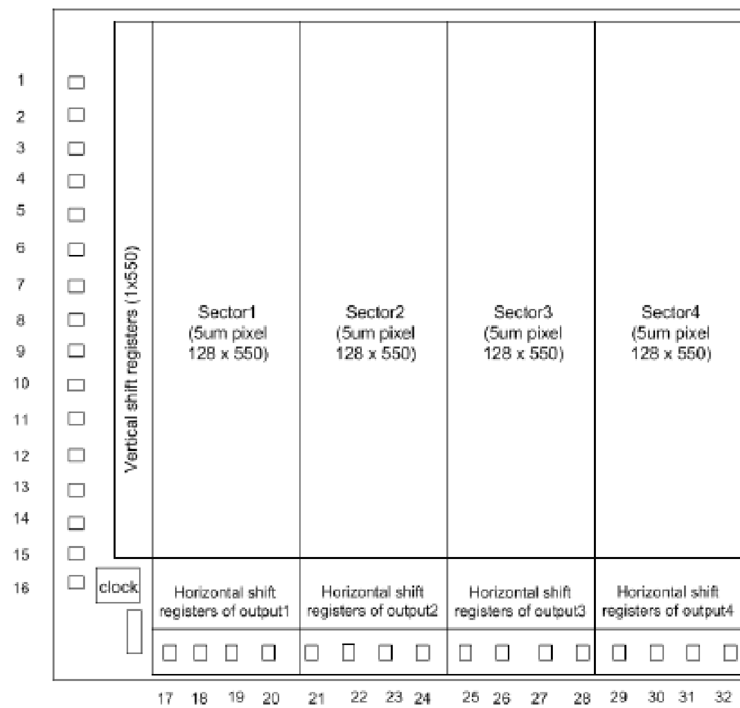

Figure 10. Block diagram of EM3.

2.2.5 EM4

EM4, a fourth generation DDD sensor, consists of 1024 x 1024 pixels with 5 µm pixel pitch and the entire area of the chip is 5540 µm x 5510 µm.

As the layout (Figure 11) shows, the pixel array is divided into 16 sectors 64x1024 pixels each for parallel and fast signal outputs. The outputs are 16 unity gain buffers, corresponding to each sector. The sensor was fabricated in TSMC 2.5V 0.25 µm process.

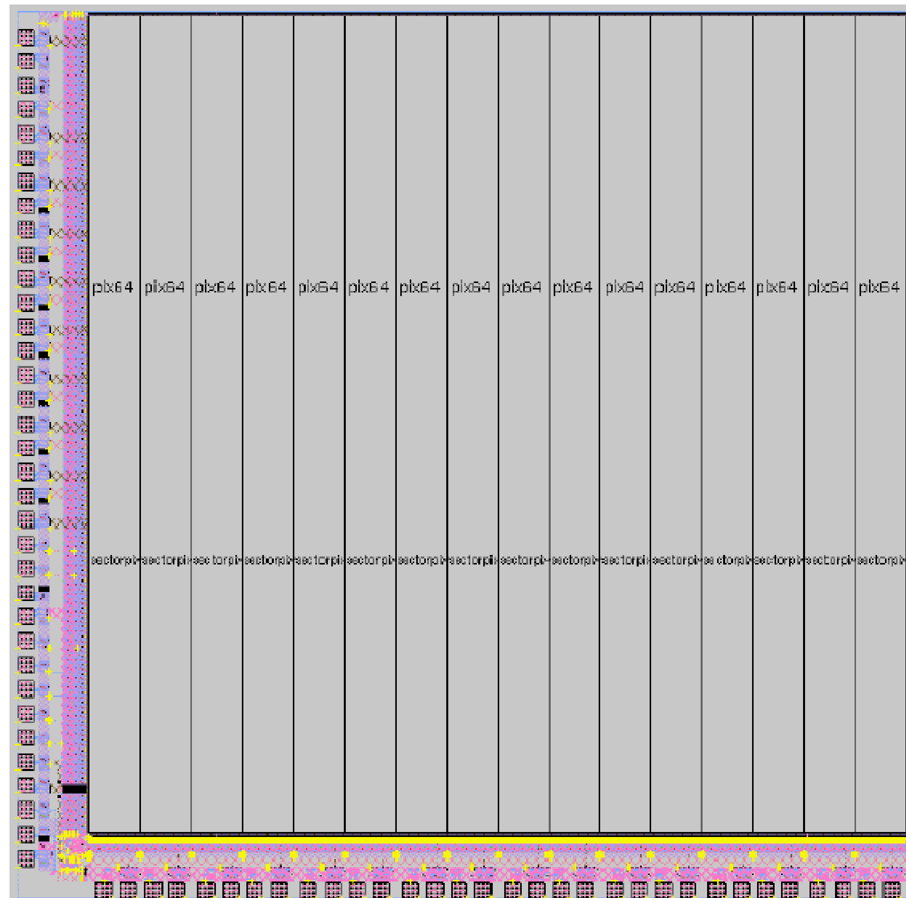

Figure 11. Chip layout of EM4.

2.2.6 EM5

EM5, a fifth generation DDD sensor, consists of 560 x 460 pixels with 5 μm pixel pitch and the entire area of the chip is 3055 μm x 4812 μm.

The EM5 is the first DDD sensor to feature column level charge amplification and analog to digital conversion on the chip. The operation of the amplifier can be changed using control signals. A 10-bit single slope ADC is designed on this chip to convert analog signal into digital output for each column. As shown in the layout (Figure 12) and block diagram (Figure 13), the ADCs are on two sides.

The sensor was fabricated in TSMC 2.5V 0.25 μm process.

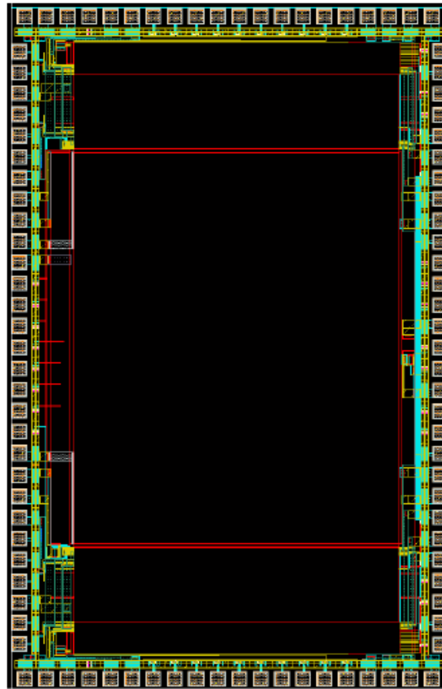

Figure 12. Chip layout of EM5.

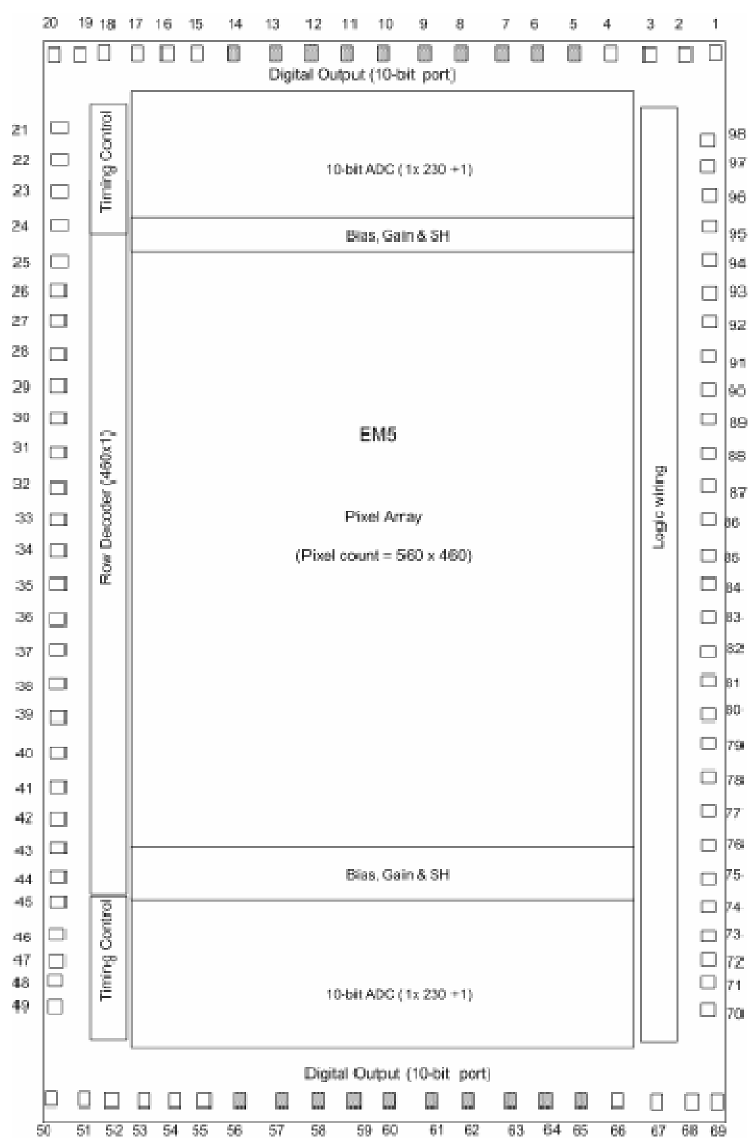

Figure 13. Block diagram of EM5.

2.3 Electronics and Mechanical Designs

All five generations of DDD sensor prototypes are custom designed and fabricated, and thus require dedicated electrical and computer support systems. The EM1 and EM2 sensors were mounted and tested using supporting electronics and computer

programs from Lawrence Berkeley National Laboratory. Since EM3, our group in UCSD has taken over the development of the electronics and computer programming development. The details of EM3 and EM5 systems can be found in the following chapters, and for the details of EM4 system, please refer to the thesis from Anna Milazzo.

To test the DDD on the electron microscope, dedicated mechanical mounting systems were designed and fabricated, and they have been improved over the five generations of DDD into a much improved version.

2.4 Microscopes

Here is a list of the microscopes used for the characterization of the DDD, all of which are located in the National Center for Microscopy and Imaging Research (NCMIR) at University of California San Diego:

1. JEOL JEM-1200 (Maximum operation voltage: 120kV)
2. JEOL JEM-2000 FX II (Maximum operation voltage: 120kV)
3. JEOL JEM-4000 EX (Maximum operation voltage: 400kV)

Chapter 3 Experimental Results from EM3

The EM1/EM2 prototypes provided the initial proof-of-concept results for direct electron detection possibilities offered by the Active Pixel Sensor technology (Xuong, Milazzo et al. 2004; Milazzo, Leblanc et al. 2005). The custom-designed EM3 with 5 μm pixel size was the first prototype to provide in-depth characterization of the DDD for real-world imaging conditions. In this chapter, the experimental results obtained from the EM3 system will be presented.

3.1 EM3 System

At the core of the EM3 system is the third generation DDD prototype sensor chip, which was described in Chapter 2. However, the readout electronics, mechanical and cooling systems and the computer system are also essential components of the entire EM3 system. This section is dedicated to the supporting peripherals that we designed around the EM3 sensor chip.

3.1.1 Readout Electronics

An EM3 supporting electronics board was custom designed with the following functions:

1. Provide power and timing controls to run the EM3 sensor chip. All clocks were controlled by a Complex Programmable Logic Device (CPLD) from Lattice Semiconductor Corporation with custom firmware.

2. Digitize the four analog outputs from the EM3 sensor chip using four 12-bit Analog-to-Digital Convertors (ADC).

3.1.1.1 Timing for EM3

To read out the entire EM3 sensor array, proper clock timing needs to be generated.

In order to reduce the reset noise in the sensor as well as eliminate the fixed pattern noise, we used the Correlated Double Sampling (CDS) method. For any given pixel, after a pixel reset (the signal charge in the photodiode was cleared out), the analog output voltage of the pixel was sampled twice. Here, the source follower buffer design inside the pixel structure allows sampling the voltage of the photodiode to be non-destructive. The difference between the two reads constitutes a CDS read, which corresponds to the signal charge that was collected in the photodiode after the first sampling and before the second sampling. The CDS subtraction corrects for the voltage level differences between the pixels as well as cancels out the random injected charge that is associated with the pixel reset since the two reads were associated with the same reset.

The CDS method outlined above is for single pixel operations, and for the entire sensor array, we used a Global Reset CDS mode in EM3. All the pixels were reset at once, followed by the readout of the entire array in a row by row fashion. The second CDS read of the sensor was performed after a programmable delay, which was used to

control the exposure time. After the completion of the second read, the sensor array was reset again and the readout cycle repeated.

Figure 14 shows the typical timing diagram for the global reset mode. The reset line was pulsed first for a duration of 20μs to 2ms. The row clock (rck) activated the readout of individual rows and the column clock (cck, pixel clock) connects each column output to the analog outputs of the sensor.

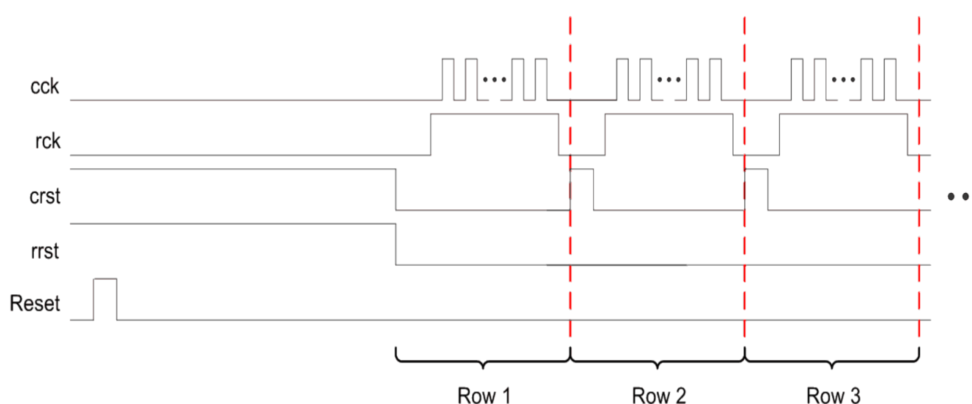

Figure 14. Timing diagram showing the clocking of the first 3 rows of the sensor.

This process was repeated from the first row to the last row in the array, which formed the first readout of the entire array. On the completion of the first read, a programmable delay was asserted, before the second readout starts. The reset line was held low during both the first and second reads, and it ensured that the signal charge in the photodiode was accumulating. The entire process is outlined in Figure 15. The subtracted values between the first and second reads would form the final CDS frame.

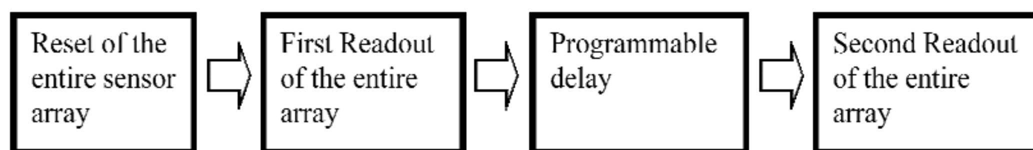

Figure 15. Global reset CDS mode flowchart diagram showing the readout sequence of one frame.

The effective integration time or the exposure time during the Global Reset CDS readout is equal to the read time of the whole sensor array plus the programmable delay between the CDS reads. If we bypassed the programmable delay altogether, the minimal integration time is then simply equal to the time it takes for a single read. In the case of EM3, the read time is 58ms.

There is actually a problem with the global reset mode, which relates to the sensor dead time. The dead time can be defined as the time that the electron beam is illuminating the sensor but the signal is not contributing to the final image acquired. In the global reset CDS mode, all the pixels are illuminated by the electron beam continuously. After the global pixel reset, all the photodiodes start to collect signal charges. However, the pixels are read out row by row, which means that the last row of pixels need to wait until all the previous rows are completely read out. When it finally comes to the last row of pixels, they have already accumulated a certain amount of signal charges in the photodiode. In the CDS subtraction, the accumulated charges in the photodiode before the first readout are cancelled out. Similarly during the second readout, the other rows of pixels have to wait until the last row of pixels are completely read out before they are reset and prepared for the next frame. Therefore, the dead time associated with each CDS frame is equal to

the time it takes for one complete read out. In the worst case scenario of bypassing the programmable delay between the two CDS reads, the dead time becomes as long as the effective integration time, which means that the sensor dead time is 50% in the worst case.

Considering the fact that the electron beam is not only illuminating the sensor but also the specimen, the dead time increases the total dose on the specimen unnecessarily. As many biological samples are vulnerable to the radiation damage by the electron beam, this problem could limit the application of the DDD. To solve this issue, a new mode of operation was designed in the EM5, and will be presented in the next chapter.

3.1.1.2 Computer System

The four analog outputs of the EM3 sensor were digitized by the supporting electronics board and the digital signal was then relayed to the Digital Input / Output (DIO) acquisition board NI-PCI-6534 from National Instruments. The ADC on the supporting board converted the sensor analog output voltages into 12-bit of data for each pixel. As the DIO board can only accept at most 32 bit in a single trigger, 2 pixels (24 valid bits) were transferred with a single trigger clock.

The DIO board was controlled on the PC by a custom program written in LABVIEW language from National Instruments. Figure 16 shows the user interface of the program. The main features included:

1. Real-time acquisition and display of an individual frame or summed image from multiple frames. Dark frame can be acquired and corrected before the image display.
2. Configuration for timing controls, including changing the digitization rate, reset pulse duration and the time delay between the two CDS reads.
3. Data streaming to hard drive for multiple frames, up to 2000 frames in a single trigger. The resulting frames were stored in a single binary file, with embedded header with text information for the configuration settings used during the acquisition.
4. Continuous triggering of the system to acquire multiple files automatically without user intervention.
5. Loading and viewing data files previously acquired.

The binary file embedded with text header information was later processed by a set of MATLAB scripts for further analysis and processing.

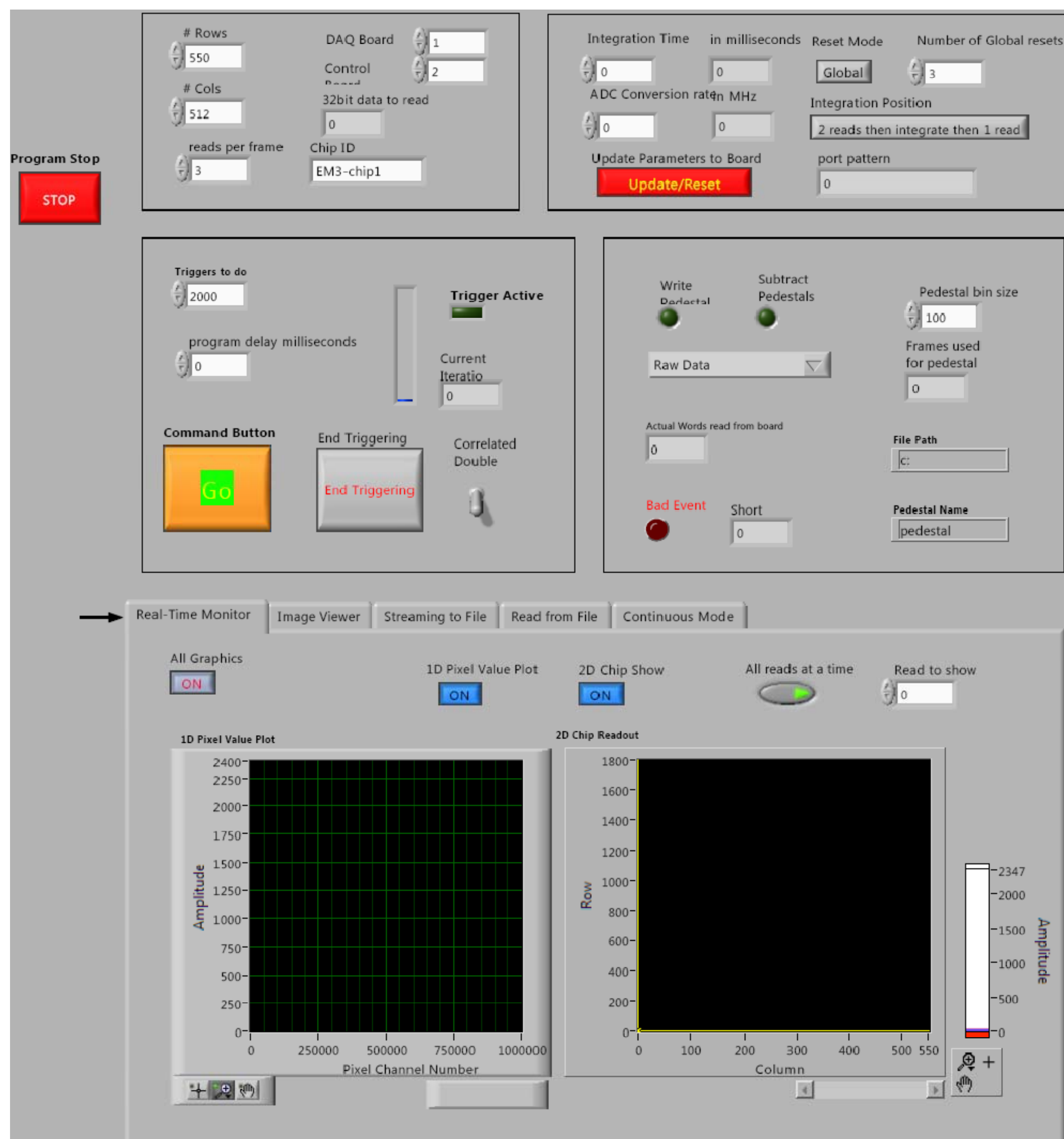

Figure 16. LABVIEW control interface for the EM3 system.

3.1.2 Mechanical Assembly and Cooling System

As electron microscopes require a vacuum environment for the entire beam path, the DDD system has to be mounted in vacuum in order to detect electrons directly. With a custom mechanical design, we were able to mount the DDD sensor and the supporting

electronics board onto a mechanical adapter that fits in a JEOL film drawer. As all JEOL microscopes share the same film drawer, the design allowed the DDD to be mounted onto all the JEOL microscopes available in the UCSD NCMIR resource. The film drawer was much easier to access compared with a bottom/side mount solution, and enabled quick installation and removal of the DDD prototypes on the microscopes and significantly sped up the development and testing.

Figure 17 shows the mechanical assembly used to mount the EM3 in a JEOL film drawer. The EM3 sensor was installed on the supporting electronics board, which in turn was mounted on a tray that can be inserted into the JEOL film drawer. All control and data signals were passed through the I/O connectors on the door.

Other than the I/O connectors, the door of the DDD mechanical assembly also had water cooling pipes passing through the vacuum interface. Right beneath the DDD sensor chip, a three-stage thermoelectric cooling module was coupled with a copper piece touching the backside of the sensor chip package. The hot side of the thermoelectric module was coupled with the water pipes so that the heat could be transferred out to a water chiller outside the vacuum.

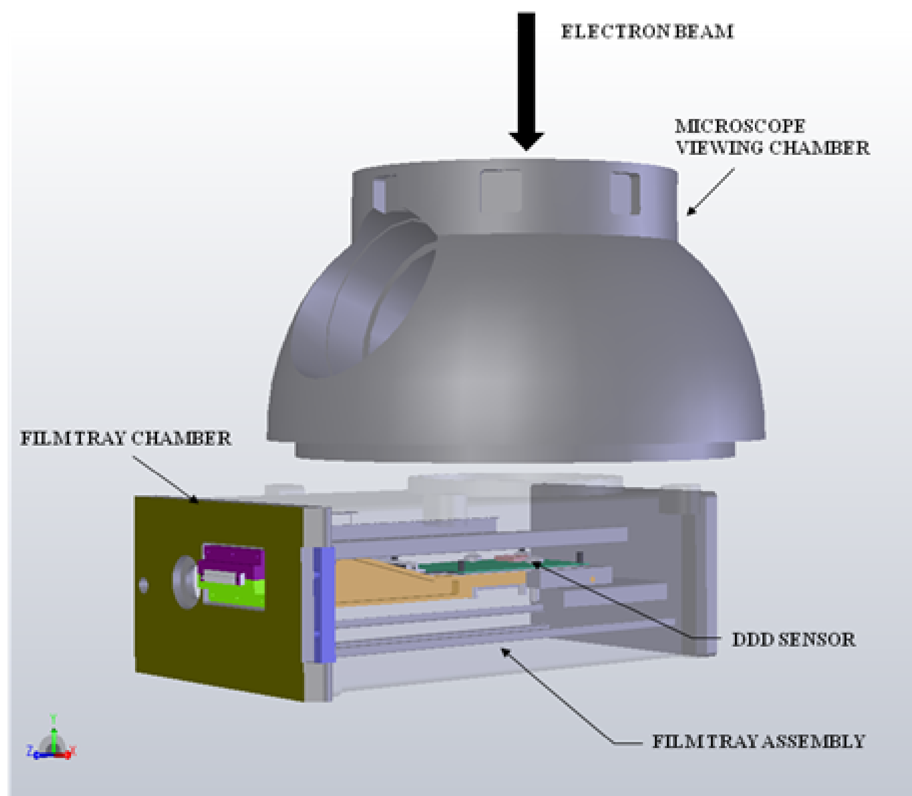

Figure 17. Mechanical mounting of the DDD sensor on a JEOL microscope.

3.1.3 Mechanical Shutter

As a safety measure to protect the DDD sensor from unwanted beam exposure, a mechanical shutter was placed directly above the sensor. It would remain closed unless the system was ready to acquire images with an electron beam.

Because the high energy electron beam can penetrate thin materials, the material and thickness of the shutter blade had to be determined. A convenient method to obtain the thickness needed to stop electrons with certain energies was to use the Continuous-Slowing-Down Approximation (CSDA) range from the NIST ESTAR database (Berger and Laboratory 1998). The CSDA ranges for 100-400keV electrons in selected materials

were shown in Figure 18. To reduce the Bremsstrahlung radiation that would be stronger in higher atomic number materials, it would be better to use low atomic number materials for the shutter (beryllium would be the best candidate). However, since beryllium was more costly and required proper handling, aluminum was eventually selected for the shutter. For 400keV electrons, the thickness of the shutter had to be thicker than 700 μm in order to stop the electrons. The thickness used in the EM3 shutter was about 2 mm, plenty for the protection purpose.

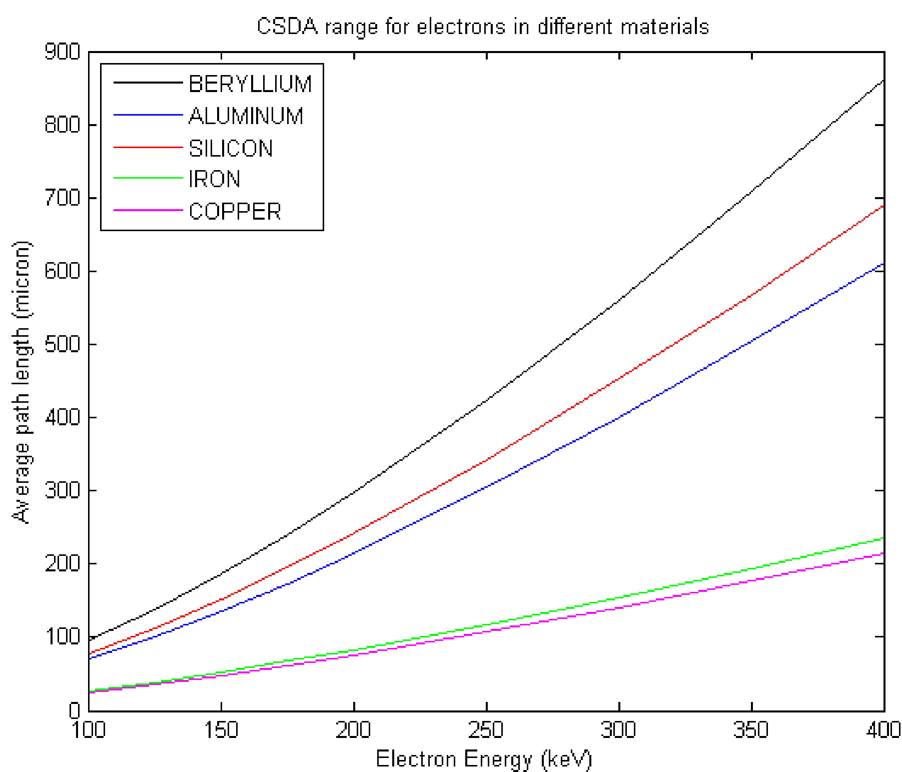

Figure 18. The CSDA ranges for 100-400keV electrons in selected materials.

3.1.4 Faraday Plate (Electron Beam Intensity Measurement)

The electron microscope normally has readings of the electron beam intensity, both from the viewing screen and the smaller focus screen. These readings are intended for determining the exposure time for taking images on film, but can also provide a baseline for an estimate of the electron flux.

To measure more accurately the electron flux, people have used a Faraday cup design. A “Faraday Cup” is essentially an electric current measurement device in the shape of a cup. The idea is to trap as many incident electrons as possible in the cup, and since every one of the electrons carry a unit of electrical charge, a beam current can be measured.

Borrowing from the idea of the cup design, we used a “Faraday plate” to measure the beam current. Using a plate instead of a cup design allowed us to minimize the height requirement while increasing the collection area. The collection plate was a square piece of aluminum a few millimeters thick. The thickness of the plate ensured that most incident electrons would be stopped in the plate and their electrical charges would be collected. An electrometer grade operational amplifier (op amp) circuit was then used to amplify the signal to a voltage that was later converted to digital values by an Analog to Digital Converter (ADC).

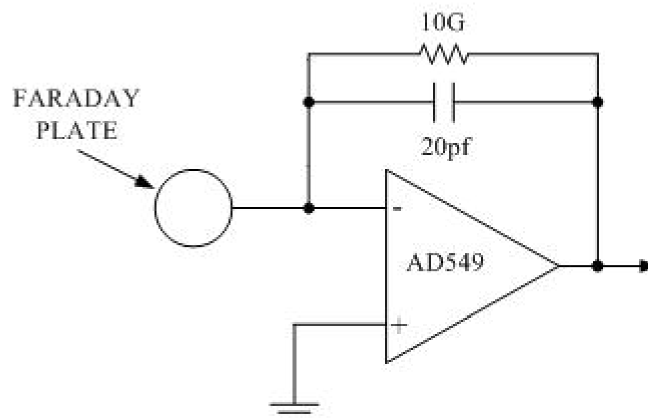

Figure 19. Schematic of the amplifier circuit for the Faraday plate.

Figure 19 shows the op amp circuit used for the DDD. The electrometer grade op amp was configured in a typical inverting mode. Because essentially no current was flowing into the op amp, the current input from the Faraday plate would equal to the current flow on the 10 Giga Ohm feedback resistor, thus providing a reasonably large output voltage. Using an aluminum plate of 1.27cm by 1.27cm (collection area = 1.61 cm^2), we can then convert the measured output voltage to the beam flux on the Faraday plate using the following equation:

Electron Flux = Measured Voltage / Feedback resistor value / Collection Area

In this equation, if we use the unit of millivolts for the measured voltage, giga ohm for the feedback resistor and square centimeter for the collection area, the calculated electron flux would be in the unit of picoampere per square centimeter (pA/cm^2), which was the common unit for electron dose in electron microscopy. For example, a measured voltage of 400 mV at the output can be converted back to a corresponding beam intensity of 24.8 pA/cm^2.

By changing the electron beam intensity to different brightnesses, a set of electron fluxes could be measured by using both the Faraday plate and the microscope viewing screen. The results at 200keV from the JEOL JEM-2000 FX microscope are presented in Figure 20. The measured beam intensity from the Faraday plate was plotted against the beam flux readings from the microscope viewing screen. They follow a linear relationship with a slope of close to 1. A slope of less than 1 here meant that the Faraday plate readings were actually higher than the readings from the viewing screen for any given electron flux. Because the viewing screen of each electron microscope was independently calibrated by the manufacturer, the electron flux readings from the viewing screen can vary from microscope to microscope. However, using exactly the same circuit and collection plate, our Faraday plate ensured consistent beam intensity results even when the DDD system was mounted on different microscopes.

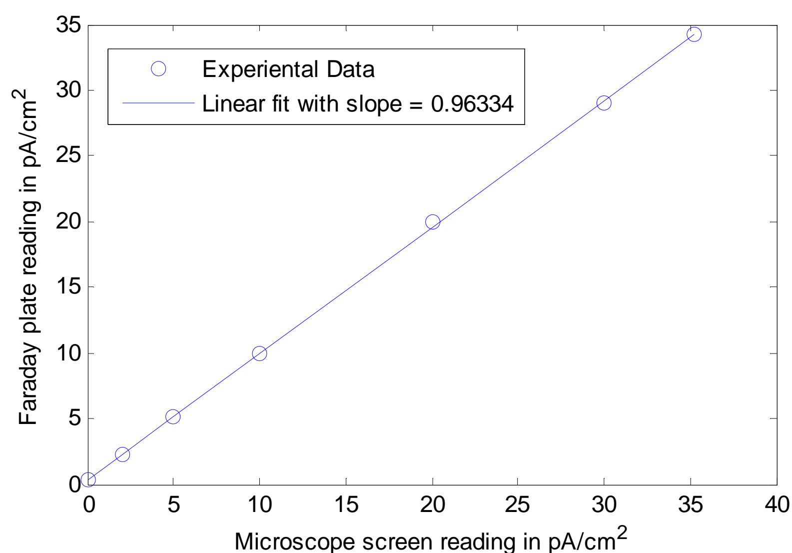

Figure 20. Measured electron beam flux from the Faraday plate and the microscope viewing screen at 400keV on the JEOL JEM-4000 EX.

There was a systematic error of using the plate design for the collection of the electron beam: a fraction of the incident electrons could exit the Faraday plate from the top surfaces or the sides (with a thick plate, there would be no transmitted electrons at the bottom surface). The number of electrons that would exit the sides would be relatively small as long as the collection area was big enough. However, the backscattering electrons would easily escape the top surface and would make the measured beam flux inaccurate. The traditional Faraday Cup design provides more accurate results, as the walls of the cup would effectively collect most of the backscattered electrons generated in the center of the cup.

To correct for this systematic error, one would need to know the fraction of primary electrons that hit the collection plate and later exited. Using the Monte Carlo simulation framework to be outlined in Chapter 5, this fraction was estimated to be around 14% for incident electrons with 120-400keV energy and an aluminum plate of 1.27 cm x 1.27 cm x 2 mm.

3.2 EM3 Sensor Characterization

A series of experiments were carried out to characterize the performance of the Direct Detection Device (DDD), including its noise characteristics, leakage current and energy conversion calibration.

3.2.1 Leakage Current (Dark Current)

Even when the sensor is not exposed to any external signal, the photodiode region of the DDD sensor pixels could still accumulate certain excess charges. The excess

charges come from the leakage current, which is a typical characteristic in CMOS image sensors. The contributions to the leakage current include: a) electron-hole pair generation near the photodiode in the depletion region; b) electron-hole pair generation near the interface between the top circuit and the epitaxial layer; c) diffusion current collected in the photodiode, but generated in the epitaxial layer. Because all of these leakage current sources are temperature dependent, the total leakage current is also directly related to the sensor temperature. At a certain temperature, the leakage current is a constant for any specific pixel, but it can have a large variation from pixel to pixel.

Figure 21 showed the histogram of all the pixel values in an image taken in total darkness. With CDS subtraction, most of the fixed pattern noise in the sensor was removed, except the leakage current contribution. The large spread of the pixel values in the histogram indicated large variations in the leakage current from pixel to pixel. As the distribution was not symmetric, the mean value of the CDS frame (69 ADC values) was actually quite different from the most probable peak value (32 ADC values).

The leakage current of any pixel at any given temperature can be experimentally measured by changing the integration time or exposure time while maintaining the sensor in total darkness (without any external signal). The longer the pixel is allowed to accumulate charges, the more dark charges will be collected in the photodiode. Therefore, a linear relationship would be observed between the measured pixel output and the effective integration time.

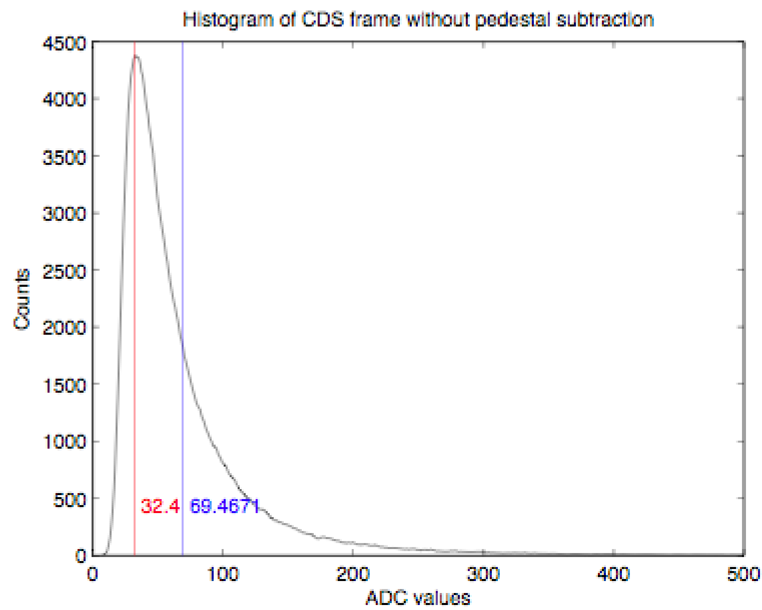

Figure 21. Histogram of all the pixel values in an image taken in total darkness. Only CDS subtraction was performed. Integration time was 58ms.

In Figure 21, the effective integration time was 58ms, and the temperature of the sensor was at 22.5 °C. After increasing the integration time to 309ms while maintaining all the other conditions the same, another image was taken and its histogram was shown in Figure 22. The most probable peak was now at 167.6 ADC values instead of 32.

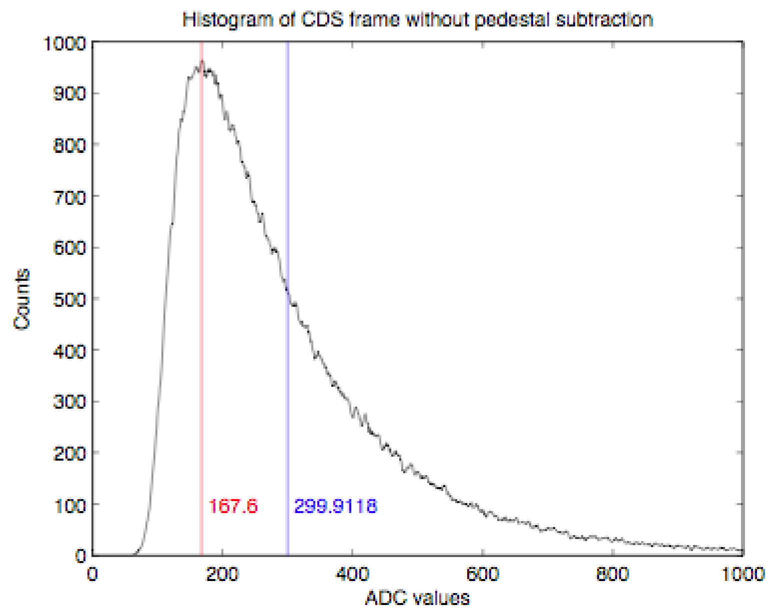

Figure 22. Histogram of all the pixel values in an image taken in total darkness. Only CDS subtraction was performed. Integration time was 309ms.

The same process was repeated for a few different integration periods and the most probable peak values were plotted against the integration time in the Figure 23. The resulting curve as expected was a linear curve with a slope of 0.542 ADC per millisecond. Considering that the 12 bit ADC full range was 2 Volts, 1 ADC = 0.488 mV. Therefore, the measured leakage current was 0.542 ADC/ms = 0.26 mV/ms.

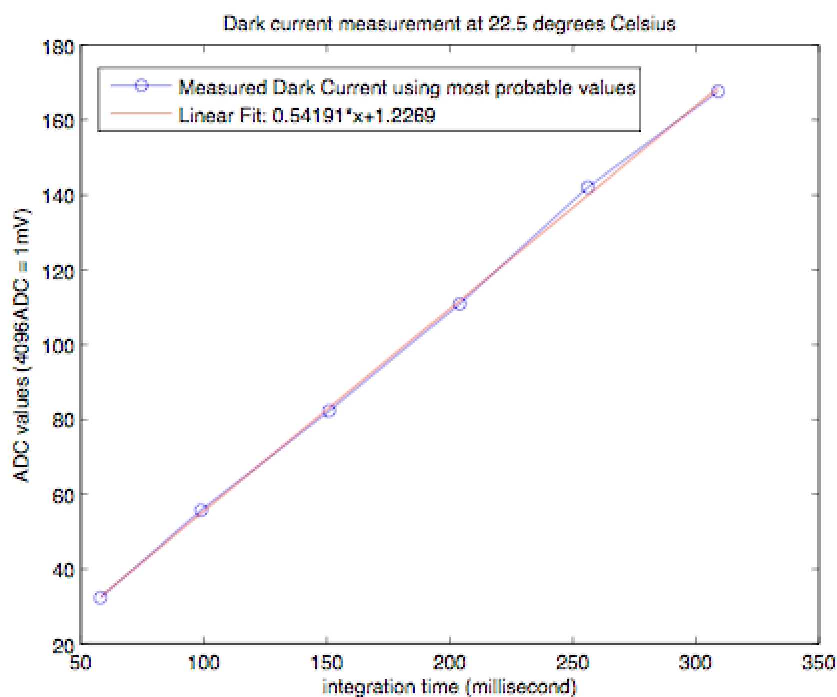

Figure 23. Leakage current measurement using the most probable peak values from the histogram of pixel values in dark exposure images with different integration periods.

To check the temperature dependence of the leakage current, the leakage current was measured using the same method at 10.9 °C, 1.2 °C and -22.5 °C (Figure 24). The leakage current was reduced to 0.049 mV/ms at 1.2 °C, one fifth of that at 22 °C. Cooling the sensor beyond 1.2 °C did not change too much of the leakage current, as other sources of noise dominated the pixel output and the measured values did not reflect the true leakage current anymore. Additionally, it was possible to convert the obtained leakage current value into units of electrons per millisecond (see section 3.2.4).

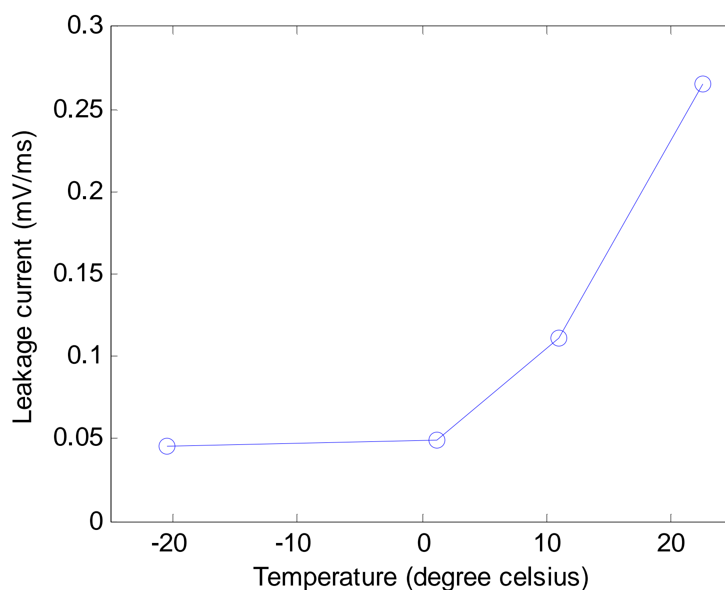

Figure 24. Temperature dependence of the measured leakage current.

The leakage current in the DDD was the major contributor to the fixed pattern of the image after the CDS subtraction, which eliminated the reset noise and other fixed pattern noise sources. The large variations of the leakage current had to be corrected; otherwise any real signals would be buried in the fixed pattern noise. We used a common method to deal with the fixed pattern noise, which will be referred to as pedestal correction method. The idea of the pedestal correction was to acquire a number of dark frames before taking any images from real signals. The average of these dark frames provided the pedestal baseline for each pixel corresponding to their leakage current values. This pedestal averaged image would be subtracted from any subsequent images from real signals, and thus effectively correcting the leakage current contribution. The pedestal should be re-taken if any of the conditions related to the leakage current were changed. For example, if the temperature or the integration time of the sensor or the

sensor chip itself were changed, a new pedestal would be needed. The leakage current could also change over time due to radiation damage, and thus it would be best to collect a new pedestal as frequently as possible.

3.2.2 Pixel Gain Variations

Due to imperfections in chip fabrication that affects the output in the pixel design, all DDD sensors have pixel to pixel gain variations. To minimize the effect of the gain variations, bright field correction can be applied. The electron beam was spread out to create a uniform illumination condition, and a set of images were acquired in the DDD. For each image, CDS subtraction and the pedestal correction were performed. The resulting images were then averaged to yield a bright field image.

All the pixels in the bright field image were divided by the mean value of the bright field to yield the gain correction ratios. Its histogram (Figure 25) showed that the distribution had a peak around 1.0 and a Full-Width-At-Half-Maximum (FWHM) of 0.087.

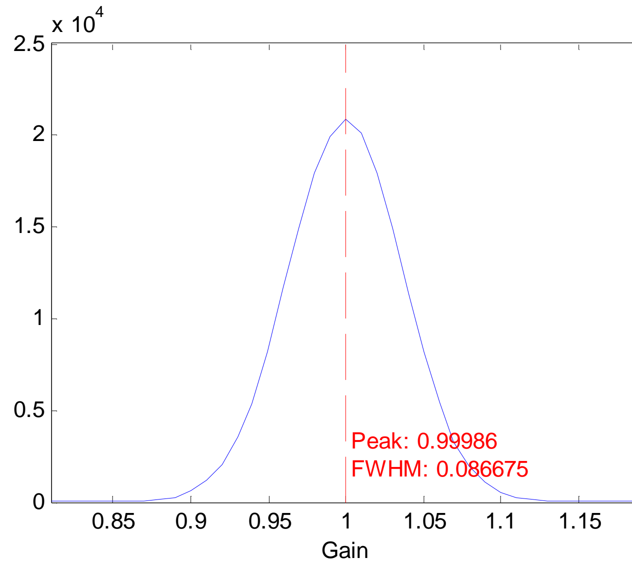

Figure 25. Gain variations shown in the bright field image.

The gain correction ratios could be then used to correct for the pixel gain variations for any images taken with the same sensor and acquisition settings. After CDS subtraction as well as pedestal correction, the images could be divided by the gain correction ratios obtained above, and yield the final corrected images. As most of the correction ratios fell within the 0.9 to 1.1 range, applying the gain correction would not affect the pixel values dramatically.

3.2.3 Noise in the DDD

The sources of the noise in the DDD system can be categorized into the following contributors:

1. Shot noise in the signal. In any signal event (incident photons or electrons), a certain number of ionization electrons are collected in the photodiode, but that

number of ionization electrons obeys the Poisson distribution. This is intrinsic noise and exists in any images taken with the sensor.

2. Reset noise or kTC noise is the noise associated with the pixel reset circuit. Each time when the reset switch is activated in the pixel and the reset voltage is applied to the photodiode, the pixel voltage will not return to exactly the same voltage level as that after the previous reset. The reset noise is temperature dependent and also related to the capacitance of the photodiode; therefore, it is also called the “kTC” noise. As noted before, the reset noise is effectively eliminated using the CDS readout.
3. Offset fixed pattern noise (FPN) is the different voltage levels that the pixels can exhibit. As it is an offset, the FPN is effectively removed after the CDS subtraction.
4. Thermal noise or leakage current shot noise is the random variations in the dark charges that can accumulate in the photodiode. Its statistical distribution follows a Poisson probability with the mean value being the leakage current measured in the section 3.2.1. As the variance of the Poisson distribution equals the mean, the shot noise has the same dependence on temperature and the integration time as the leakage current.
5. Readout noise refers to the added noise from the readout electronics. The readout electronics can include the on-chip pixel level buffer (source follower) circuit as well as the off-chip amplifier and ADC circuit. The source of the analog readout noise can be related to board layout and the interferences between the analog voltage traces and the clock sources. The ADC could

introduce input-referred noise or code transition noise, which should be small when using a high resolution ADC device. The link connecting ADC digital output to the input on the acquisition PC card might also be subject to digital noise, which can be neglected if the transfer rate and the cable length are properly chosen.

6. Random Telegraph Signal (RTS) noise is a switching noise, whose origins might be related to dislocations, metal precipitates and surface conduction channels in the p-n junctions. For the DDD sensor, the RTS noise in the source follower transistor can have a big contribution to the noise. The measured RTS noise behaviors are outlined in the following subsection.
7. The pixels along the edge of the sensor array can exhibit much higher sensitivity than pixels in the middle of the array. We normally ignored the readings from the outermost two to five pixels along the perimeter of the chip.

3.2.3.1 Random Telegraph Signal (RTS) Noise

When looking at the noise floor of the DDD sensor kept in total darkness, some pixels exhibited flickering noise, on top of the random white noise. The outputs from a normal pixel and a pixel with RTS signal are shown in Figure 26.

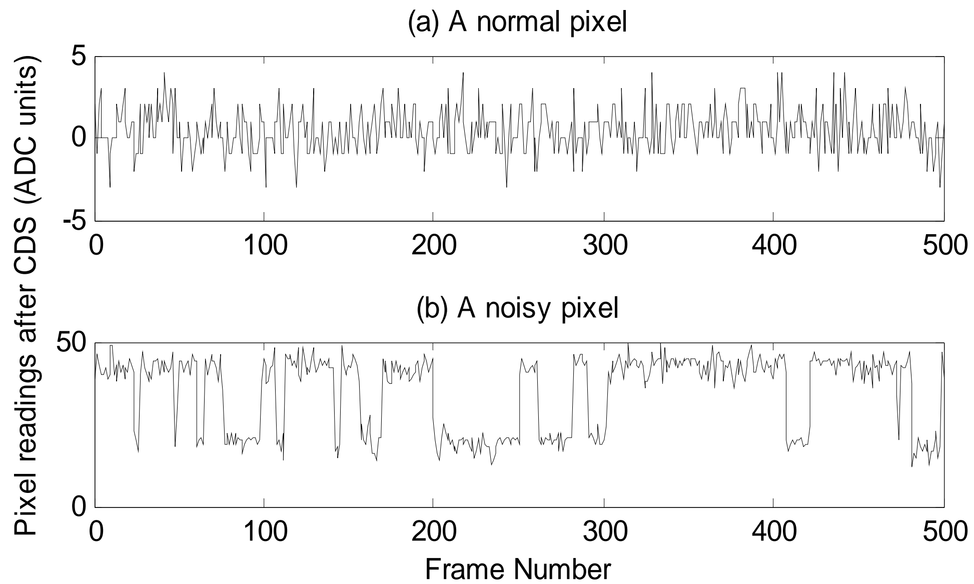

Figure 26. The readings of (a) a normal pixel and (b) a noisy pixel showing RTS noise, in 500 continuous frames.

The RTS noise was commonly observed in CMOS imaging sensors (Janesick, Andrews et al. 2006; Leyris, Martinez et al. 2006; Wang, Rao et al. 2006). The RTS signal was believed to be generated in the source follower transistor in the pixel structure.

By looking at specific pixel readings over a period of time, a noisy pixel with RTS feature can be distinguished because they manifested two distinct levels and randomly jumped from one level to the other. To detect and map the pixels with excessive RTS noise, more than 5000 background frames were collected (with no external signals) and then the standard deviation σ of the readings of all pixels after correlated double sampling was determined. These readings were also dark current corrected, using the average of a preliminary acquisition of 500 frames to establish the pedestal frame. Noisy pixels were defined as the ones that gave an average reading

greater than 10σ in at least 0.5% of the total number of frames. The noisy pixel map, containing the noisy pixel positions, was stored in a file and their readings were replaced by the average of the neighboring pixel readings in final images.

The total number of noisy pixels was less than 1.5% of the whole array. By comparing the noisy pixel map with the map of the same chip after one month of usage in the electron microscope, we found that at least 80% of the noisy pixels in the new map matched the previous map.

3.2.3.2 Measured Total Noise after Correction

After the CDS subtraction and the pedestal correction, the images taken with the DDD in total darkness still contain thermal noise, readout noise as well as RTS noise. To measure the total noise of the sensor, we collected one dark frame at 22.5 °C with 58ms integration time. CDS subtraction and the pedestal correction were then applied. The histogram of all the pixel values in the resulting image is shown in Figure 27. As expected, the mean of the image is now at zero, which indicats the successful removal of the fixed pattern noise, reset noise and leakage current baseline in all the pixels. The Full-Width-at-Half-Maximum (FWHM) of the noise distribution is about 8.4 ADC, so it is equivalent to a Gaussian noise with a standard deviation of 3.6 ADC units. The same method was used to measure the total noise at lower temperatures: at -10 °C, the standard deviation dropped to 2 ADC units or 0.976mV. Additionally, the total noise can be expressed in unit of electrons (see section 3.2.4).

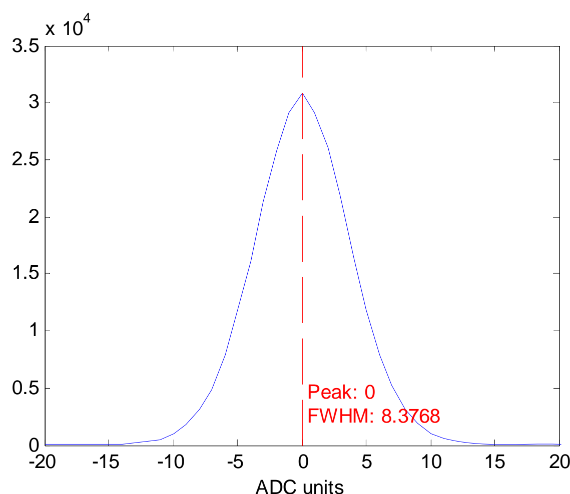

Figure 27. The histogram of a dark frame after CDS subtraction and pedestal correction.

3.2.4 Device Calibration Using X-ray Photons

The physics of signal charge generation in the DDD described in 2.1.2 only applies to electrons but it can be expanded to include photons as well. The dominant interactions of photons with the sensing volume in the DDD are photoelectric absorption, Rayleigh (coherent) scattering, and Compton (incoherent) scattering. The cross sections for different processes of the photon-silicon interactions are plotted in Figure 28 in the energy range of 1keV to 500keV.

For ^{55}Fe radiation source emitting 5.9keV X-ray photons, Figure 28 indicates the photoelectric absorption would be the dominant effect in the sensing volume of the DDD.

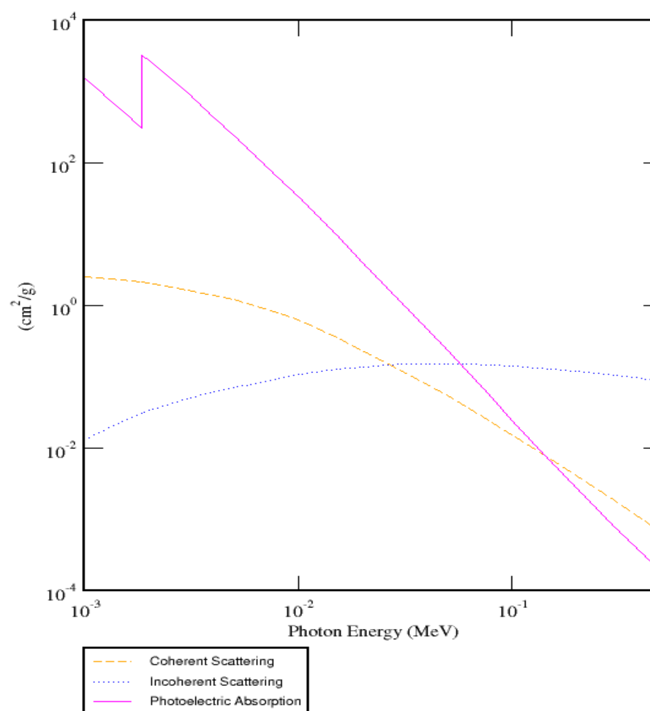

Figure 28. Cross sections of coherent, incoherent scattering and photoelectric absorption for silicon and photons with energies in the range of 1keV to 500keV.

The absorbed photon energy will be converted to ionization electrons and can be collected in the photodiode. The photon can be absorbed at any depth in the DDD sensor, and by chance, it might be absorbed near the depletion region of the photodiode where all of the generated ionization electron will get collected in that specific photodiode. Since every ^{55}Fe photon carries 5.9keV of energy and the ionization energy in silicon is 3.6eV, we can expect on average 1639 ionization electrons to be collected in such a scenario.

In the calibration experiment using the ^{55}Fe photons, the radiation source was placed on top of the sensor chip (less than 1cm away from the chip surface). The experiments were carried out in low temperature (-10 °C) to minimize noise. More than

10000 frames were then collected and processed using CDS subtraction as well as pedestal correction. Because the standard deviation of the pixel noise is about 2 ADC units, any pixel reading higher than 20 ADC units was considered a photon signal.

Figure 29 shows the histogram of the values in the 81107 events found. The main peak was around the event cut-off of 20 ADC, and it corresponded to the events where the signals from the incident photons were small and comparable to the noise floor. The additional peak around 84 ADC was the peak used for calibration, as it represented the case when the incident X-ray photon was absorbed right near the depletion region of the photodiode, resulting in the total conversion of its energy. A Poisson curve was fitted to that peak and the mean was obtained at 84 ADC units, which was the equivalent signal for 5.9keV of converted photon energy or 1639 ionization electrons. As each ADC unit was equal to 0.488mV, the calibration could be expressed as 0.051 ADC unit/electron or 0.025mV/electron.

Using the signal charge conversion of 1639 ionization electron to 84 ADC units, we can in turn estimate the noise of the sensor to be 40 electrons at -10 °C (see section 3.2.3.2 for the original ADC values). The leakage current can be then estimated at 10 electrons/ms at 22.5 °C and 2 electrons/ms at 1.2 °C (see section 3.2.1 for the original ADC values).

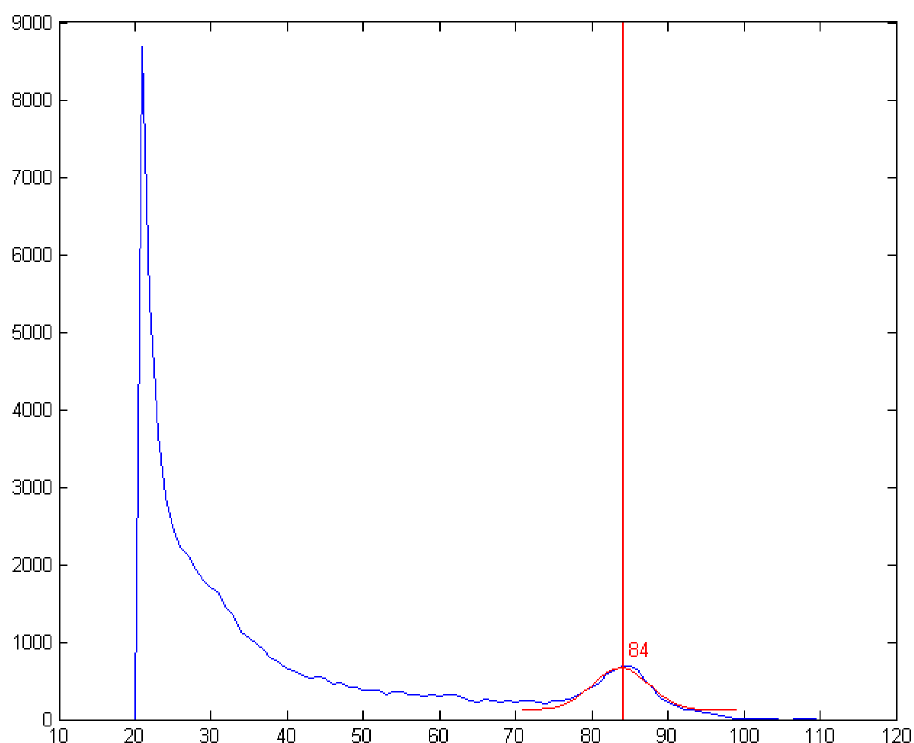

Figure 29. The peak value histogram for events detected in EM3. The peak around 84 ADC was fitted with a Gaussian and the mean value corresponded to the 5.9keV ^{55}Fe photon calibration.

The same data acquisition was repeated for a ^{109}Cd radiation source as a validation. The peak corresponding to 22.1keV characteristic X-ray was found at 310 ADC units, which also translated to the same value of 0.025mV per ionization electron as obtained from the ^{55}Fe calibration.

For all the detected events, a 7x7 matrix can be obtained around the peak value and the average of all these matrices yielded the average matrix as shown in Table 2 (for ^{55}Fe) and Table 3 (for ^{109}Cd). Most of the ^{55}Fe signals were contained in the 3x3 matrix around the center peak, while the ^{109}Cd signals had more spread and needed a 5x5 matrix.

The peak value in the ^{55}Fe matrix contributed to more than half the total signal, while the peak in the ^{109}Cd signals contributed to less than half of the total due to the larger signal spread.

Table 2. The 7x7 average matrix from the ^{55}Fe events.

0	0	0	0	0	0	0
0	0	0	0	0	0	0
0	0	2	6	2	0	0
0	0	6	43	6	0	0
0	0	2	6	2	0	0
0	0	0	0	0	0	0
0	0	0	0	0	0	0

Table 3. The 7x7 average matrix from the ^{109}Cd events.

0	0	0	0	0	0	0
0	0	1	1	1	0	0
0	1	4	11	5	1	0
0	1	11	65	12	1	0
0	1	5	12	5	1	0
0	0	1	1	1	0	0
0	0	0	0	0	0	0

The signal spread seen in the average matrix came from the ionization electron diffusion in the events where the incident X-ray photons were absorbed in the epitaxial layer not close to the photodiode. Therefore, it contained information about how the ionization electrons diffused in the epitaxial layer. This information will be explored more in the section 1.1.

3.3 Detector Responses from Beam Electrons

As described in the previous section, the X-ray photon interactions with the DDD sensor differ from the electron interactions in terms of the signal charge generation mechanism. The experimental results from beam electrons of energy from 120-400keV are presented.

3.3.1 Uniform Electron Illumination

By mounting the EM3 on the JEM-2000 FX II and JEM-4000 EX microscopes, we were able to systematically measure the detector responses to high energy electrons in the transmission electron microscopes.

The DDD detector was first submitted to uniform electron illumination. The electron beam was spread out to an area much larger than the detector area. The beam intensity was measured independently by the Faraday plate (described in 3.1.4). To express the incident electron flux in a more convenient unit for further analysis, we used the unit of electrons per pixel per frame. With a pixel size of 5μm and a frame integration time of 58ms, one electron per pixel per frame is equal to one unit of electronic charge in

an area of 25 square microns in 58ms of time. Substituting in all the constants, we get 1 electron/pixel/frame = 11 pA/cm^2.

Multiple images were taken at different beam intensities. After CDS subtraction and pedestal correction for each image, the mean values of the center regions (100x100 pixels crop) were plotted against the beam intensities in Figure 30. Average ADC values in the DDD detector for different uniform electron dose at 200keV. for 200keV beam, and in Figure 31 for 400keV beam. The mean values increased linearly in both plots. A slope of 122ADC per incident electron (equivalent to 8.57keV of deposited energy) was found for 200keV, and for 400keV, the slope was 88.7ADC per incident electron (or 6.23keV). The slope was an accurate measurement of the average signal generated by each incident electron in the entire sensor array.

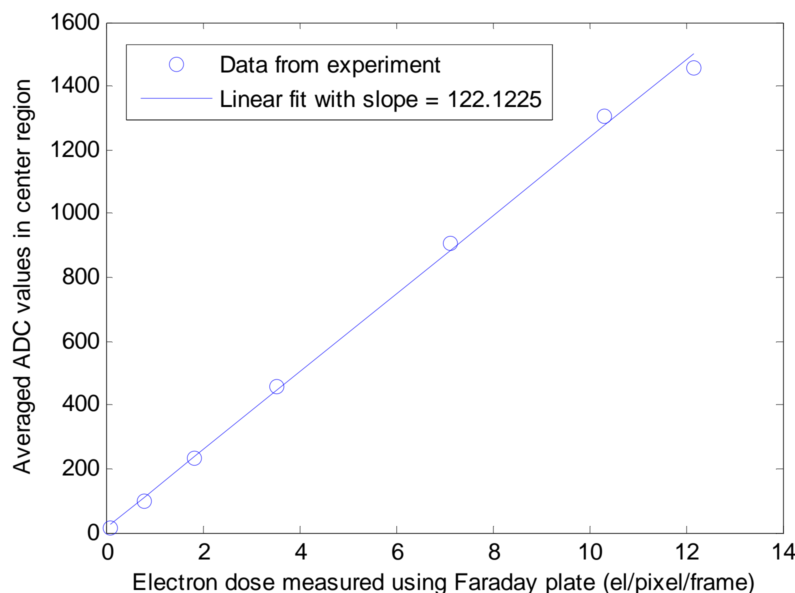

Figure 30. Average ADC values in the DDD detector for different uniform electron dose at 200keV.

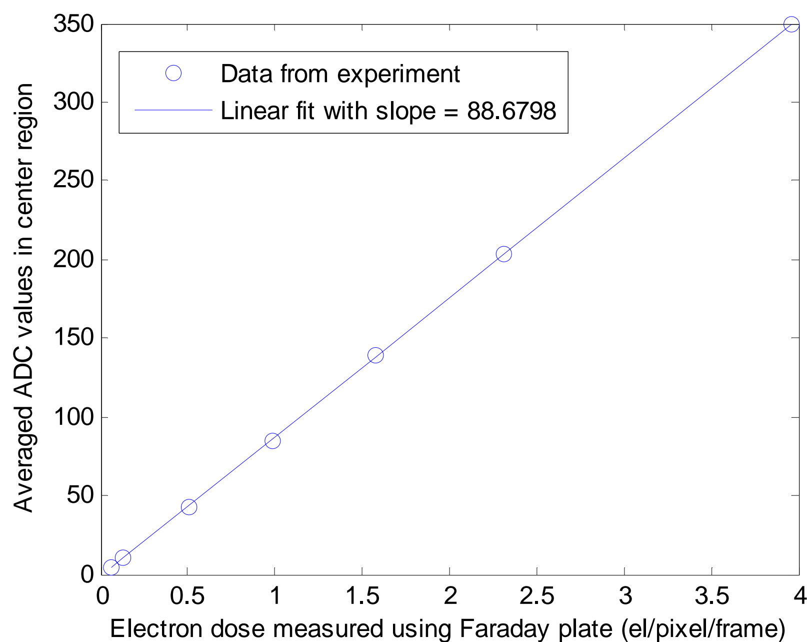

Figure 31. Average ADC values in the DDD detector for different uniform electron dose at 400keV.

The same method was used to obtain the signal response from other beam energies. The results were combined in Figure 32. Average ADC values in the DDD detector for different uniform electron dose at 120keV, 200keV, 300keV and 400keV beam energy. With lower beam energy, the slope was higher due to the fact that lower energy electrons would have more interaction and lose more energy in the same epitaxial layer than higher energy electrons.

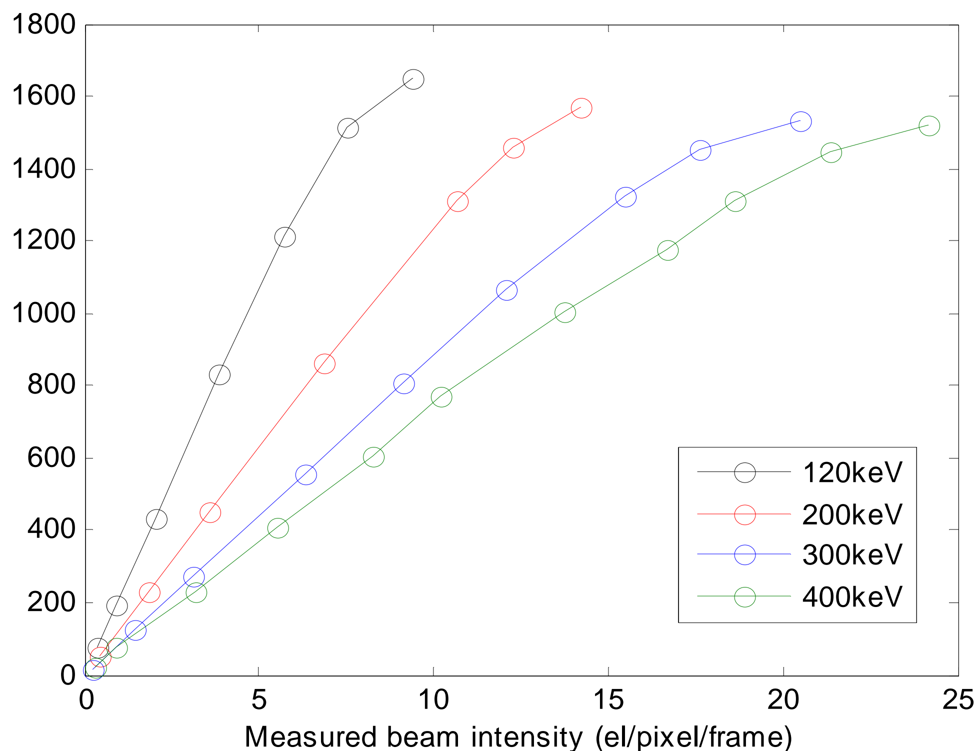

Figure 32. Average ADC values in the DDD detector for different uniform electron dose at 120keV, 200keV, 300keV and 400keV beam energy.

At higher beam intensities, the EM3 sensor started to show saturation, because the pixel output voltage dropped near the ground level and cannot drop further. At saturation, the sensor pixel output would remain unchanged even if more incident electrons were hitting. For 120keV beam electrons, the sensor reached saturation after about 8-9 electrons/pixel/frame, and for 400keV electrons, the saturation level was around 20 electrons/pixel/frame. This limited dynamic range of the DDD sensor was the trade-off of the high sensitivity of the device. One way to compensate the limited dynamic range is to acquire multiple images and sum them together. Because most of the noise in each image was uncorrelated, the summation would increase the total noise in the final image.

3.3.2 Single Electron Hits

In section 3.3.1, the total deposited energies in the EM3 by beam electrons were measured. However, they did not include any information about how the energies were distributed in the pixel array, which is very important for understanding the spatial resolution of the sensor.

To measure the response of EM3 to any single incident electron, the electron beam intensity was reduced so that only a few incident electrons were hitting the entire sensor array in the integration time. More than 10000 frames were collected and using the same method as in the X-ray photon experiment, the single electron events were identified. Because the experiment was carried out at room temperature, a higher threshold of 40 ADC units, 11 times the noise standard deviation of 3.6 ADC units, was used to distinguish the electron hits from the background noise. Figure 33(a) shows a typical reading for a detected single incident electron of 300keV. In these single electron events, the significant pixel values were always grouped inside a 5x5 array centered on the pixel with the maximum reading. By averaging the 7x7 arrays selected around the center pixel for each detected electron event, we were able to calculate the average pixel readings distribution. Figure 33(b) shows such a distribution for 300 keV incident electrons. The average distribution had significant values inside a 5x5 array centered on the peak pixel. By summing over this 5x5 array, we determined an average signal value of 214 ADC units for a single electron event. Assuming the noise in each pixel of the 5x5 array was uncorrelated and could be summed in quadrature, the total noise for the sum of 25 pixels in the 5x5 array should be 18 ADC units. So the average signal to noise ratio

(SNR) for a detected 300keV electron was 12/1. Very similar SNR values were also obtained for 200 and 400 keV electrons.

However, if we compare the average signal of 214 ADC found in the single 300keV electron events with the slope for 300keV in Figure 32, the average signal in the detected single electron hits data was much higher. The discrepancy came from the high threshold that we used in the detection of electron events. If an event had a peak value smaller than the threshold of 40 ADC units, our detection algorithm would simply ignore them. As the undetected events were usually smaller signals, the average matrix from the detected signals was biased towards a higher signal. On the other hand, the uniform illumination experiment did not use any threshold and the total signal obtained was a true representation of the average energy deposited in the sensor.

a. Pixel readings for a typical event

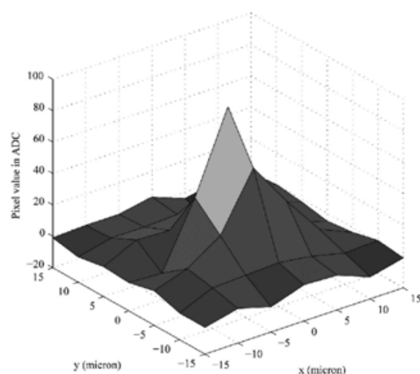

	Y_1	Y_2	Y_3	Y_4	Y_5	Y_6	Y_7
X_1	-3	2	-4	3	2	-6	-1
X_2	-3	6	7	8	5	0	1
X_3	2	9	23	59	31	6	-3
X_4	-2	-3	38	89	29	1	-5
X_5	-1	9	8	25	6	5	-2
X_6	-4	1	1	2	-10	5	0
X_7	-1	0	0	4	-4	0	-2

b. Average distribution

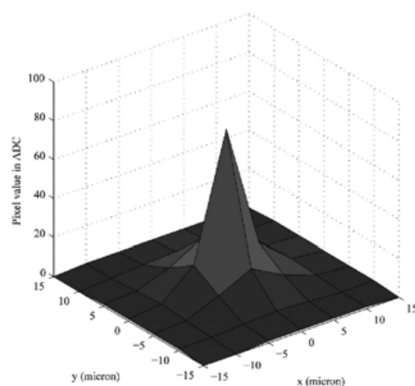

	Y_1	Y_2	Y_3	Y_4	Y_5	Y_6	Y_7
X_1	0	0	1	1	1	1	0
X_2	1	1	2	3	2	1	1
X_3	1	2	9	17	8	2	1
X_4	1	3	17	81	17	3	1
X_5	1	2	8	17	8	2	1
X_6	0	1	2	3	2	1	1
X_7	0	1	1	1	1	1	0

Figure 33. (a) the typical pixel readings of a single 300keV electron event and (b) the average distribution of all the detected events.

To get consistent results, it is necessary to lower the detection threshold. Unfortunately for the EM3, the total noise limited how low the threshold could be (lowering the temperature helped, but it was not enough). See Chapter 4 for more results from the EM5 which had lower noise.

The SNR of the single electron events would have dropped to a smaller value if all the undetected events were counted in. However, as the signals from the undetected

events were smaller, it would be likely that the signal spatial distribution would be less than the higher signal events, i.e. within the 5x5 region. We could then predict that for 400keV electrons, the signal of 88 ADC units obtained from the uniform illumination experiment would be absorbed in a 5x5 pixels region, still yielding a SNR of 5/1. For lower energy electrons, the SNR would be even higher as the signals were larger than the 400keV electrons.

The single electron hits confirmed that the EM3 was single electron sensitive with an average SNR of at least 5/1 for 400keV electrons at room temperature (higher SNR with lower energy electrons or lower operation temperatures) and most of the signals were deposited in a 5x5 pixels region.

3.3.3 MTF Measurements Using Edge Method

3.3.3.1 Modulation Transfer Function (MTF)

The Modulation Transfer Function (MTF) is a widely accepted way of describing the performance of an imaging system. We used the edge method (De Ruijter and Weiss 1992; Weickenmeier, Nüchter et al. 1995) to determine the real-world MTF performance of the DDD sensor.

The edge method measures the response of an imaging system to an input of sharp edge transition. The edge input was created on the EM3 by using a sharp metal edge, placed directly on the sensor chip. 500 frames were acquired from the DDD sensor, and after CDS subtraction and pedestal correction, the frames were summed together to create one edge image. The sensor and the edge were illuminated by a uniform electron beam.

Several of such images were taken for different incident electron energies and then passed on for MTF analysis, adapted from Meyer and Kirkland (Meyer and Kirkland 2000). The MTF analysis at 300keV beam energy is presented as an example.

The orientation of the edge was roughly lined up with the columns in the pixel array, as seen in Figure 34. The bright area on the left was the area exposed to electron beam, and the dark area was covered by the metal edge.

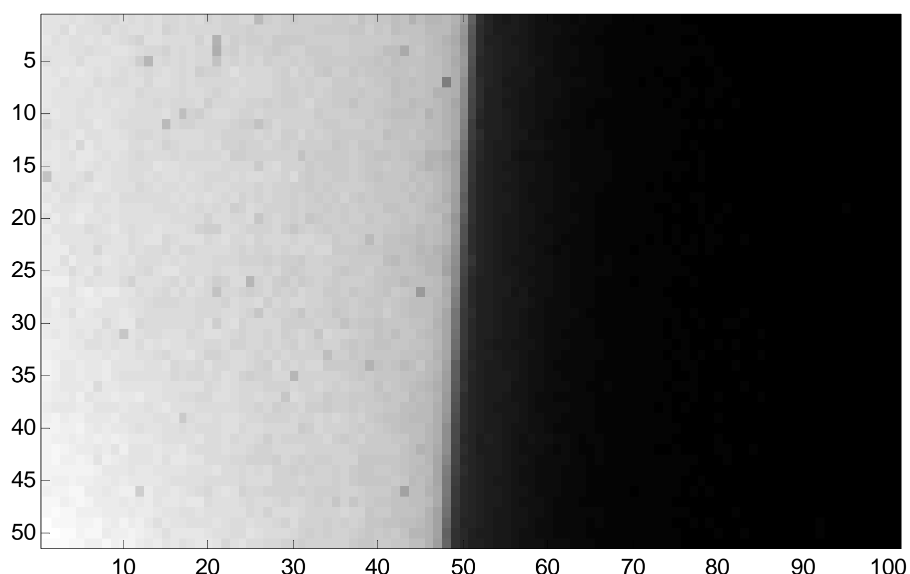

Figure 34. The image from EM3, showing the edge transition. Image was a 52x100 pixels crop from the original image.

For each row in Figure 34, a single line profile was obtained. It was then over-sampled by 8 times using linear interpolation, and the transition from the bright area to the dark area was determined for each row to sub-pixel resolution. Based on the edge position found for each row, multiple line profiles (original line profiles, not oversampled) were aligned and averaged together to yield the final edge profile. The edge

profile obtained this way uses only the raw data but was still 8 times over-sampled. To further reduce noise contributions, the edge profile could be fitted with an analytical function as proposed by Weickenmeier (Weickenmeier, Nüchter et al. 1995). Figure 35 shows the oversampled edge profile from the raw data along with the fitted curve.

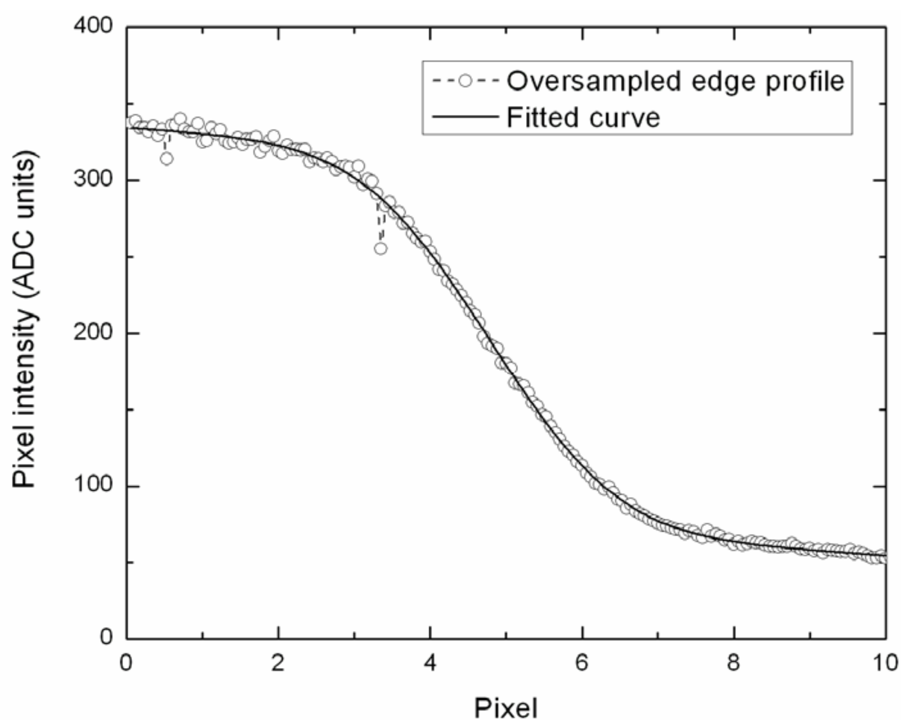

Figure 35. Oversampled edge profile from raw data as well as the fitted edge profile using an analytical function.

The derivatives of the edge profile obtained above would produce the line spread function (LSF). And the Modulation Transfer Function (MTF) was the Fourier transform of the LSF. To correct for the finite pixel size effect (Meyer and Kirkland 2000), the MTF curve was divided by the sampling function (sinc function) based on the 5μm pixel

size, and the resulting MTFS curve is shown in Figure 36. Here MTFS stands for sinc function corrected MTF.

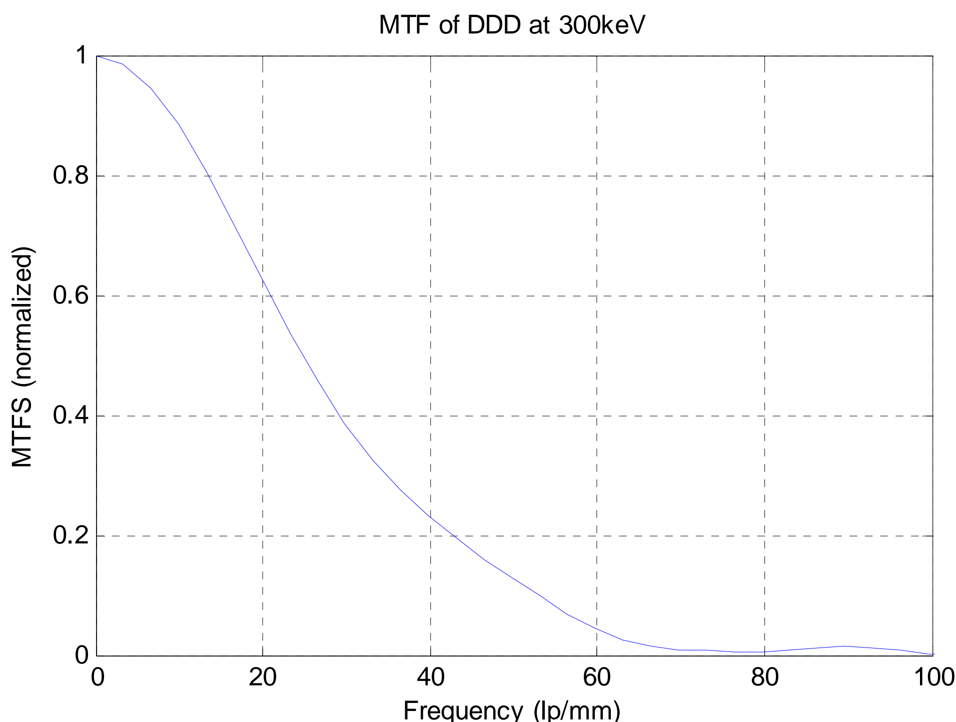

Figure 36. MTFS curve of the EM3 at 300keV using the edge method.

As in Table 4, comparing the MTF of EM3 to the publicly available MTF data from scientific CCD camera manufacturers like Gatan, it is clear to notice the imaging advantages of the DDD sensors. The Nyquist frequency is calculated from the pixel size. Because in perfect imaging sensors, the highest frequency it can detect without aliasing is a spacing separated by a single pixel. Its corresponding spatial frequency is then 1/(2*pixel size). For the EM3, the Nyquist frequency is 1/(2*5μm) = 100 line pairs per millimeter (lp/mm). The MTF at half Nyquist frequency was usually quoted in CCD data sheets, and for the EM3, it was at about 15%. With a larger effective pixel size for the

CCD cameras due to the use of scintillation screen, the Nyquist frequencies for CCD cameras are typically in the range of 30 to 50 lp/mm. The Gatan UltraScan 4000 was quoted with a MTF of >20% at 16.7 lp/mm, while the EM3 at 16.7 lp/mm has a MTF value of >60%. The EM3 clearly outperformed the CCD cameras in terms of spatial resolution.

Table 4. Comparing the EM3 MTF values to the public datasheet from commercially available scientific CCD manufacturers

Sensor	Pixel size	1/2 Nyquist frequency (lp/mm)	MTF at 1/2 Nyquist	Method
EM3	5 μm	50	15%	Edge (300keV)
Gatan UltraScan 4000	15 μm	16.7	>20%	Edge (120keV)
Gatan UltraScan 1000	14 μm	17.9	>15%	Edge (120keV)

It is also possible to use a Gaussian shape curve to fit the LSF, but the resulting MTF curve would not be accurate at low frequencies as it removed the low frequency tails in the LSF. However, for qualitative comparisons of MTF curves at different beam energies, the Gaussian fitting would help reduce the noise oscillations in the MTF curves. In Figure 37, the MTF curves at different beam energies from 80keV to 400keV were plotted together. The MTF became significantly worse when the beam energy was lowered to 120keV. It can be explained by the fact that the energy deposited by a 120keV electron is larger than a 400keV electron and its signal charge distribution in the pixel

array is larger. Therefore the edge profile detected in the EM3 for 120keV electrons would be more blurry than that for 400keV electrons.

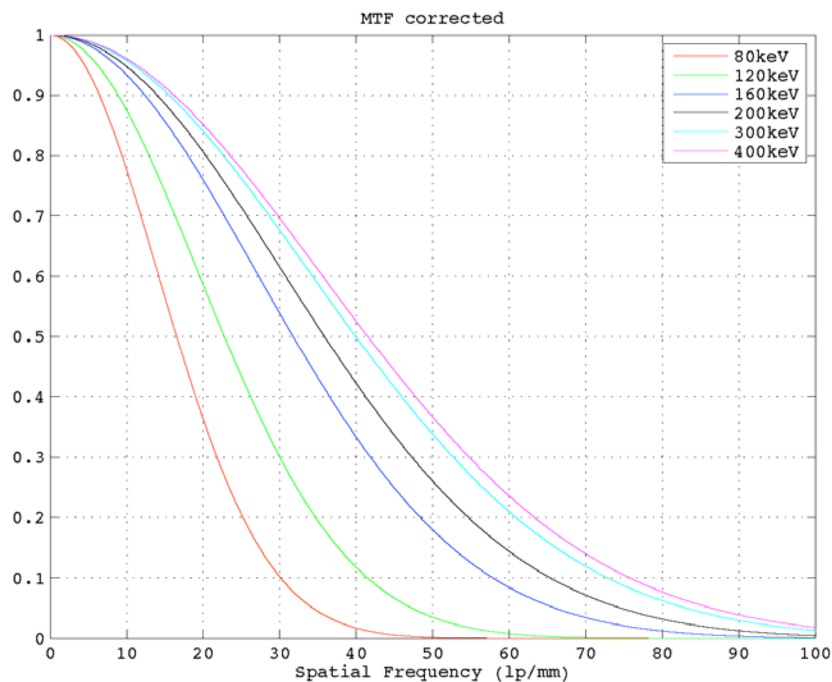

Figure 37. MTF curves from the edge method at different incident beam electron energies. The LSF curves were fitted with a Gaussian shape, so the MTF curves in this plot were for qualitative comparison purposes only.

3.4 Radiation Damage

The advantage of the EM3 in the spatial resolution did not come without a trade off. Because the EM3 uses direct detection of high energy electrons, the sensor is exposed to the beam electrons directly and will be subject to radiation damage, while in the case of CCD cameras, the beam electrons are stopped by a lead window so the CCD sensors are protected.

The interaction between the high energy incident electrons and the silicon in the DDD sensor will introduce trapped holes or new interface states. The most obvious behavior of the degraded device after radiation is a dramatically increased leakage current.

We designed an experiment to quantitatively measure the radiation effects in the EM3 sensor. The sensor chip was illuminated with 300keV electron beam at a constant intensity for a sustained period of time. At certain time intervals, the leakage current of the sensor was measured and to make sure the sensor still responded to single electrons, the beam intensity was lowered and single electron data were obtained. The beam intensity was raised to the same level again after the single electron data were acquired and the radiation test was continued. The beam intensity was recorded by the Faraday plate and integrated over time to yield the accumulated dose. The entire procedure was repeated on two EM3 sensors, one at room temperature, and the other one at -15°C. The leakage current of the sensor increased linearly with the accumulated electron dose that was put on the sensor.

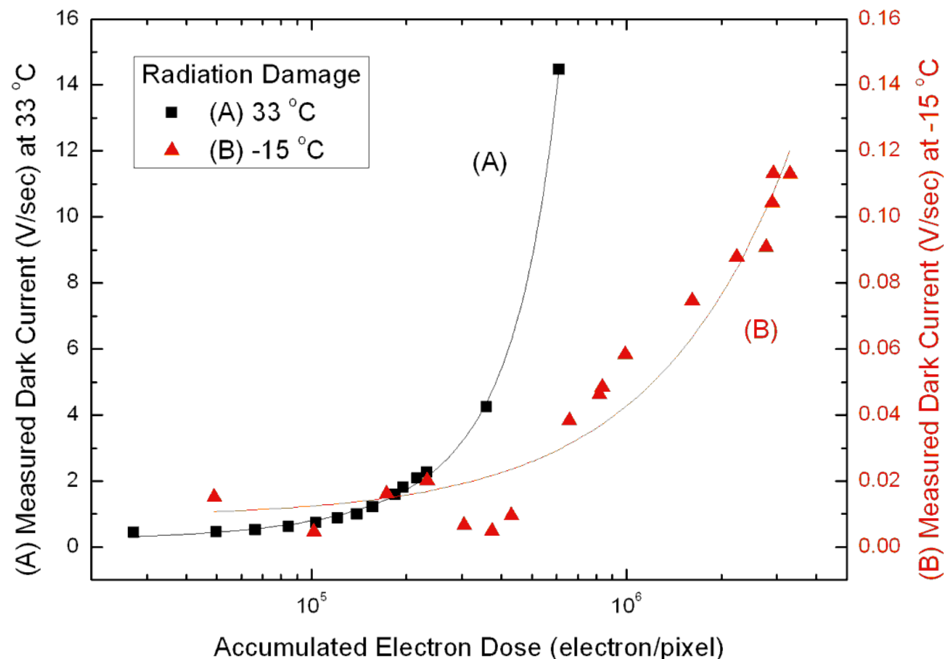

Figure 38. The increase of the leakage current at different levels of radiation. The room temperature and the low temperature results were plotted together but with different y-scales. (a) black squared at 33°C; (b) red triangles at -15°C. The lines were the linear fit to the data.

With low accumulated dose, the increase in the leakage current can be corrected by using the pedestal correction procedure. However, the leakage current will eventually reach a level that is so high that the dynamic range of the sensor becomes zero, i.e. after every integration period, even without any external signal, the sensor will appear saturated just by the leakage current. At that point, the sensor becomes unusable.

At room temperature, we observed that the DDD became unusable after a fluence of $3.6x10^5$ electrons/pixel. As the leakage current is temperature dependent, with the

sensor cooled down to -15°C, the EM3 sensor worked even after a fluence of $3.6x10^6$ electrons/pixel, i.e. an order of magnitude more exposure than at room temperature. The radiation tolerance of the EM3 is at least in similar range as other silicon detectors if not better (Faruqi, Henderson et al. 2005).

a. before radiation damage

	Y_1	Y_2	Y_3	Y_4	Y_5	Y_6	Y_7
X_1	0	0	1	1	1	1	0
X_2	1	1	2	3	2	1	1
X_3	1	2	9	17	8	2	1
X_4	1	3	17	81	17	3	1
X_5	1	2	8	17	8	2	1
X_6	0	1	2	3	2	1	1
X_7	0	1	1	1	1	1	0

b. after radiation damage

	Y_1	Y_2	Y_3	Y_4	Y_5	Y_6	Y_7
X_1	0	1	1	1	1	1	1
X_2	1	1	2	2	2	1	1
X_3	1	3	8	17	7	3	1
X_4	1	3	16	85	18	4	1
X_5	0	2	6	16	9	3	1
X_6	0	1	2	3	3	1	1
X_7	0	1	1	1	1	0	0

Figure 39. Distribution of pixel readings for single incident electron events at 300 keV (a) before and (b) after the radiation damage test. The chip was maintained at -15 °C.

Comparing the single electron data obtained after $2.9x10^6$ electrons/pixel of accumulated electron dose on the sensor to the data obtained right at the beginning of the radiation test, we found out that the signal level generated by the 300keV electrons stayed almost the same (Figure 39). The noise of the sensor did not increase much as well, thanks to the CDS subtraction and pedestal correction, thus the SNR of the single electron detection remained unchanged. This indicated that if we could lower the leakage current even more, the sensor would be able to sustain even more radiation dose.

We used electrons/pixel to describe the accumulated dose, which is a convenient choice. The unit commonly used for radiation dose is Gray (Gy), and to do the

conversion, we need to use the deposited energy by the incident electrons. On average for a single 300keV electron, the energy deposited in the EM3 sensing volume is about 7keV and the volume for each pixel is $5x5x10\ \mu m^3 = 250\ \mu m^3$. Therefore, for a single electron, the energy deposited in the sensing volume = $7000 \times 1.6 \times 10^{-19}/250\ \ J/\mu m^3 = 4.48\ J/m^3 = 4.48/2.33 \times 10^{-3}\ J/kg = 1.92 \times 10^{-3}$ Gy, using the silicon density of $2.33 \times 10^3\ kg/m^3$. The dose of $3.3x10^6$ electrons/pixel is thus equal to 6.34 kGy or if using the Rad unit, 0.634 MRad.

To get a realistic idea about how many images the dose of $3.3x10^6$ electrons/pixel is equivalent to, we can do some estimation. In cryo-EM, the low dose condition requires the specimen dose not to exceed 20 electrons/$Å^2$. If we use 50,000 magnification, each 5µm x 5µm pixel on the EM3 would correspond to 1 $Å^2$ on the specimen. So for each cryo-EM image, the dose would be 20 electrons/pixel. So the DDD sensor is at least capable of acquiring 165,000 cryo-EM images ($3.3x10^6$ electrons/pixel). If the format of the DDD can be larger, say 3.5k x 4k pixels, each cryo-EM would be able to capture multiple single particles, say 20. It all sums up to about 3 million single particle images, enough to solve several single particle structures. For electron tomography, the typical imaging dose would be higher, but 200 electrons/pixel in each image would be plenty. The dose of $3.3x10^6$ electrons/pixel would equal to at least 16,500 images, enough to do 136 single-tilt tomographic data (each with 121 images, +/- 60 degree with 1 degree interval). In a typical high-throughput electron microscopy lab, the number of images mentioned above translates to at least three to six months of normal usage.

If a DDD sensor became unusable after a certain period of usage, it can be replaced. As only the sensor chip needs to be replaced, the cost and the procedure would be quite simple. The properties of the defects introduced in the sensor by the radiation also allow thermal annealing, a reverse process to radiation damage in which the positively charged traps are being filled again by electrons (Danchenko, Desai et al. 1968; Anelli, Campbell et al. 1999). Although the annealing process can reverse most of the damage by radiation, it cannot cure degradation due to some interface states.

Using the thermal annealing method, we successfully revived a sensor chip, by leaving the chip in an oven at 100°C for about 5 days. The leakage current of the sensor was reduced by at least 10 times and was able to be used again. With regular thermal annealing, we can expect the lifetime of the DDD sensors be prolonged and fewer replacements would be needed.

As explained in section 3.1.1.1, when operated in global reset CDS mode, the EM3 had a dead time that could be 50% of the total image acquisition time. As the sensor was illuminated during the dead time, it would reduce the total number of images the sensor could take over its lifetime. The issue was resolved in the EM5 prototype and will be explained in Chapter 4.

Chapter 4 Experimental Results from EM5

Although the design of the EM3 was largely successful, there were a few problems that existed. The sensor dead-time in the global reset CDS mode was most important as it unnecessarily increased the radiation damage to both the specimen and sensor. The noise in the EM3 system also limited the signal to noise ratio for electron detection.

To tackle these problems, a new prototype was designed. The EM5 not only fixed the problems found in EM3, but also allowed us to do imaging with 2-dimensional electron counting, which was found to improve the spatial resolution of the DDD system even further.

4.1 EM5 System

4.1.1 EM5 Sensor

The schematic of the EM5 sensor was shown in section 2.2.6. The sensor chip in EM5 was wire-bonded directly to a carrier board, as shown in Figure 40. The overlay on the photo showed how the sensor chip was aligned to the carrier board.

The main feature of the EM5 was its massively parallel on-chip per-column 10-bit Analog to Digital Converters (ADCs). Embedding the ADCs on-chip allowed us to do ADC conversions for an entire row of pixels at once (460 pixels in a row on EM5), which drastically improved the readout speed. The converted digital values will be transferred

off the chip using a 20-bit digital output. Using digital output instead of analog output in the EM3 minimized the readout noise from the supporting electronics board and overall helped to reduce noise of the system.

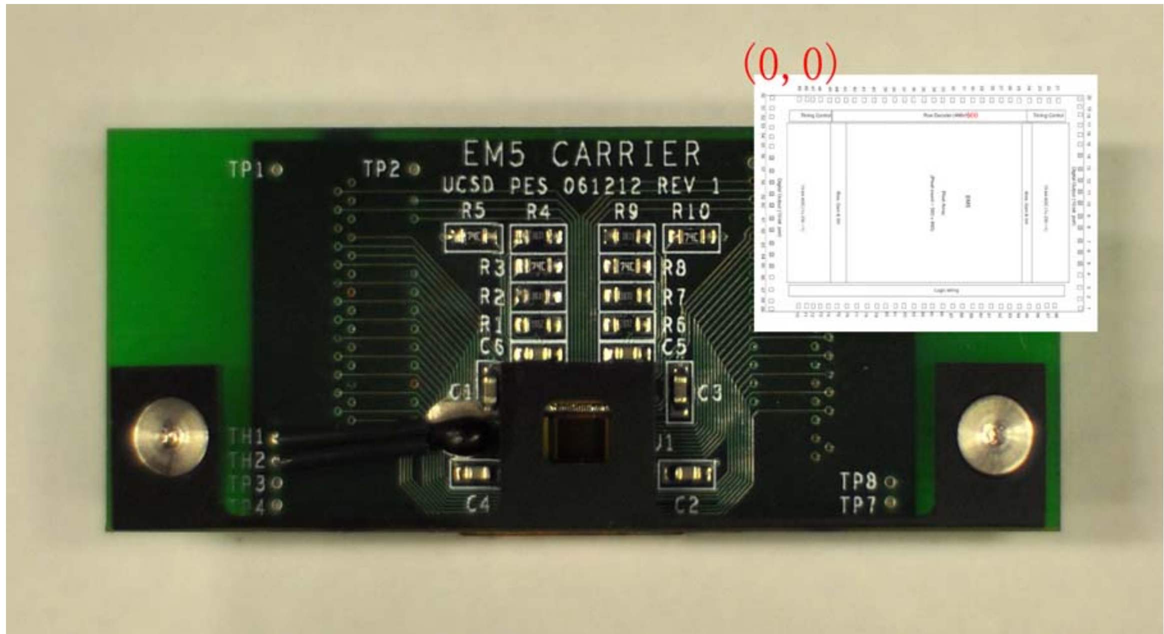

Figure 40. Photo of the EM5 carrier board with mounted sensor chip.

A single slope ADC design was chosen for its compactness and low power consumption. The ramp voltage was supplied off the chip, which could be used for nonlinear ADC operation. The output from the ADC was in gray-code, which would need to be converted to straight binary later in the data path. Power consumption was only 10 micro-amps or less per column.

4.1.2 Supporting Electronics Board

The EM5 carrier board with the sensor chip is directly plugged into the main supporting electronics board. As in the EM3 system, a Complex Programmable Logic Device (CPLD) with custom firmware provides proper timing and clocking to operate the sensor, and drives two 16-bit Digital to Analog Converters (DACs) to supply the voltage ramp for the on-chip ADC.

To monitor the temperatures at various places in the system, thermistor circuitry is integrated on the board. The mechanical shutter control and the Faraday plate amplification circuitry are also integrated, making the EM5 supporting board the most compact system in the five generations of DDD prototypes.

The digital outputs from the EM5 sensor are converted to Low-Voltage Differential Signaling (LVDS) to minimize problems with long cable length and allow high transfer rate (up to 100MHz in EM5). The LVDS outputs are converted back to single ended signals right before routing into the high speed digital acquisition card on the computer.

4.1.3 Mechanical Assembly and Cooling System

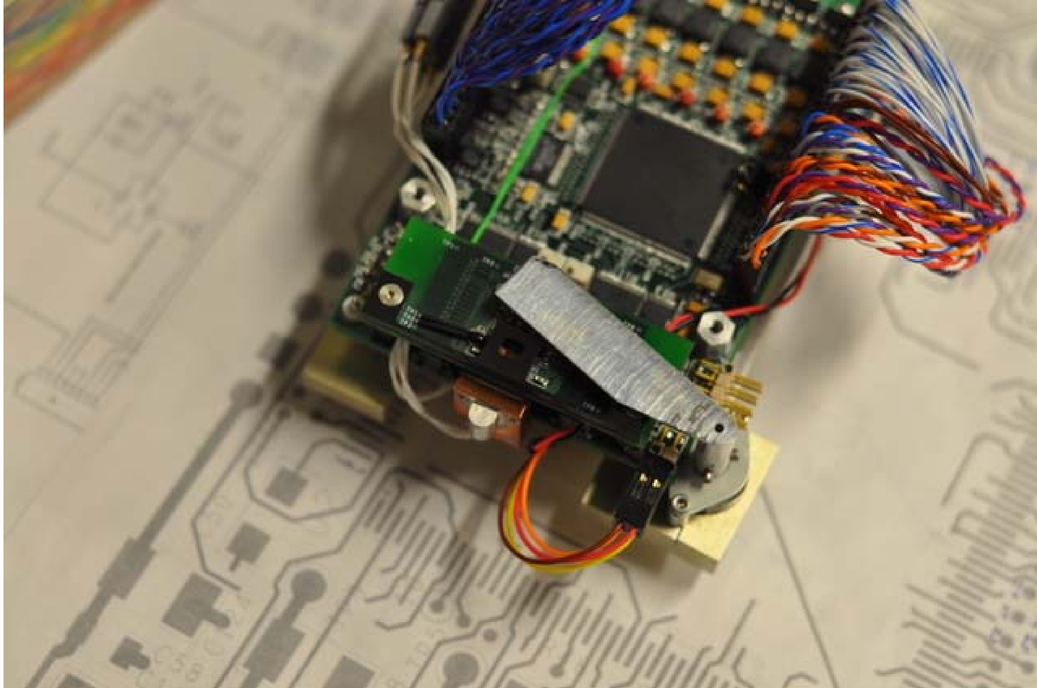

Figure 41. Photo of the supporting electronics board with the carrier board mounted. The mechanical shutter and the copper link between the sensor chip and the water cooling pipe were marked.

Figure 41 shows the EM5 carrier board mounted on the supporting electronics board. The mechanical shutter (made of aluminum) is also shown. The copper piece underneath the carrier board was a heat exchanger between the thermoelectric cooling module and the backside of the EM5 sensor. Water cooling pipes (as in Figure 42) passed through the vacuum interface and went right beneath the hot side of the thermoelectric module. A water chiller was used outside the vacuum.

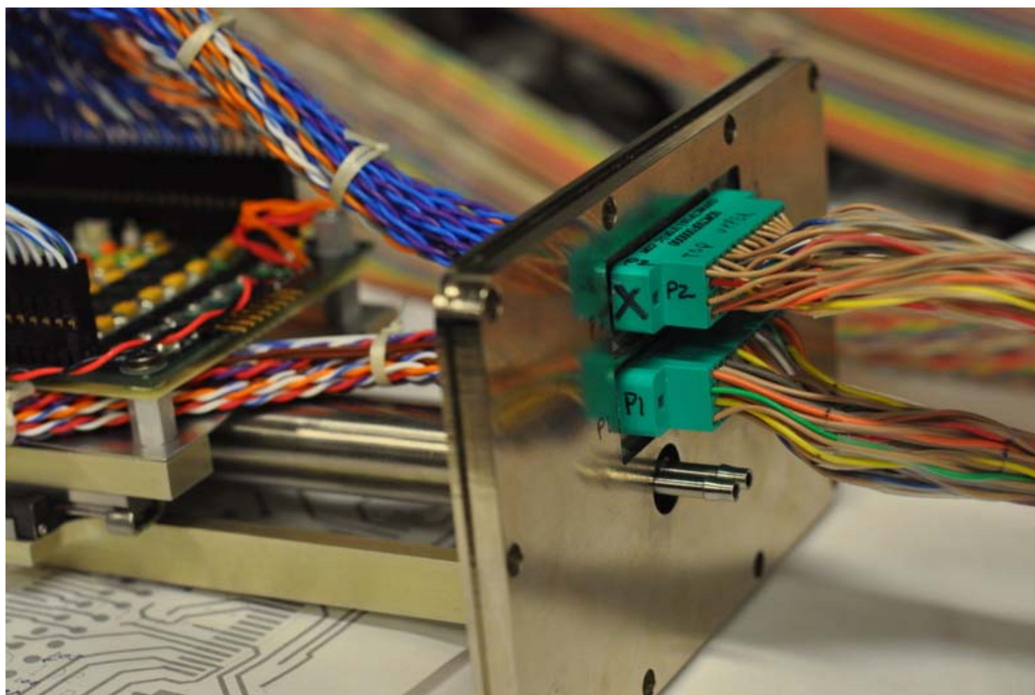

Figure 42. EM5 vacuum interface with water cooling pipes.

The compact size of the EM5 board and the cooling systems made it possible to adapt the system into multiple configurations. Using different vacuum interfaces, the EM5 system could be mounted in the film chamber of any JEOL microscopes, or in an adapter box at the bottom of the viewing chamber on any electron microscopes, by JEOL or FEI.

4.1.4 Peripheral Control Box

To tidy up the cables and boards in the system, we included a peripheral control box in the EM5. The cables from the vacuum interface connected directly to the control box first, before passing it on to the computer. The components in the control box

provided the power supply and LVDS to single ended conversions, as well as the shutter override and protection.

4.1.5 Computer System

In order to achieve the highest readout speed, we chose PCI-6552 100MHz Digital Waveform Analyzer card from National Instruments. The board accepts the 20-bit output from the EM5 sensor in a single clock and has an on-board 64Mbit/channel buffer memory.

A USB analog and digital input output box from Measurement Computing was used to control the mechanical shutter as well as monitoring the Faraday plate and thermistors. A custom program written in LABVIEW kept a log of the thermistor readings as well as the Faraday readings.

The main program for the EM5 image acquisition was also written in LABVIEW. It was re-written from ground up for the EM5, but had similar features as the EM3 control program.

Real time configuration changes could be made for the ADC digitization rate, transfer rate, reset pulse duration and the time delay between the two CDS reads. Data streaming to hard drive was assisted by using the buffer memory on the board as well as the PC memory to minimize any lag in the hard drive access. It was also possible to do continuous triggering to acquire multiple files automatically without user intervention. The real time image display function was capable of converting gray code into straight binary as well as CDS subtraction and pedestal correction. Averaging multiple frames

was also achieved in real-time with a minor delay compared with display frames without averaging.

The data file from EM5 was in uncompressed binary HWS file format from National Instruments. As it was a HDF5 based file format, it could be opened with any HDF5 capable software. The data files were normally parsed and converted into MATLAB data files for easier access and a set of MATLAB scripts were used for data analysis.

4.1.6 Timing for EM5

4.1.6.1 Rolling CDS Mode

Instead of resetting the entire pixel array at once (like in the global reset CDS mode in EM3), we implemented a new rolling reset CDS mode in the EM5 sensor chip. Only one row of pixels was reset at a time. To get the benefits of the CDS readout, the sensor array was also read out twice, but in quite a different fashion.

Figure 43 shows the rolling mode timing diagram. The sensor array is read out row by row. However, for any given row, we start by reading out that row, followed by a reset that is applied only to that row. Another read out of the same row is immediately acquired after the reset. The same read-reset-read procedure is repeated for each row in the pixel array.

After reading out all the rows, we would have completed the readout of one frame. The data in one frame can be organized into two reads. The first read was

constructed using only the row readout before the reset. And the second read was constructed using only the row readout after the reset. We needed more than 2 frames to get the CDS working. The second read of one frame and the first read of the next frame will be used for the CDS subtraction, as they correspond to the same pixel reset.

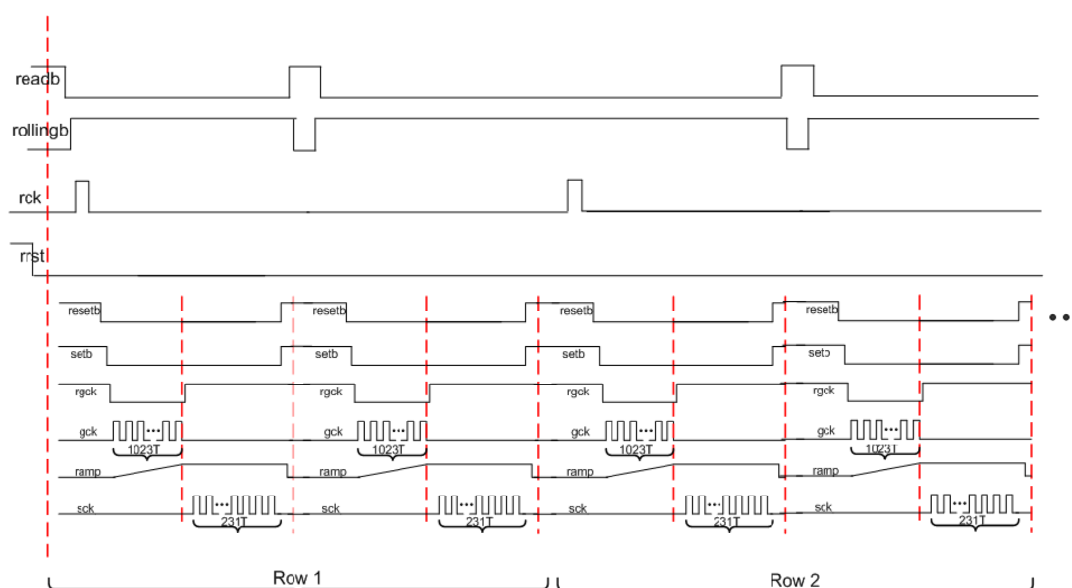

Figure 43. Rolling CDS mode timing diagram.

In this readout scheme, the sensor dead time is equal to the reset time of only a few microseconds per frame. As each frame takes at least a few milliseconds, the dead time in the EM5 using the rolling mode is effectively zero. As we discussed in Chapter 3, the zero dead time would be extremely helpful in minimizing the excess electron dose on the specimen and the sensor chip.

4.1.6.2 Pseudo-CDS Mode

To further improve the readout speed of the EM5, another mode of operation was designed in the EM5. It relied on the same pixel structure for the rolling reset mode but had special requirements for the op amp set up.

As shown in Figure 44, the pseudo-CDS mode had only one readout for each row, instead of two for the rolling reset CDS mode. When switching to one row, the input of the op amp of any pixel in that row was the pixel output with integrated charges in the photodiode. A series of switches (s1,s2,s3,s4) were opened and closed to set up the op amp to store that pixel output voltage on a capacity before the op amp input. The pixel reset was then asserted, and the pixel output swung back to the reset voltage, but as the input of the op amp was AC coupled, the voltage swing from the integrated level to the pixel reset level would appear at the output of the op amp.

The voltage difference between the voltage levels of the same pixels before and after the rolling reset was similar to the CDS subtraction in the previously described global and rolling reset CDS mode, but, because they were associated with two different resets, the reset noise would be additive and thus higher than the true CDS modes where subtractions were done between the two reads associated with the same reset. This readout method was called “pseudo-CDS” mode to differentiate it from the true CDS subtraction that we do in global and rolling reset modes. The advantage of the pseudo-CDS mode was that it only needed to read out every row once, therefore it substantially reduced the readout time.

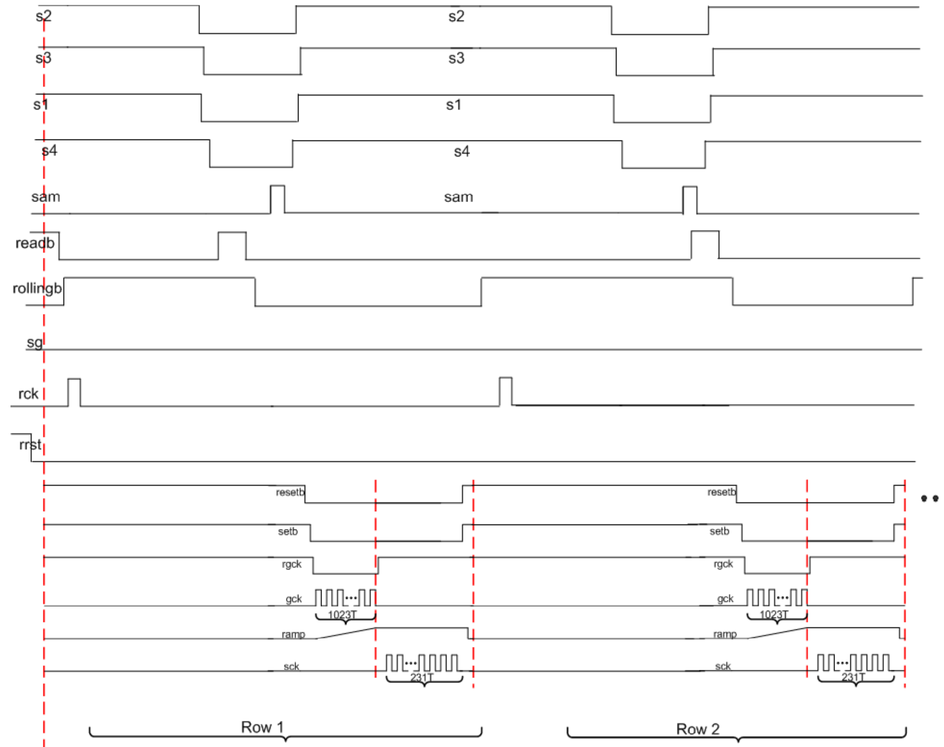

Figure 44. Pseudo CDS mode timing diagram.

4.1.7 Single Read Difference Mode

During the process of calibrating the EM5 sensor using electrons, we found out that there was an analog delay for the pixel reset circuit. To explain the behavior, we could focus on the voltage change of a single pixel over time first.

Typical changes in the pixel output voltage in the first and second reads of multiple frames are shown in Figure 45. Rolling reset CDS mode was used, but the first and second reads were re-aligned so that for each frame, the first and second reads were associated with one single reset. An incident electron hit the pixel in the 22nd frame after the first read, but before the second read, which represented most of the signal events

because the time between the second read and the first read of the next frame was negligibly small. The generated charges brought the output voltage down.

At the start of the next frame (23rd frame), the pixel was reset and the charges in the photodiode were being cleared out. However, if the reset was short (1.6 microsecond in the example here), some charges would still remain in the photodiode when the pixel was allowed to accumulate charge again. It could take multiple resets to clear out all the charges created by the signal hit. In the example here, it took about 20 resets, which counted to 32 microseconds in total for the reset.

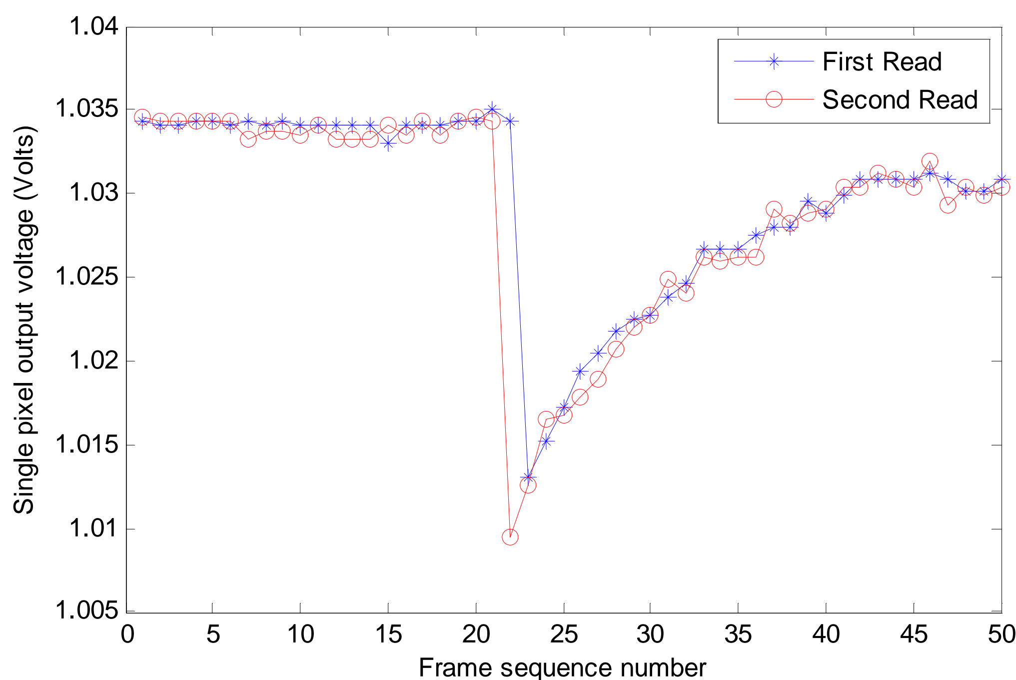

Figure 45. Changes in the output voltage of a specific pixel in the first and second reads of multiple frames. An incident electron hit the pixel in the 22nd frame.

The response of the pixel due to insufficient reset would not affect the CDS readout, as shown in Figure 46. Before the incident electron hit, the two reads of the sensor yielded similar voltages as it was determined only by the leakage current, which was small in this case. The CDS values (second reads subtracted from the corresponding first reads) stayed around 0, until the electron hit brought the read 2 of the 22nd frame to a lower voltage and producing a CDS value above the background noise, i.e. the peak in the plot.

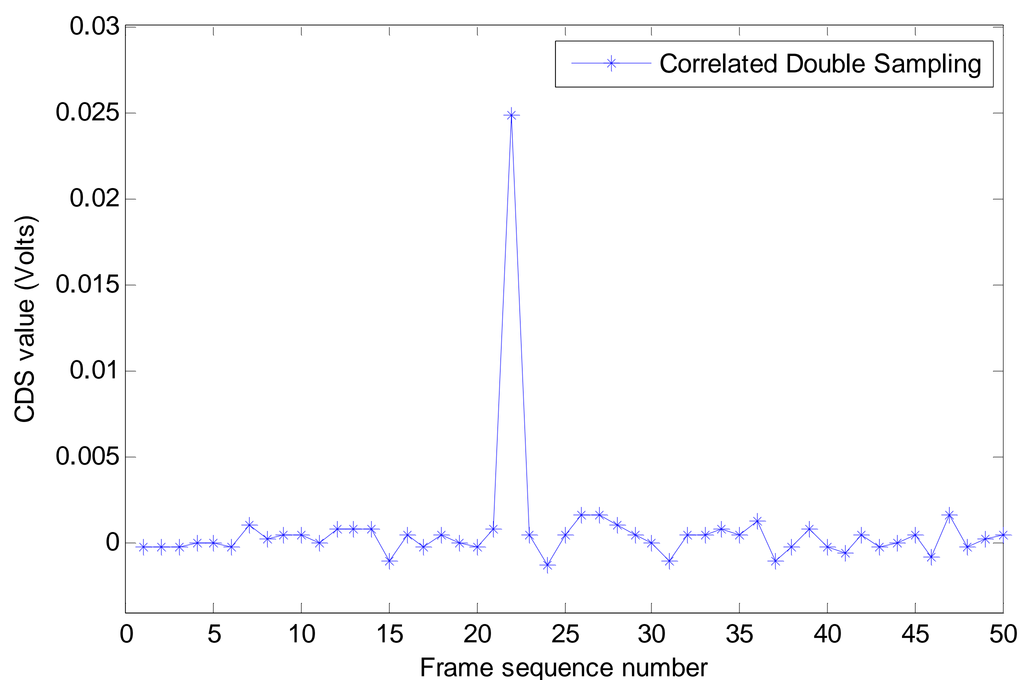

Figure 46. Values of each frame after CDS subtraction for the same data in Figure 45.

The pseudo CDS mode, on the other hand, would be heavily impacted by the slowly recovering pixel voltage with insufficient reset. The basic assumption of the pseudo CDS was that the pixel output would always settle to almost the same voltage

level after a pixel reset. However, this assumption broke down in this case outlined in Figure 45, where the read 1 of the 23rd frame was almost the same as the read 2 of the 22nd frame. The pseudo CDS readout that used the difference between these values would have yielded a much smaller peak almost buried in the background noise. Therefore, to make the pseudo CDS work more efficiently, we would need to allow enough time for the output to settle, i.e. the reset needed to be long enough. While the time to do a full reset only took tens of microseconds, if there were many rows of pixels, it added up to a large time delay and would limit the maximum frame rate.

To achieve high frame rate, we designed a new method that could utilize the pixel response for insufficient reset and required only a single read, which was called "Single Read Difference Mode".

From Figure 45, we observed that after the incident electron hit the pixel in the 22nd frame, the pixel output voltages in BOTH the first and second reads of subsequent frames followed each other and slowly recovered. If we only read out the first reads but kept everything the same, we would see a sudden jump of voltage in the 23rd frame, and the recovery was much more gradual compared to the rapid jump after the electron hit. This allowed us to use the difference between the voltage levels of the first reads in subsequent frames to detect an incident electron hit. The difference values for the first reads in subsequent frames in Figure 45 are shown in Figure 47.

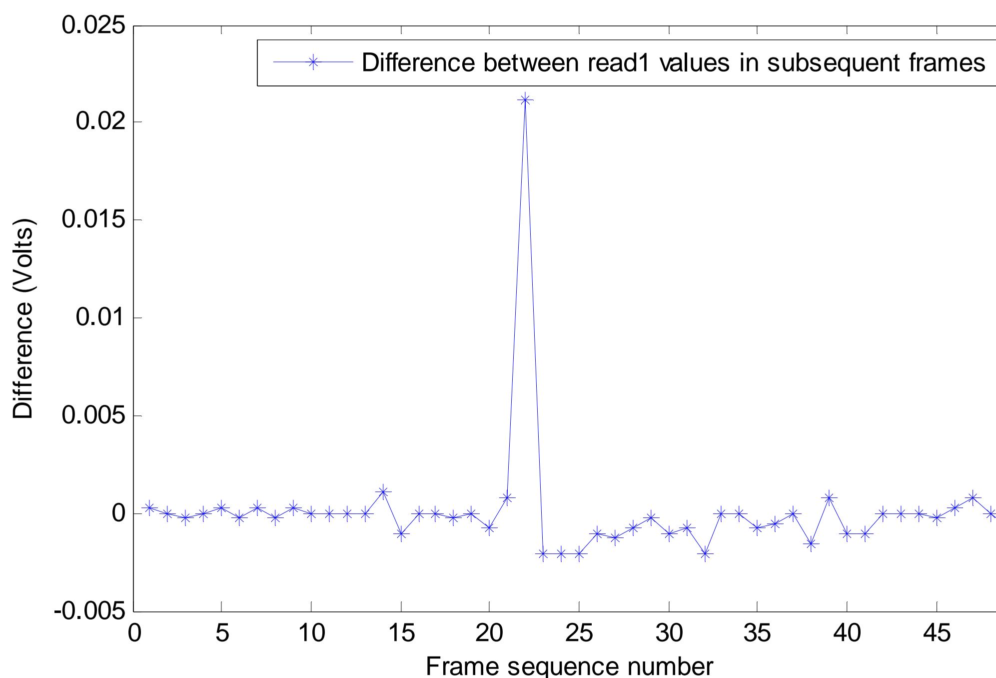

Figure 47. Single read difference values for the same pixel as shown in Figure 45.

Figure 47 demonstrates that it is possible to detect the incident electron hits using only the difference between the voltage levels of first reads in subsequent frames. Due to the pixel reset, the detected peak value using this mode would always be smaller, compared to that obtained in the rolling reset CDS mode. Therefore, this mode cannot be used for accurate measurements of the deposited energies by the incident electrons, but it would work well for detecting electron events. As the method required that the single reads must be performed near the start of the recovery curve, the time between a pixel reset and reads could be essentially zero and the method would be even faster than the pseudo CDS method which relied on enough delay time after the pixel reset. One potential challenge with this method was that it might fail if a lot of incident electrons were hitting the same pixel and the pixel output stabilized around a certain voltage and

never showed the recovery pattern. However, under relatively low dose condition, this scenario was very unlikely to happen.

4.1.8 Readout Frame Rate

The EM5 was designed with a maximum ADC rate of 100MHz, and a data transfer rate of 100MHz. With the flexible design of our supporting electronics board, we can also clock the sensor at a slower speed such as 12.5MHz, 25MHz, or 50MHz. The ADC rate and the data transfer rate can be independently changed, allowing any combination of the four choices.

To obtain the different frame rate of the system at different ADC and transfer rates, the total frame acquisition time should be broken into different contributors and analyzed. If we chose 100MHz for both the transfer and ADC rate, we should be able to calculate the highest frame rate of the system.

Starting with the contribution from the ADC conversions, for 10 bit resolution, we needed 512 clocks, which translated to 512 x 10ns = 5μs for one read of a row of pixels if 100MHz ADC rate was used. As the transfer bus was 20 bits wide, the digital values from 2 pixels can be transferred on a single transfer clock, if using 100MHz transfer clock, one row of pixels (460 pixels in a row) would need 460/2 * 10ns = 2.3μs. The pixel reset could be independently changed from less than 1μs to 100μs. Similarly the integration time delay was programmable from zero to 1 second. For maximum frame rate, the integration delay was always set to zero. To set up some digital logic in the

sensor, there were some other required timing delays in the range of 100ns to 500ns, which we would ignore for now.

Combining these contributors together for the rolling reset CDS mode, we can get that for each row of pixels, we would need: 5μs of ADC + 2.3μs of transfer + 1μs of reset + 5μs of ADC + 2.3μs of transfer = 15.6μs (read + reset + read). Summing up for the entire 560 rows, we got roughly 8.7ms of total frame acquisition time, or 115 frames/second.

As for pseudo CDS mode, we would need to increase the reset time. As we might need 10-30μs of reset per row, the frame rate became limited by the reset time. Assuming a 20μs reset time, each row would need: 20μs of reset + 5μs of ADC + 2.3μs of transfer = 27.3μs, and the total frame time would be 15.3ms or 65 frames/second.

Lastly for the single read difference mode, the reset time could be less than 1μs. Assuming just 1μs of reset time, each row would need: 5μs of ADC + 2.3μs of transfer + 1μs of reset = 8.3μs, and the total frame time would be 4.6ms or 217 frames/second.

The calculations above all assumed that we use the full 10-bit ADC resolution, and if we were to lower the resolution to 8-bit, further speedup was possible. For each row of pixels, the ADC conversion would require only 128 x 10ns = 1.28μs, and the total frame time for single read difference mode would be only 2.56ms per frame, or 390 frames/second.

Running the EM5 at the highest speed continuously required the high speed digital input acquisition board to keep up. However, the limited PCI bandwidth and

limited buffer memory on board had an impact on the total frames that could be acquired continuously. Successful acquisitions of 250 frames in the rolling reset CDS mode or 500 frames in the pseudo CDS or single read difference mode were achieved. The acquisition could be restarted again once the data acquisition board completed the data transfer from its on board memory to the PC memory, which took at most 1-2 seconds.

4.2 EM5 Calibration

The pixel structure of the EM5 was almost the same as the EM3, so we expected the same analog responses from the X-ray photons or high energy electrons. However, the on-chip ADC and op amp brought about changes that required a full calibration on the EM5.

4.2.1 Gain and Offset Calibration for the On-chip Op Amps

To calibrate the gain and offset of the op amp before the on-chip ADC, we took advantage of a test switch in the sensor and connected a test voltage to the inputs of every op amp before each column ADC. The pixel outputs were disconnected from the input to prevent interference.

The 460 op amps were configured in unity gain mode, but could still have minor differences in gain, and the output of the op amp *Vout* should follow a linear relationship to the input voltage *Vin*, as Vout = Vin*Gain+ Voffset.

The test voltage was set to 1V and 0.8V. At each voltage, one frame was acquired using the rolling reset CDS mode. Because the pixel array was not connected at all, the

reset had no effect on the output, and the two reads in this mode were simply sampling the same voltage. Additionally, the op amps were per-column, 560 samples were obtained for each op amp.

Averaging the pixel values from the 560 samples in either read 1 or read 2 of the acquired frames would establish the two points to fit a line and obtain the gain and offset for each op amp. The test voltage could be set to more values and more accurate results would be obtained.

Figure 48 shows the histogram of the gain values for the per-column op amp obtained using this calibration method. The gain varied from 0.99 to 1.005 and the most probable value was at 1.0006, very close to unity.

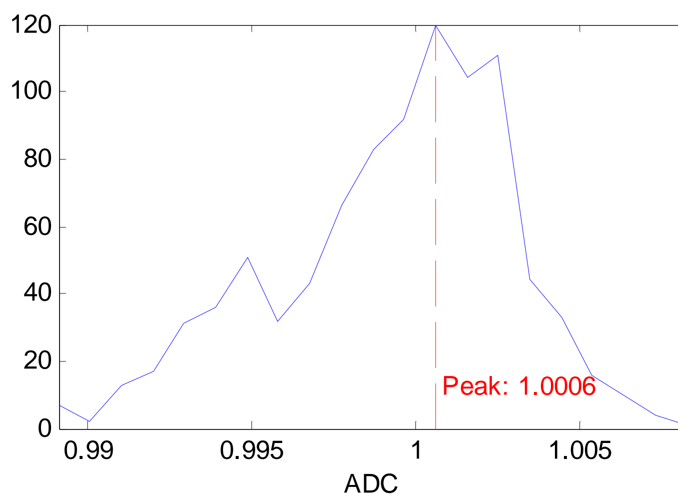

Figure 48. Histogram of the gains of the per-column op amps before the on-chip ADC.

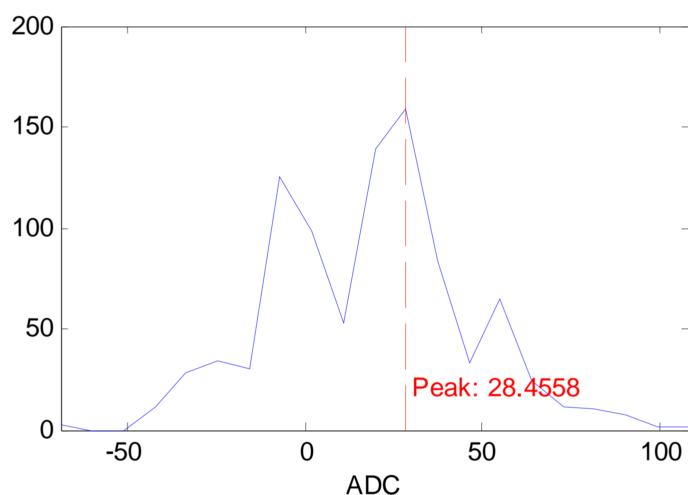

Figure 49. Histogram of the offset voltages of the per-column op amps before the on-chip ADC.

The offset voltage of each op amp showed a much larger variation, as in Figure 49. It varied from -50 ADC units to +100 ADC units. As 1024 ADC units was equal to 268mV, the variation in terms of millivolts was from -13mV to 26mV. As a fixed pattern, this offset voltage from the op amps would be corrected in all the three readout modes.

4.2.2 Leakage Current Calibration

The leakage current of the EM5 was measured using the same method as in section 3.2.1. The measured leakage current at room temperature (26°C) was at 0.061 mV/ms and it dropped to 0.007 mV/ms at -19°C. Compared to the EM3, with 0.26 mV/ms at room temperature and 0.049 below 1.2°C, the leakage current in EM5 was significantly smaller.

As the analog pixel circuit including the photodiode did not change much from EM3 to EM5, the reduced leakage current could only be explained by the improvement in CMOS processing. The recent popularity of CMOS imaging sensors used in the consumer market has motivated the fabrication facilities to tweak their process to reduce the leakage current.

With an integration time of 8.8ms in the rolling reset CDS mode, the accumulated leakage current in the pixel was only 8.8*0.007 mV = 0.062 mV when the sensor was operated at low temperature (< -19°C). The ADC to voltage conversion in the EM5 was variable, but it was always larger than 0.2 mV per ADC. It appeared that we would not need to do pedestal correction anymore as the leakage current corresponded to lower than 1 ADC unit. However, as the leakage current measured was based on the values for the most probable peak, the spread of the leakage current values for all the pixels in the array was actually large. As an example, 250 frames were acquired in the rolling reset CDS mode at low temperature. Only CDS subtraction was performed before averaging all the frames together to yield the average image, which contained contributions from the leakage current and noise. Figure 50 shows the histogram of the pixel values in the average image. The most probable peak in the histogram was at 0.2mV, less than 1 single ADC unit (0.26mV/ADC), however the spread was almost 4mV. Therefore, pedestal correction was still needed for accurate measurements of the energy deposition.

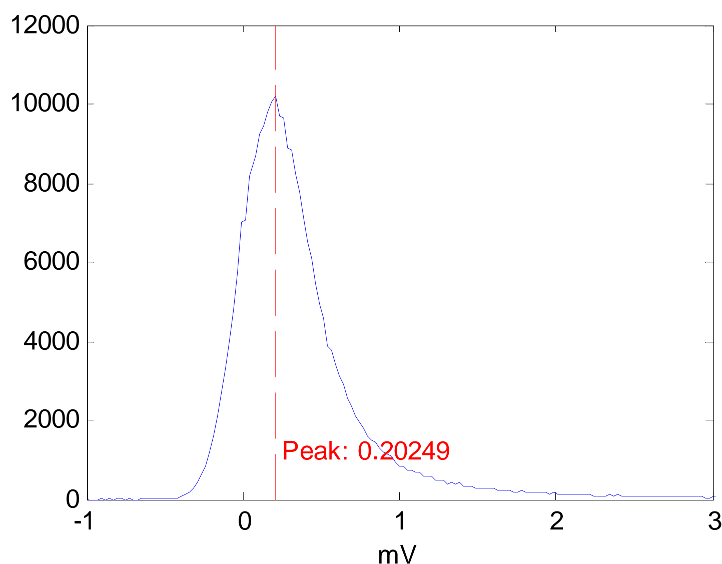

Figure 50. Histogram of the pixel values in the average image obtained in rolling reset CDS mode at -20°C. Only CDS subtraction was performed before averaging the 250 frames together.

4.2.3 Measured Total Noise after Correction

The method in Section 3.2.3.2 used the histogram of all the pixel values after CDS subtraction and pedestal correction to obtain the total noise. The method did not take into consideration that each pixel in the array could have a different gain, due to the variation in the op amp from the per-column ADC as well as the slight variations in resistance or capacitance in the pixel transistors.

To accommodate the pixel gain variations, we used a new method in the EM5 to measure the noise of each pixel separately. A large number of frames (usually 250) were taken at a certain setting and then CDS subtracted. This way we got at least 250 samples for each pixel in the array, and the standard deviation for each pixel could be calculated.

The standard deviation calculated for each pixel this way would be equivalent to the root mean squared noise (RMS) noise. Here, pedestal correction was not a necessary step, as the standard deviation calculation automatically accounted for the mean value subtraction in its algorithm.

Using this method, 250 frames were obtained in the rolling reset CDS mode at -29°C, and the histogram of all the standard deviation values for the pixels was shown in Figure 51. The most probable peak was at about 0.465mV, with a spread of 0.177mV FWHM.

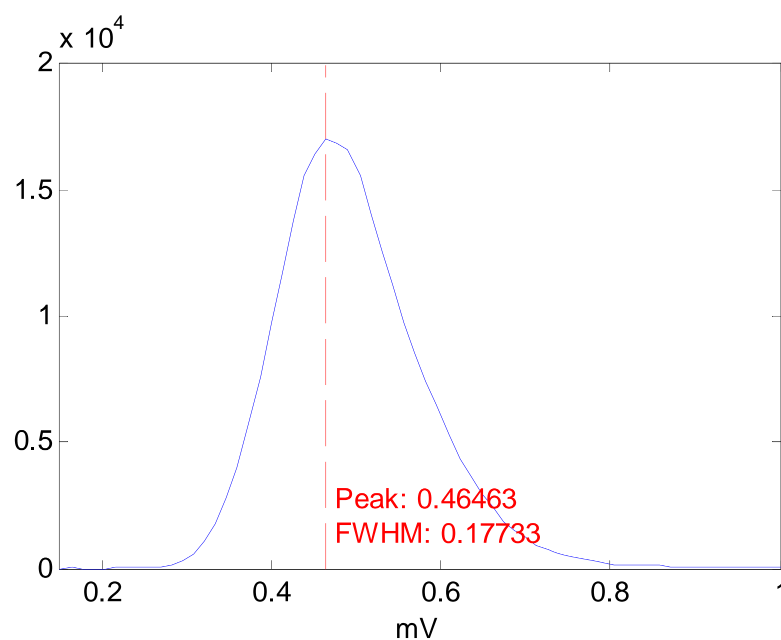

Figure 51. Histogram of all the standard deviation values for all the pixels in the EM5 sensor. Data was acquired at -29°C.

As measured in section 4.2.2, the leakage current is so small that the dominant contributor to the 0.465mV noise was the readout noise. As the readout noise did not depend much on temperature of the sensor, the RMS noise measured in each would in turn show little dependence on temperature. This was confirmed by repeating the same experiment at +16°C. As shown in Figure 52, the noise increased only a little bit to 0.53mV.

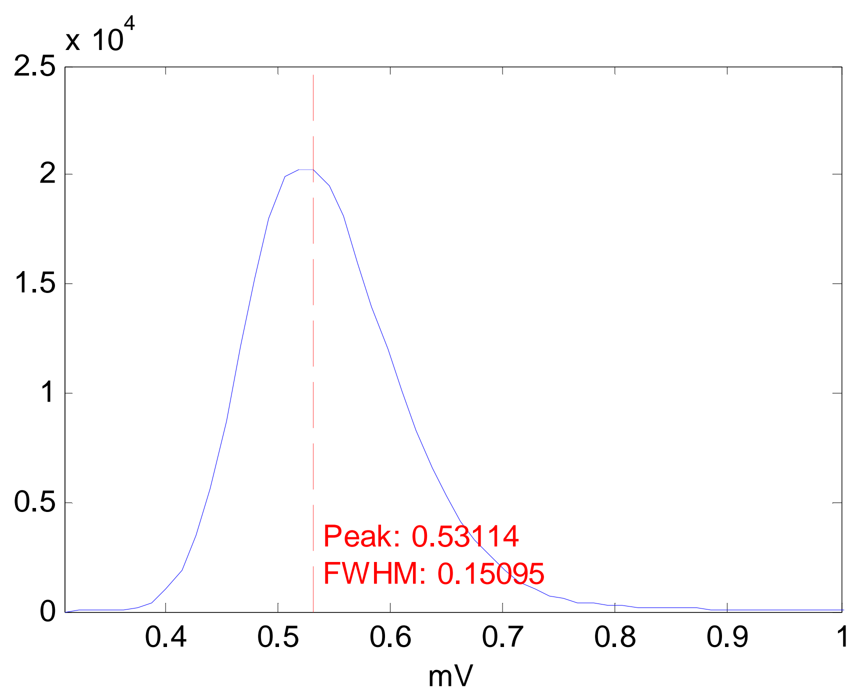

Figure 52. Histogram of all the standard deviation values for all the pixels in the EM5 sensor. Data was acquired at +16°C.

The same method used in the EM5 was applied to the EM3 data, and a standard deviation of 3.5 ADC or 1.7mV was obtained at room temperature. The lower noise in the EM5 system helped to improve the signal to noise ratio and allowed us to use a smaller threshold for detection of single electron events.

4.2.4 Device Calibration Using X-ray Photons

As in section 3.2.4, the energy conversion ratio of the EM5 was determined by experiments using the ^{55}Fe X-ray photon. With the lower noise in the EM5, the threshold to detect photon hits in the sensor was set to 8 times the noise standard deviation, equal to 4mV. The detection algorithm was also improved to use cluster analysis, which will be explained later in the single electron hits section.

With a low threshold, the detected events could have two or more pixels above the threshold. To avoid double-counting, only the pixel with the highest value would be used as the center of the event, or the peak pixel for that event. After processing 2500 frames of ^{55}Fe X-ray photon data, 2939 events were detected. The histogram of the peak pixels is shown in Figure 53, and the peak corresponding to 5.9keV X-ray photon was found at 38.7mV.

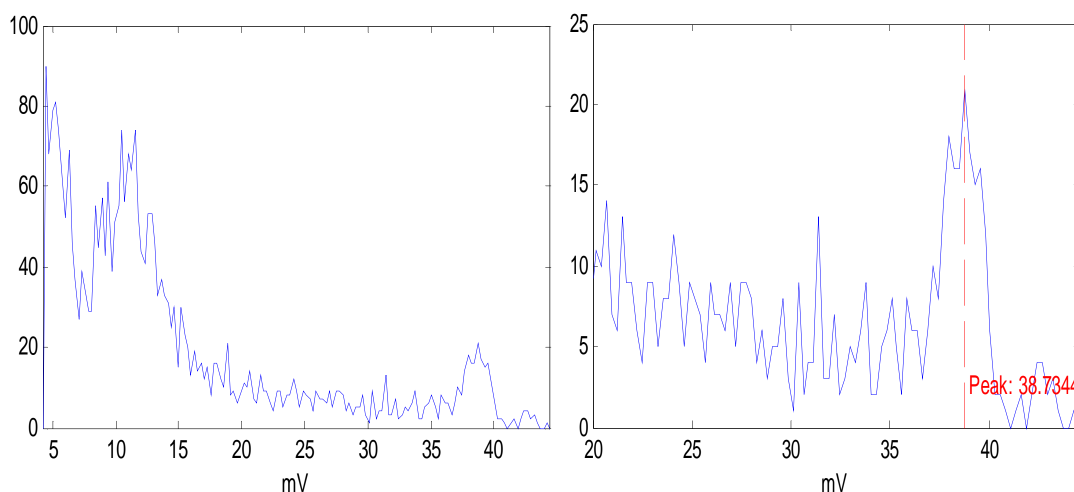

Figure 53. The histogram of the peak pixels in detected ^{55}Fe X-ray photon hits. The plot on the right showed the values around the 5.9keV signal peak.

The energy conversion was thus calibrated at 0.024mV per ionization electron, almost the same as the 0.025mV/electron obtained from EM3. This agreed with our expectation as the analog circuit in EM5 was kept the same as the EM3.

The total noise of the system was estimated at 19 electrons at -19°C and 22 electrons at +16°C. The leakage current could also be converted to 2.54 electrons/ms at 26°C and 0.29 electrons/ms at -19°C.

From the detected ^{55}Fe events, a 7x7 matrix can be obtained around the peak value and the average of all these matrices yielded the average matrix as shown in Table 5. Most of the signals were contained in the 3x3 matrix around the center pixel, whose value contributed to almost half the total signal. The sum of the average matrix came to 119 ADC, which was converted to 31.1mV, less than the 38.7mV calibration peak. One explanation could be that we might have included events coming from the photon absorption in the silicon substrate near the interface with the epitaxial layer. The signal charges generated near that interface could diffuse into the epitaxial layer and be collected in the photodiode. However in these events, the signal charges only corresponded to a portion of the total energy deposited by the photon, as the recombination rate was much higher in the silicon substrate. Counting these events in the average matrix would make the sum of the matrix smaller, compared to the calibration peak, which corresponded to the total absorption of the photon near depletion region of the photodiode.

Table 5. The 7x7 average matrix from the ^{55}Fe events in EM5.

0	0	0	0	0	0	0
0	0	1	1	1	0	0
0	1	4	9	4	1	0
0	1	9	55	9	1	0
0	1	4	9	4	1	0
0	0	1	1	1	0	0
0	0	0	0	0	0	0

4.3 Detector Responses from Beam Electrons

4.3.1 Uniform Electron Illumination

As the X-ray photon calibration experiment suggested, the EM5 sensor response to high energy electrons would be similar to the EM3 results in section 3.3.1.

Figure 54 shows the average signal response from the EM5 to different intensities of 200keV electron beam. The slope of 66.44mV per incident electron can be converted to 10keV, a bit larger than the 8.57keV measured from EM3. The difference might have come from the slight difference in the epitaxial layer thickness. As the epitaxial layer in EM5 was 10 μm (measured in section 2.1.2), the epitaxial layer of EM3 might have been thinner (within the 8-10 μm range given by the chip fab).

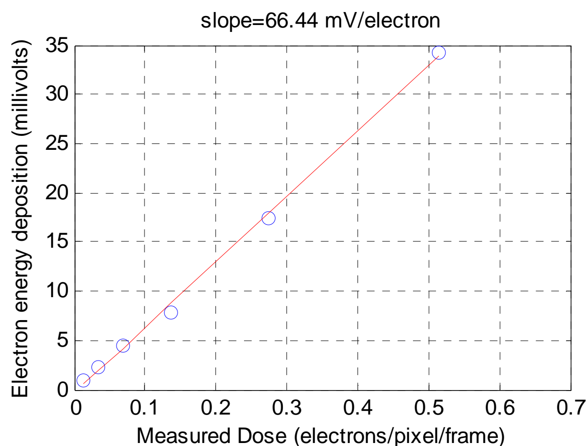

Figure 54. The average response of the EM5 sensor to uniform 200keV electron illumination at different intensities.

As expected, for 120keV electrons (Figure 55), the slope was higher than for 200keV electrons, as the lower energy electrons deposited more energy in the epitaxial layer. The slope of 111.5mV per incident electron converted to 17keV also larger than the 14keV obtained in EM3.

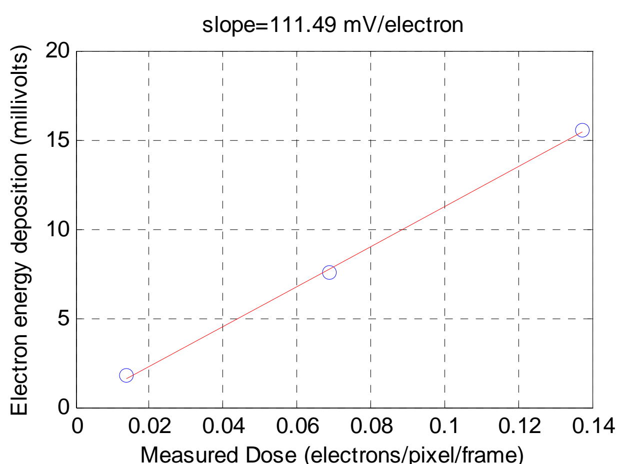

Figure 55. The average response of the EM5 sensor to uniform 120keV electron illumination at different intensities.

In both figures, the measured dose only extended to a maximum dose less than 1 electron/pixel/frame. As the EM5 was operating at 115 frames per second, the conversion factor to pA/cm^2 could be calculated to be 1 electron/pixel/frame = 73 pA/cm^2, much higher than the conversion of 1 electron/pixel/frame = 11 pA/cm^2 in EM3.

To match the least significant bit (LSB) of the 10-bit on-chip ADC to the noise in the system, the ideal ADC conversion would be 1 ADC = 0.5mV. Therefore, the full range of the ADC would correspond to 0.5 x 1024 = 512mV. As the results from 3.3.1 showed, the EM3 started to saturate at a bit less than 1 volt, and we expected the full range of the EM5 to be around 1 volt as well, which would be almost double the full range of the 10-bit ADC. Another factor that also limited the dynamic range was the voltage differences between pixels (the fixed pattern noise). Although CDS subtraction would eliminate the effects, the two CDS reads in each frame still had the fixed pattern in them. Some pixels in the array would therefore reach saturation earlier than the others due to the baseline voltage differences, and the CDS subtraction for these saturated pixels would become invalid. One source of the fixed pattern comes from the op amp offset voltage (measured in section 4.2.1) and it could be eliminated if the op amp was designed with a reference voltage to correct for offset. Unfortunately, this was not possible in the current EM5 design.

4.3.2 Single Electron Hits

As in section 3.3.2, we collected a large number of frames after lowering the beam intensity to a level that only a few electrons were hitting the sensor during each

integration time. Events from the single electron hits were searched in the images and analyzed.

Table 6. The 7x7 average matrix from detected 120keV single electron events in EM5.

1	1	2	2	2	1	1
1	2	4	6	4	2	1
2	4	14	26	14	4	2
2	6	26	94	26	6	2
2	4	14	26	14	4	2
1	2	4	6	4	2	1
1	1	2	2	2	1	1

Table 6 shows the average matrix from detected 120keV single electron events (162300 events in total). Most of the signal was contained in the 5x5 array near the peak value, while the small signal tail extended to a 9x9 matrix. Summing up all the charges in a 11x11 matrix, we got a total sum of 400 ADC, corresponding to 105mV, which was in good agreement with the result of 111.5mV per incident electron using uniform beam illumination.

The average matrix from 200keV single electron hits (304203 events) is shown in Table 7, where the 11x11 sum was obtained at around 210 ADC or 55mV. Although it is smaller than the result of 66mV per incident electron obtained from the uniform beam illumination, it is still in a much better agreement, compared with the EM3 single electron data in the section 3.3.2. The improvements were due to a smaller detection threshold for events in the EM5, thanks to the low noise characteristics.

Table 7. The 7x7 average matrix from detected 200keV single electron events in EM5.

0	1	1	1	1	1	0
1	1	2	3	2	1	1
1	2	8	16	8	2	1
1	3	16	64	16	3	1
1	2	8	16	8	2	1
1	1	2	3	2	1	1
0	0	1	1	1	1	1

To demonstrate how the threshold affected the average matrix, we filtered the detected single electron events using different threshold values. With a higher threshold, more events would be filtered out as they did not have any pixel that exceeded the threshold. The number of events that would still be detected at each threshold setting was normalized according to the total number of events when we started.

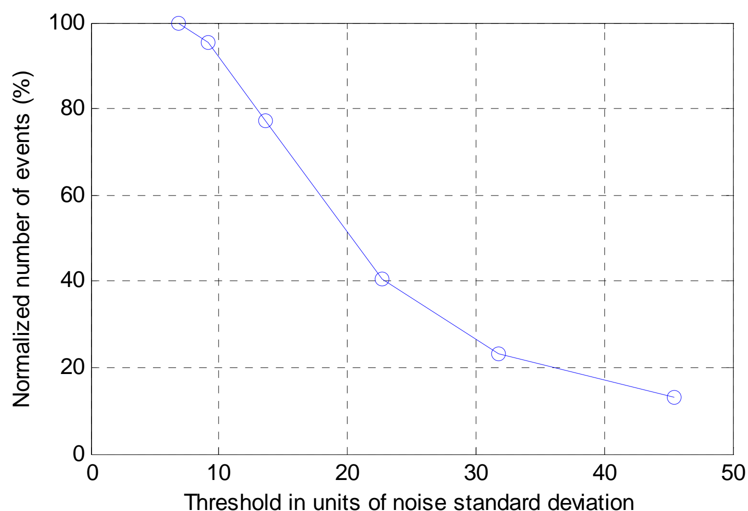

Figure 56. The normalized number of remaining events after filtering out the events with different threshold values, expressed in multiples of the RMS noise.

The result is shown in Figure 56. The number of events significantly dropped down when a higher threshold was applied. The filtering process with a high threshold also favored the events with large signals, so the average matrix obtained would be biased.

The results in Figure 56 could be further explained by looking at the histogram of the peak values in the detected single electron events at 200keV, shown in Figure 57. Because of the signal spread in multiple pixels, the peak pixel values in most events were smaller than the average value. In fact, the most probable peak was only 31 ADC (or 8.1mV), compared with 64 ADC (or 16.8mV) as in Table 7. The most probable peak corresponded to roughly 17 times the RMS noise and that was approximately where the detected events in Figure 57 dropped to 50%.

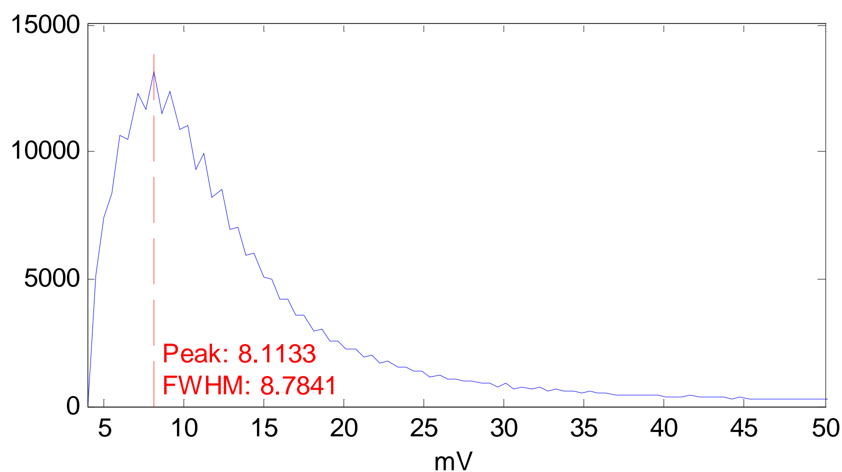

Figure 57. Histogram of the peak values from single electron events at 200keV.

To ensure the detection of most single electron events, the threshold had to be small enough. In the case of the results from EM3 in section 3.3.2, the signal from the

incident electron should be similar, but the threshold was 40 ADC or 19.5mV. As the noise in EM3 was 3.6 ADC or 1.76mV, the threshold was about 11 times the RMS noise, but as it was higher than the most probable peak, a lot of the events were buried in the background and did not get detected. As a threshold of 19.5mV would correspond to roughly 42 times the RMS noise in EM5, we expected that only 15% of the total electron events were detected in the EM3 results.

The EM5 showed that it was possible to detect almost every single electron hit from the beam electrons at a high frame rate, and it could be used as a 2-dimensional electron counter.

4.4 High Speed 2-D Electron Counter Imaging using EM5

An ideal 2-D Electron Counter would be a 2-dimensional sensor array with each pixel to be able to count the number of incident electrons hitting that pixel. The final image would be formed by the total counts in each pixel.

The EM5 was not exactly designed for counter operation, however, with its single electron detection capability, it was possible to be used as a counter.

4.4.1 Optimized Operation Mode for Electron Counting

The single electron hits experiments in section 4.3.2 were performed with very low beam intensity so that only a few electrons were hitting the entire sensor array during the frame integration period. Using such a low dose would require an unrealistic long time to accumulate enough electron counts, so a higher dose would be needed. However,

if the dose was too high, the electron events would be too close to each other and it became impossible to distinguish individual hits, thus making it impossible to do electron counting.

On average most of the energies deposited by 200keV electrons were within 5x5 pixels, so it would be reasonable to assume that if the surrounding 5x5 area around a given electron hit did not have another electron hit, we would have no problem detecting it.

Using a simple simulation, we were able to simulate different levels of electron dose and determine the percentage of events that have another electron hit nearby (in a 5x5 area). For easy understanding, the electron dose was expressed in terms of 1 electron hit in a matrix of certain size. For example, 1 electron in a matrix size of 11 by 11 was equivalent to 1/121 electrons/pixel/frame. With the increase in matrix size, the electron dose became smaller.

The result of the simulation is presented in Figure 58. Even when the electron dose was lowered to 1 electron per 15x15 pixels = 0.0044 electrons/pixel/frame, there was about 10% of chance that the electron hits would be close to each other. If we were a bit more aggressive and went to 20%, the maximum dose was estimated at around 1 electron per 9x9 pixels = 0.012 electrons/pixel/frame.

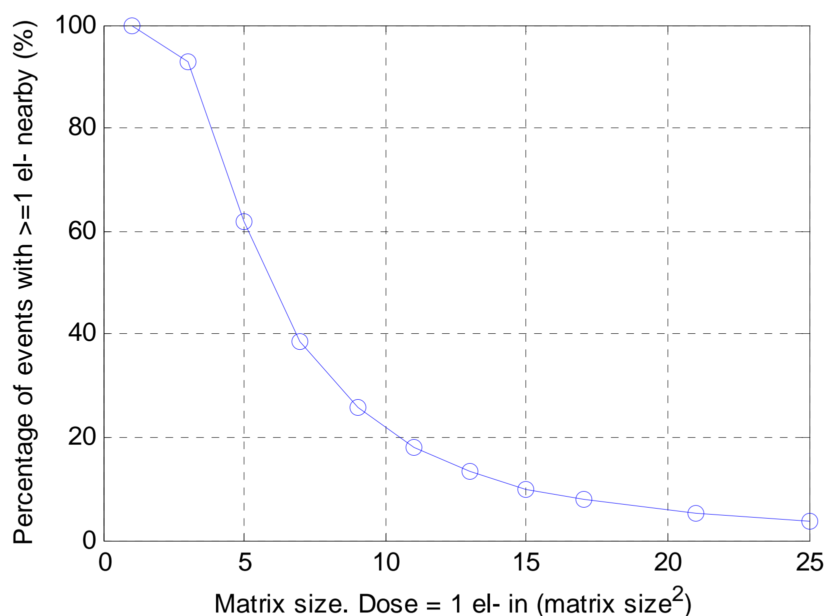

Figure 58. The percentage of events with an electron nearby, in respect to the matrix size, which would be equivalent to an electron dose of 1 electron in (matrix size)^2 pixels.

The incident electron dose was only part of the story. We would also need to consider the total number of frames and the frame rate for taking images.

As described in section 3.4, if we were to take an image for cryo-EM at 50,000 magnification, each pixel of the EM5 would accumulate 20 electrons in a single image to satisfy the 20 electrons/Å^2 dose limitation.

Using 20 electrons per pixel as the minimal required dose for the final image, and a maximum dose of 1 electron per 9x9 pixels, we would need 1620 frames. With a frame rate of 115 frames per second in rolling reset CDS mode, the EM5 could acquire the data within 14 seconds, which was in a reasonable range if the specimen was stable.

To achieve high efficiency detection, we could not increase the electron dose too high. The only factor that could be improved was the frame rate. As calculated in the section 4.1.8, the highest frame rate was achieved in the single read difference mode. The single read difference mode was not being used in the previous sections, because it was not accurate in measuring the energy deposition. However, in terms of electron event detection, it was almost as efficient as the rolling reset CDS mode.

The single read difference used almost the same timing as the rolling reset CDS mode, except that it needed only a single read in each frame. It was thus possible to use the rolling reset CDS mode to simulate the operation of single read difference by keeping only the CDS read which was performed right after pixel reset. Using the rolling reset CDS frames used for the detection of single 200keV electron hits, a simulated set of single read difference frames was obtained.

By detecting electron hits in the simulated single read difference frames, we were able to find 303039 events, which was less than the total number (304203) found in the rolling CDS mode by 0.4%. The RMS noise for each pixel in the single read difference mode was also around 0.5mV, so the same threshold was used for single electron event detection.

The average matrix from the detected events in Table 8 confirmed the fact the single read difference mode would yield a smaller signal. Comparing the values in the average matrix to those in Table 7, the peak pixel value was reduced from 64 ADC to 56 ADC in the single read difference mode, an 8 ADC reduction or 2.1mV (0.32keV). The surrounding pixels, however, remained almost the same, showing only small reductions

in values. All in all, the single read difference mode showed a great potential in maintaining the detection efficiency as in the rolling reset CDS mode, while improving the frame rate.

Table 8. The 7x7 average matrix from detected 200keV single electron events using the single read difference mode.

0	0	1	1	1	0	0
1	1	2	3	2	1	0
1	2	7	15	8	2	1
1	3	15	56	15	3	1
1	2	7	15	8	2	1
0	1	2	3	2	1	0
0	0	1	1	1	0	0

The maximum frame rate obtained using the single read difference mode at the full 10-bit resolution was 217 frames/second. To obtain the same 1620 frames necessary for the final image of 20 electrons per pixel at a dose of 1 electron per 9x9 pixels, we would need only 7.5 seconds, compared to the 14 seconds in the rolling reset CDS mode.

Because of the limitation in data transfer, the EM5 system could only acquire 500 frames in single read difference mode or 250 frames in rolling reset CDS mode. Continuous triggering was possible, but the next burst of frames would need to wait 0.5 second or so for the acquisition board to transfer the data from its on-board memory to the computer memory. If the electron beam was left on the specimen and the sensor, it would have introduced roughly a 20% dead time if multiple bursts were required. This

dead time could be reduced if the acquisition was synchronized with the beam blanker in the microscope.

4.4.2 Cluster Analysis and Selection

Although the average matrix from the detected single electron hits was quite symmetric in shape, the matrix from individual single electron hits could take a complex shape. Cluster analysis was used to quantitatively measure the shape of the events, and thus provides a measure for further selection or categorization of the events.

The first step of the cluster analysis was to convert an image containing multiple electron hits into a binary image. Any pixel that had a value above the threshold would mark a 1 in the binary image, while the pixels with smaller values would be represented by a 0.

All the 1s in the binary image were then divided into multiple clusters, corresponding to multiple electron hits. Each cluster could contain one or more pixels, but they would have to be binary connected (8-neighbor). For each cluster, the total number of pixels in the cluster was counted. The number of pixels in a cluster alone was not enough to determine the shape, because there could be multiple configurations that had the same pixel count but different shapes. For example, a cluster of 2x2 pixels would have the same pixel count as a cluster of 1x4 pixels. Therefore, the minimal box (bounding box, with width X and height Y) that could cover all these pixels was also calculated. The bounding box ratio was defined as max(X, Y)/min(X, Y), and would be used to distinguish symmetric events from asymmetric events. The area of the bounding

box (X*Y) was also a good measure of the real size of the cluster, and it would be always larger than or equal to the total number of pixels in the cluster.

Figure 59 shows the histograms of the number of pixels in each cluster from ^{55}Fe photon data, and it is clear that most of the events had only 1 or 2 pixels above the threshold. In Figure 60, the 120keV electron hits showed quite a different result, with most events having more than 1 pixel. In fact, the most probable peak was found at 4 pixels per cluster.

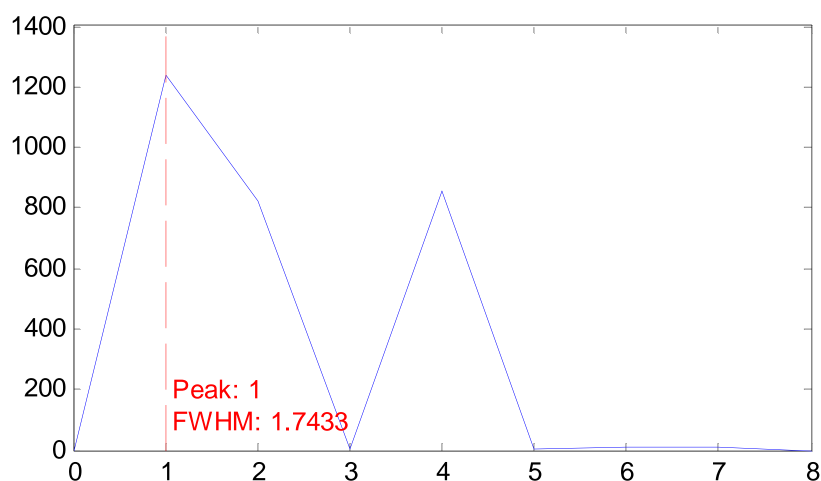

Figure 59. Histogram of the number of pixels in each cluster, from ^{55}Fe photon data in EM5.

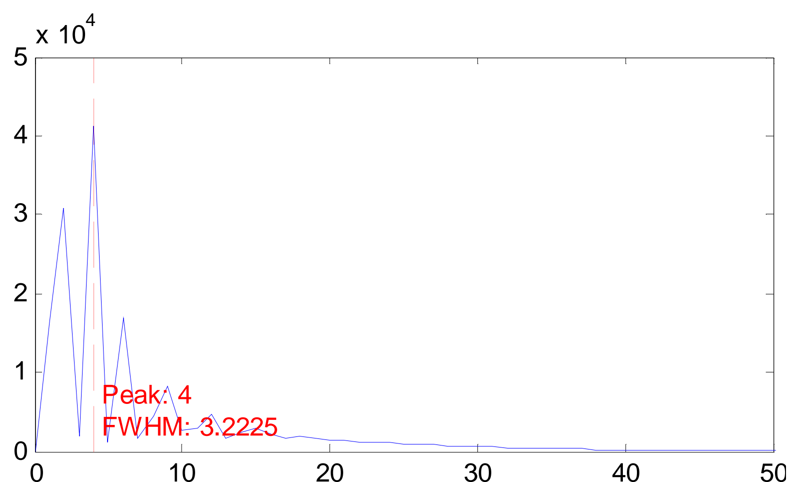

Figure 60. Histogram of the number of pixels in each cluster, from 120keV electrons in EM5.

The histograms of the bounding box ratios obtained from ^{55}Fe photons and 120keV electrons were presented in Figure 61 and Figure 62 respectively. In 120keV events, large and symmetric clusters (with 4 or more pixels in the cluster) tend to have a ratio close to one. In ^{55}Fe events, small and single pixel clusters would also have a ratio of 1. That was why the two histograms looked almost identical.

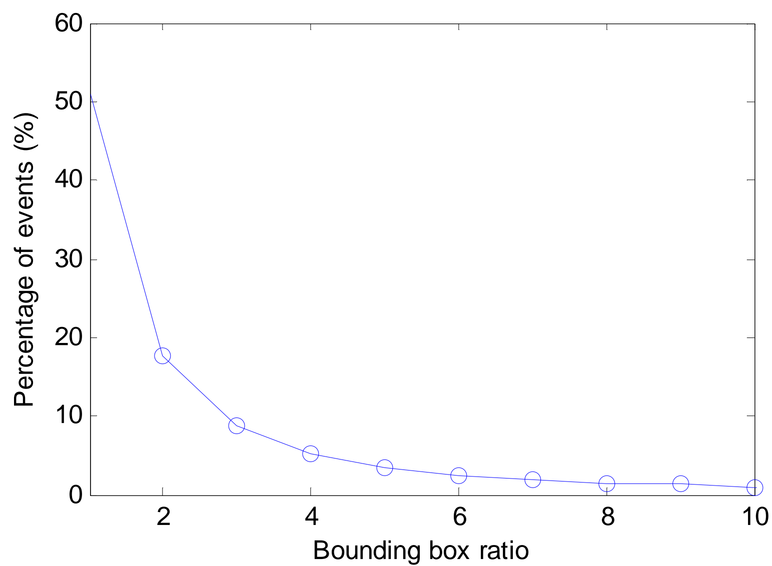

Figure 61. Histogram of the bounding box ratios obtained from ^{55}Fe photon data in EM5.

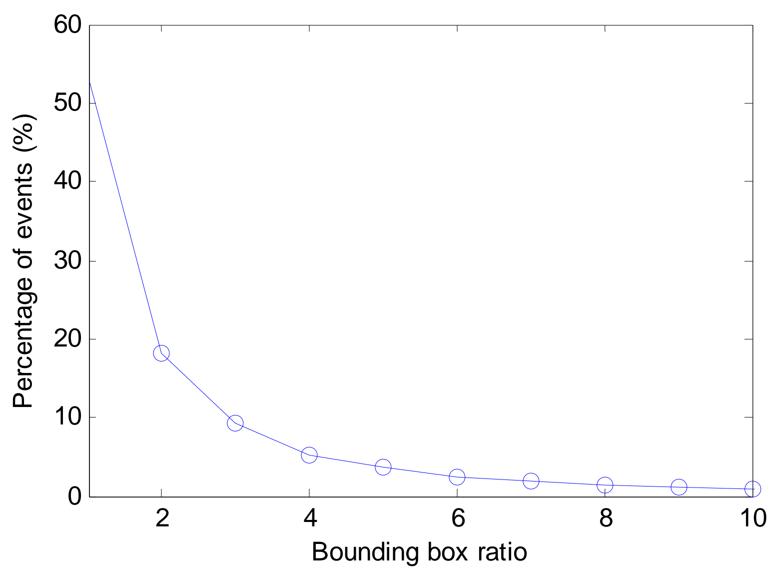

Figure 62. Histogram of the bounding box ratios obtained from 120keV electrons in EM5.

Using the characteristics calculated for each cluster, it was possible to categorize the events from photons or electrons into different groups. A selection rule could be used to filter the clusters to include or exclude specific groups from final image reconstruction.

4.4.3 Image Reconstruction and Super-resolution

The image reconstruction method used in the EM3 was to digitally sum all the frames acquired, so that each pixel contained all the charges integrated over the total integration period. We would call this method "integration method". When operated in the electron counting mode, the EM5 would acquire individual frames just like the EM3. However, the frames were processed to detect single electron hits. Based on the assumption that the pixel that was hit by the incident electron would contain the highest signal, we could reconstruct the final image by using only the peak positions of the detected electron events. In the final image, each pixel would contain only the total counts of the events found in that pixel. If there was no external signal at all, no events would be detected and the final image would contain only zeros.

The signals in the pixels around the center peak pixel in the events might also contain information about the entry point of the incident electron, and it would make it possible to achieve sub-pixel resolution for the incident electron entry point position. A common way to achieve the sub-pixel resolution was to use the centroid of the detected event.

The spatial resolution of the 2-D electron counter relied on the accuracy of finding the positions of incident electron hits. The electron interaction in the epitaxial

layer was more complex than the photon case, so the assumptions about the entry point would need to be re-addressed in the Monte Carlo simulation in Chapter 5.

4.4.4 Noise in the Final Image

The noise contributions in the DDD were outlined in the section 3.2.3, but they were only applicable to the integration imaging method. The detection of single electron hits was performed with a threshold and the readout noise and thermal noise in the system would not affect the final image at all, unless a fake event was counted due to random variations in the noise. With a high signal to noise ratio in EM5, the threshold was high enough that the chance of having fake events were very slim.

A problem with the integration imaging method was that the energy deposited by incident electrons could vary a lot. In fact, the energy deposition in thin silicon layer followed a broad distribution (Landau 1944; Bichsel 1988). The shape of the distribution can be seen in Figure 63, which is a histogram plot of the sum values of the 7x7 matrix around the peak pixels in detected 200keV single electron hits. The large variations would introduce extra noise in low dose images.

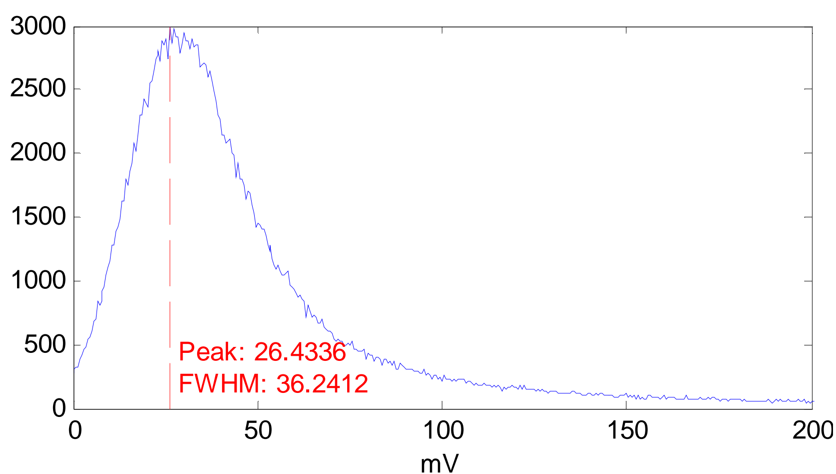

Figure 63. Histogram of the sum values from the 7x7 matrix around the peak pixels of detected single 200keV electron hits.

However, with the electron counting operation, the noise contribution from the variations of the signal shown above would not affect the final image at all, even at low dose imaging conditions. As the incident electron beam dose was kept at a low level, the chances of having two electron hits nearby were minimized. Even if an event deposited 10 times the average energy in the sensor array, that event would be counted still as a single hit, no different from any other event.

In the electron counting mode, the only noise left in the final image would be the shot noise from the incident electron beam, which was an intrinsic noise. As the shot noise was proportional to $\frac{1}{\sqrt{N}}$, the only way to reduce this noise was to increase the total electron dose in the final image, which might not be possible for dose sensitive specimen.

4.4.5 Beam Stop Image using the Electron Counter Mode

To demonstrate the electron counting mode in EM5, an edge image was acquired. For convenience, we used the microscope beam stop to create the edge image, instead of using a metal edge placed on the sensor surface as in EM3.

2500 frames were acquired in the rolling reset CDS mode with a low dose of 0.0048 electrons/pixel/frame or 0.35pA/cm^2. A total of 1578539 electron hits were detected. The final image, shown in Figure 64, was reconstructed using the electron counting method, based on the peak position of each detected event. Five pixels around the edge of sensor were excluded in the single electron detections, corresponding to the thick dark line surrounding the sensor. The dark area represented the area covered by the beam stop, while the bright region was the part of the sensor exposed to the electron beam.

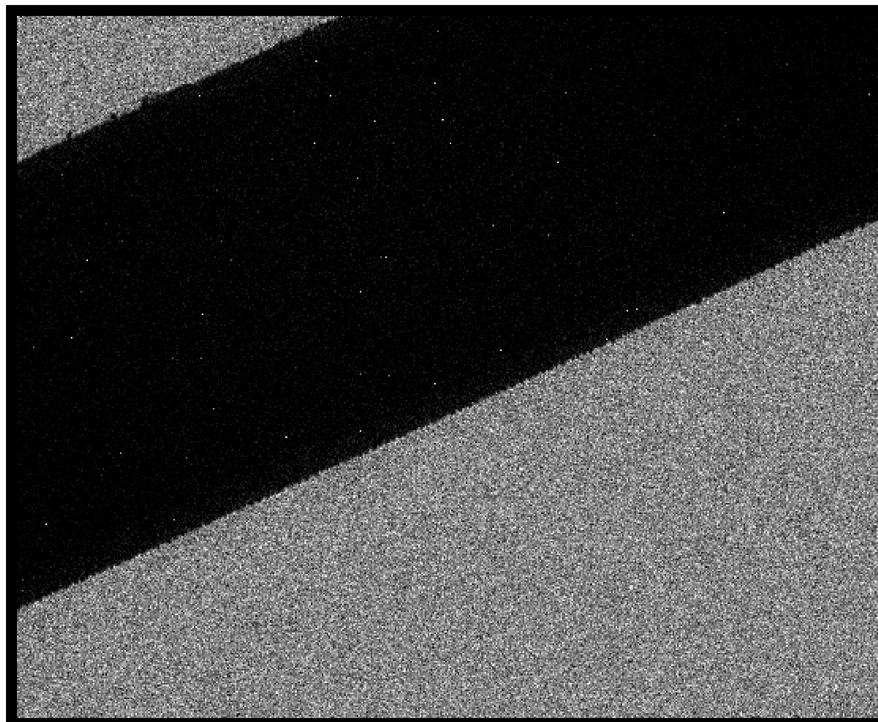

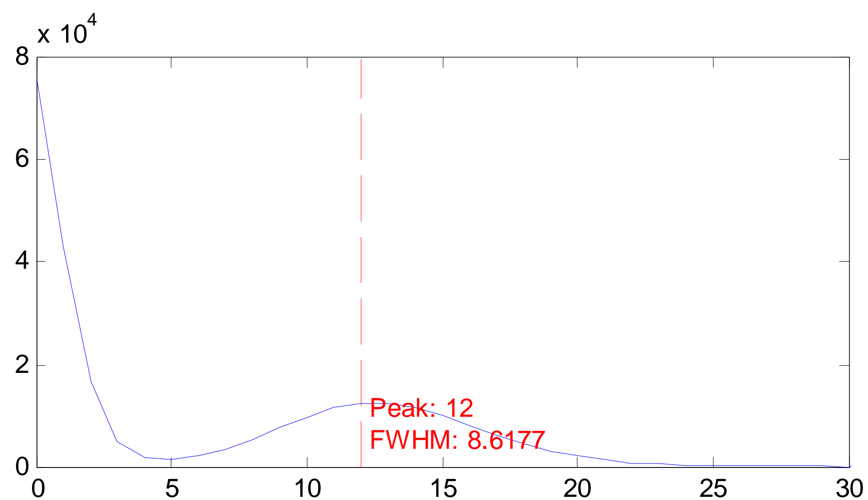

Figure 64. Beam stop image (top) reconstructed using electron counting method at 200keV. The histogram (bottom) of the pixel values in the image was shown at the bottom.

From the histogram in Figure 64, the total number of electron hits detected in the bright region was around 12 electrons/pixel, which agreed well with the expected dose from the measured beam intensity: 0.0048 electrons/pixel/frame x 2500 frames = 12 electrons/pixel. This confirmed that the EM5 was detecting almost every single electron in the incident beam.

The dark region that was covered by the electron beam contained occasional electron hits, and these were likely to be backscattering electrons that entered the EM5 in the bright region, but deflected to the dark region. Some of these events could also come from the X-ray photons generated in the beam stop when the 200keV electrons were absorbed.

4.4.6 MTF Comparison

For comparison purposes, we acquired two datasets using the EM5. The first dataset was acquired using rolling reset CDS mode, with a total dose of 103 electrons/pixel in 250 frames. The second dataset was acquired using single reset diff mode, with a total dose of 120 electrons/pixel in 25000 frames. The two datasets were obtained on the same microscope, with the same beam stop kept in the same position. The beam intensity was lowered in the case of the second dataset to match the total dose per pixel.

Integrating imaging method was used in the first dataset to obtain an edge image and the second dataset was processed using the electron counting method. The method used for MTF calculations in section 3.3.3 was used on both images. Both the edge

spread functions (ESF) and the line spread functions (LSF) for both beam stop images were plotted in Figure 65. The edge transition in the electron counting image was clearly sharper than the one using integration method, which was confirmed in the MTF plot, Figure 66, using the Gaussian fitted LSFs.

a) integrating method

b) electron counting

Figure 65. The line spread functions from the beam stop images using, a) integrating method, b) electron counting method. Data was taken with 200keV electrons.

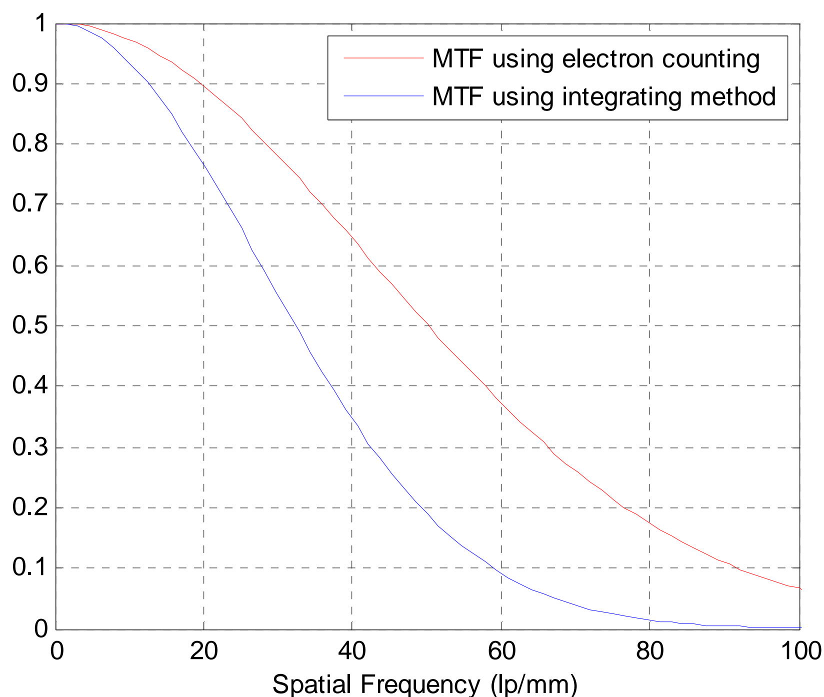

Figure 66. The MTF plots for both the integrating method and the electron counting.

Since we already knew that the EM3 with integrating imaging was already able to surpass any current available scintillation screen based CCD camera system. The electron counting method in EM5 simply made the DDD system even better. The effects of the electron counting on biological images were later presented in Chapter 6.

Chapter 5 Monte Carlo Simulation for DDD

5.1 Monte Carlo Approach to the Electron Transport Problem

As described in the section 2.1.1, the interaction of the electron beam and solid material is a complex problem. Many processes exist and the transport of a single electron in the solid material is a stochastic process, rather than a deterministic process. It is an ideal problem to be studied using the random sampling method in the Monte Carlo approach.

The transport of high energy electrons has been studied extensively in high energy particle physics and several Monte Carlo software packages exist. The most popular ones include GEANT4 (Agostinelli, Allison et al. 2003) and PENELOPE (Salvat, Fernandez-Varea et al. 2003). To use GEANT4 for the electron energy of 120-400keV, one would need to use the additional package of low energy electromagnetic physics (Chauvie, Guatelli et al. 2004), which uses the same cross sections from PENELOPE. Therefore, the two simulation packages would have yielded similar results. The benchmark comparison between the simulation results of PENELOPE and experimental data also confirmed the reliability of the simulation package (Sempau, Fernández-Varea et al. 2003).

In our simulation, the 2008B version of PENELOPE was used.

5.2 Simulation for the EM5

As the scanning electron microscopy images showed us in section 2.1.2, the geometry of the DDD could be modeled by three layers. At the surface of the sensor was 10μm of circuitry, followed by 10μm (for EM5) of epitaxial silicon and then the bulk silicon layer. The total thickness of the device was 300μm.

For simplicity, the geometry of the DDD was defined as three layers of silicon with corresponding thicknesses. As the atomic number and density were the most important factors affecting the simulation, such a simplified model would still be enough to yield realistic results.

To match the charge collection in the DDD, 25 virtual volumes were defined to simulate a 5x5 pixel array. Each virtual volume had a size of 5μm x 5 μm x 10 μm and was placed in the middle layer, which was used to model the epitaxial layer.

The electron beam was normally incident on the top surface. The position of the electron beam was randomly generated within a 5μm x 5 μm area, corresponding to the center virtual volume in the 5x5 array. The electron beam had a single energy, at 120keV or 200keV. At least half a million electrons were simulated for each energy.

The primary electrons or secondary electrons were considered absorbed when their energy dropped down to 50eV. For each simulated event, the location of the entry point as well the energy deposited in each of the 25 virtual volumes were written to a data

file, which was analyzed later on using the same algorithm used in the EM5 single electron hits detection. The same detection threshold was used.

To make the comparison easier, the energy deposited in the virtual volumes was converted to ADC units, based on the photon calibration in EM5 (section 4.2.4).

The average matrix from the simulation at 200keV is shown in Table 9. Comparing to the Table 7 from the EM5, the simulation results showed a much smaller lateral signal spread. In fact, the center pixel value was almost double the experimental value. The sum value of the 5x5 pixel array around the peak was 161 ADC, which did not differ too much from the 5x5 sum from the experimental data (192 ADC).

Table 9. The 5x5 average matrix from the simulation results at 200keV.

0	0	0	0	0
0	2	7	2	0
0	7	125	7	0
0	2	7	2	0
0	0	0	0	0

Similar results were obtained also at 120keV (Table 10). The peak in the simulation results was at 176 ADC, compared to 94 ADC in Table 6. The sum of 5x5 pixels in the simulation results was at 287 ADC, in agreement with the 318 ADC in the experimental data.

Table 10. The 5x5 average matrix from the simulation results at 120keV.

1	1	2	1	1
2	6	16	6	1
2	15	176	15	2
2	6	16	7	2
1	1	2	2	1

The discrepancy of the simulation and the experimental data was actually due to the diffusion process that happens when the ionization electrons generated in the epitaxial layer diffuse to the surface photodiode to be collected (see section 2.1.2). The process was extensively studied by Dr. Shengdong Li using Monte Carlo simulation (Li 2007).

To measure the lateral signal spread due to the diffusion process, one would need to inject ionization electrons at any depth in the epitaxial layer and measure the response in the sensor array. Actually, we had already measured this response in the X-ray photon calibration experiment in section 4.2.4. The cross section of 5.9keV X-ray photon determined that the photoelectric absorption was the dominant interaction for the photon in the epitaxial layer (explained in section 3.2.4). Since the absorption could happen anywhere in the epitaxial layer and on average 1639 ionization electron would be created at the absorption site, the measured response from the sensor array was simply due to the diffusion process.

Taking the measured average matrix from photon events in Table 11, we could convolute it with the average matrices from the simulations. The result for 200keV is shown in Table 11, which is almost a perfect match with the average matrix obtained from experiment. The same agreement was confirmed for 120keV simulation and experimental data.

Table 11. The 5x5 average matrix from the simulation results at 200keV

0	1	1	1	0
1	7	15	7	1
1	15	67	15	1
1	7	15	7	1
0	1	1	1	0

The extra energy deposition detected in the experimental results might have come from contributions due to the ionization electrons that were generated in the silicon substrate and later diffused into the epitaxial layer. This process was not simulated in PENELOPE, so the simulation results would be smaller.

5.3 Faraday Plate Simulation

Using the same simulation framework, we performed a simulation for the Faraday plate collection efficiency and the results were quoted in section 3.1.4.

To illustrate the problem with the backscattering electrons, a few electron trajectories were plotted in Figure 67. The dotted line shows an incident electron that entered the Faraday plate and deflected so much that it exited the surface again. These

escaped electrons would contribute to a systematic error for the beam intensity measured by the Faraday plate.

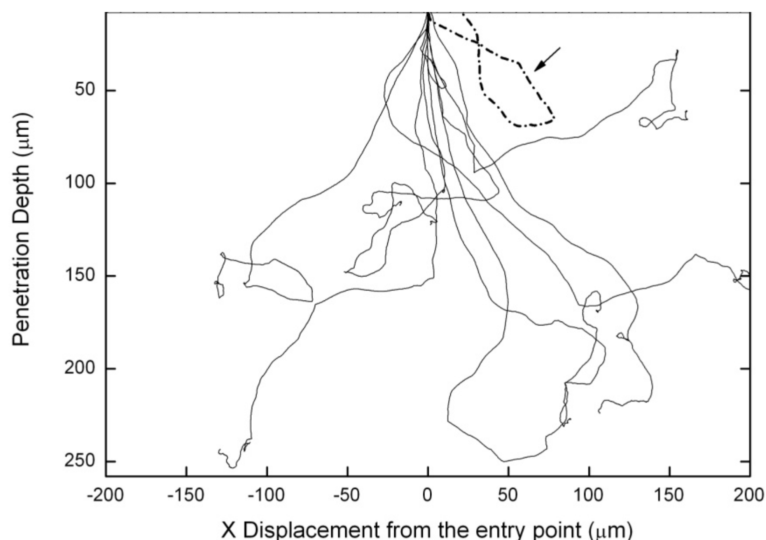

Figure 67. Electron trajectories in aluminum, with a backscattering electron in a dotted line.

The Faraday plate was modeled as an aluminum volume of 1.27 cm x 1.27 cm x 2 mm. The incident electron beam was generated randomly in a box of 1.27 cm x 1.27 cm. One million electrons were simulated for each energy.

At 400keV, 85% was absorbed in the plate, while 11% backscattered and 4% exited the side surfaces. At 300keV, 86% was absorbed, 11.3% backscattered and 2.7% exited the side surfaces. At 200keV, 86% absorbed, 13% backscattered and 1% exited the side. Finally, at 120keV, 86% was absorbed, 13.7% backscattered and less than 0.3% exited the side.

Chapter 6 Applications of DDD

In this chapter, a few examples are given for the applications of the DDD in electron microscopy. The unique features of the DDD make it possible to do specimen drift correction as well as obtaining fast wide-field image mosaics. The comparison between CCD and DDD, as well as the comparison between the integrating imaging and electron counter imaging are also included.

6.1 Image Comparison between CCD and DDD

As an example of the imaging advantages afforded by the DDD, an image of myelin at a magnification of 2500 was taken at 200keV. The myelin layer spacing was about 10 nm, which corresponded to about 25 μm across the myelin band on the detector, i.e. 5 pixels in the EM3. Figure 68 a shows the myelin image. The details of the myelin band are clearly visible. These details were lost on an image (Figure 68 b) of the same sample at the same EM magnification using a high quality cooled fiber coupled CCD camera (2k x 2k Tietz TemCam-F224HD slow scan, 24 μm pixel, 16-bit). The poor spatial resolution of the scintillation screen together with the large pixel size (24 μm) of the CCD made the image very grainy. The DDD image was constructed from a sum of 50 frames taken at a low dose (1.5 electrons/pixel/frame). In total, there were on average 75 incident electrons per pixel. The image demonstrates the high signal-to-noise ratio and the excellent spatial resolution of the new detector.

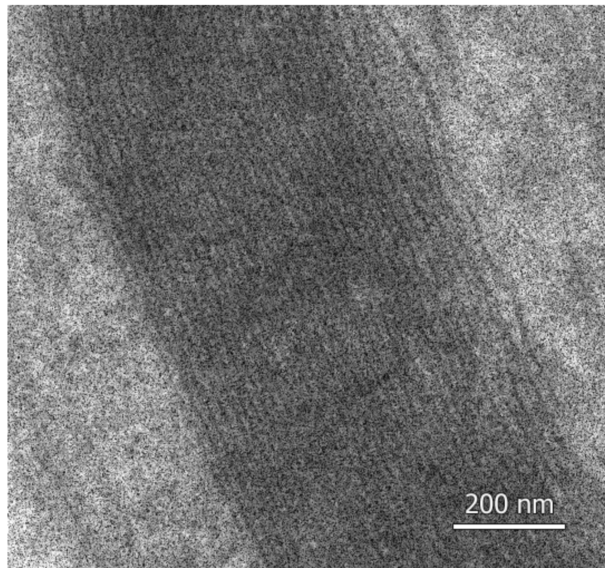

a.

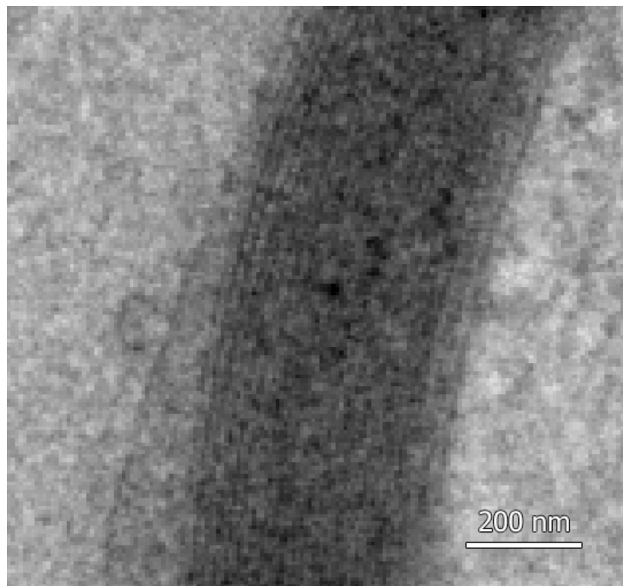

b.

Figure 68. Images of myelin samples from the EM3 (top) and the Tietz 2k x 2k CCD camera (b. Both images were taken at an EM magnification of 2500 with 200 keV electron beam.

6.2 Image Comparison between Integrating Imaging Method and Electron Counting Method

As the MTF comparison in section 4.4.6 indicated, using the DDD with electron counting method would yield better spatial resolution than the normal charge integrating imaging method.

To demonstrate the benefits of the electron counting method, two images were taken on the same specimen (mitochondria) at 5000 magnification. The first image was constructed using the digital integration method from 50 frames in rolling reset CDS mode. The effective integration time was 100ms per frame (5 seconds total acquisition time) and the total electron dose was 63 electrons/pixel in the final image. The second image was constructed using electron counting from 5000 frames in the single read difference mode. The effective integration time was 4.6ms per frame (23 seconds total acquisition time) and the total electron dose was 72 electrons/pixel in the final image.

In Figure 69, the image on the top was the one constructed using the digital integration method. The bottom image from the electron counting showed thinner lines, which appeared more blurry in the top image.

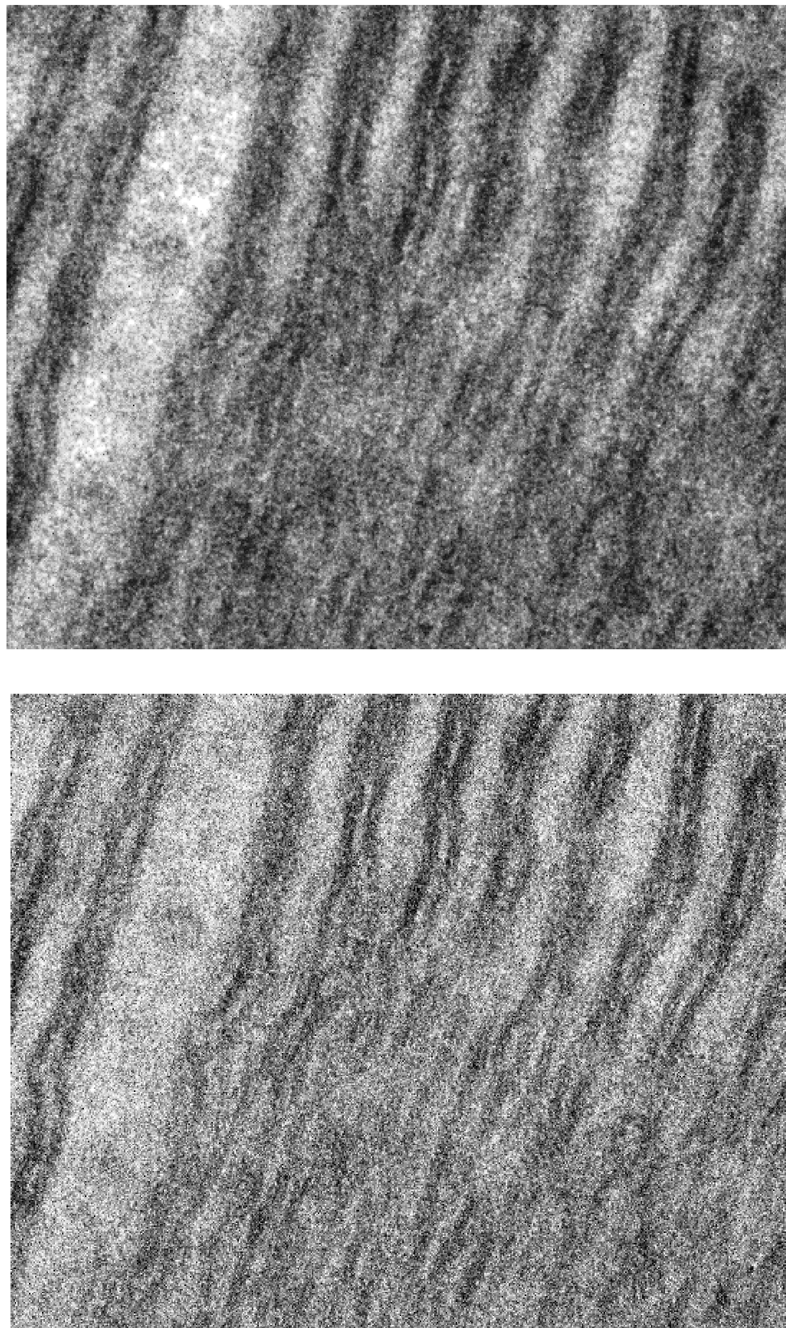

Figure 69. Images of the same specimen using integrating imaging method (top) and electron counting (bottom) method.

6.3 Specimen Drift Correction

In the case of the CCD camera, usually a single image is taken in the duration of a few seconds, the large well capacity of the CCD allowing the signal charge to accumulate in the pixels during the entire exposure time. The process could be called an "analog integration" process.

As for DDD, the limited dynamic range requires the use of digital integration to sum multiple frames to achieve equivalent electron dose in the final image. The higher frame rate in the DDD make this possible, and it also brought about new features that the "analog integration" could not achieve.

One of such features was that the DDD was capable of flexible digital integration. After acquiring a certain amount of images, it is possible for the DDD to choose and use a subset of the frames to do the digital integration. To illustrate the process, 100 frames were acquired using the EM3 for a myelin specimen. Summing up 1, 5, 10, 20, 50, or 100 frames yielded 6 different images, which are shown in Figure 70. In the first image frame, when only 1 frame was used, the noise from the random deposited energy was large, resulting in snow flake type noise corresponding to the electron hits. By summing up 5 or 10 frames, the noise was significantly reduced. By the time we summed up 50 frames, the image quality was almost as good as the one by summing up all the 100 frames. With such a flexible digital integration, we could actually generate 5 images from the same dataset, each from summing up only 20 frames. These 5 images could be then aligned and summed together to yield the final image. Using this method, it is possible to detect and correct for specimen drift.

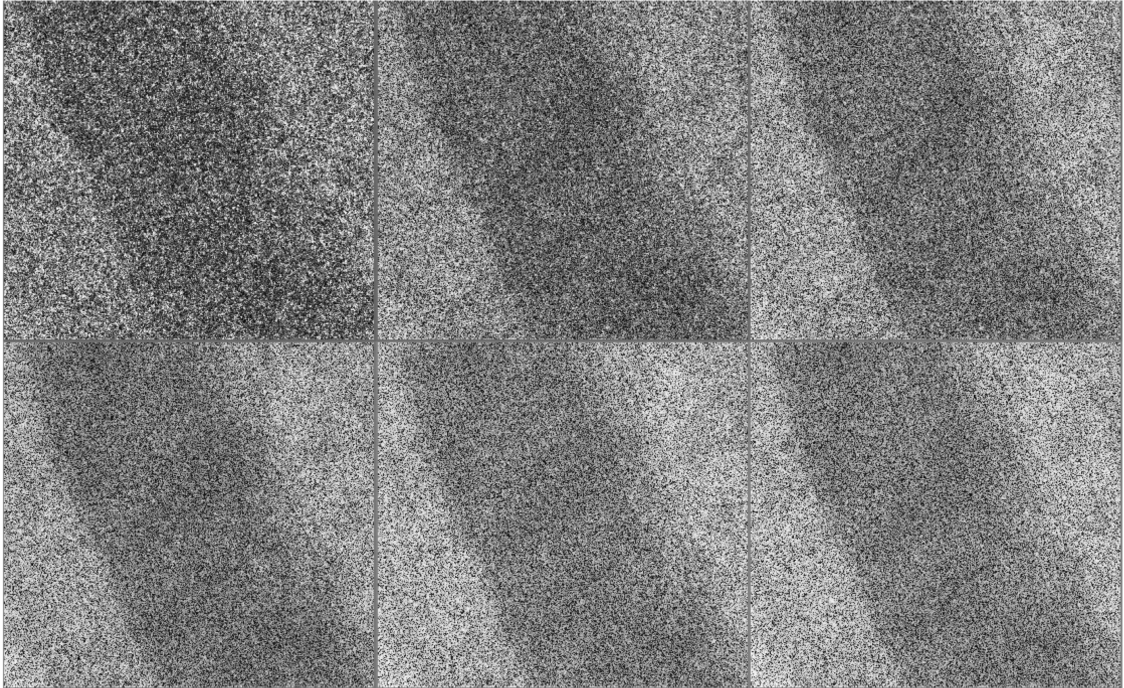

Figure 70. The improvement of image quality by digitally summing up more and more frames. On the first row, 1 frame, 5 frames, and 20 frames were used, and the second row was for 20, 50 and 100 frames (left to right).

Specimen drift is usually observed in electron microscopes at high magnification. It is mostly due to the charging effect on the specimen surface during the beam illumination. The charge build-up can be drastically reduced if a conductive carbon coating is applied. However, even with the carbon coating, specimen drift can still be observed and causes images to blur. It is more of a problem if the exposure time is long.

As an example, 200 individual short exposed frames were obtained using EM3. Every 5 frames were summed together and using the normalized cross correlation function between two subsequent images, we estimated the shift in the x, y direction

(shown in Figure 71). These parameters were then used to align the 5-frame summed images and form the final drift corrected image.

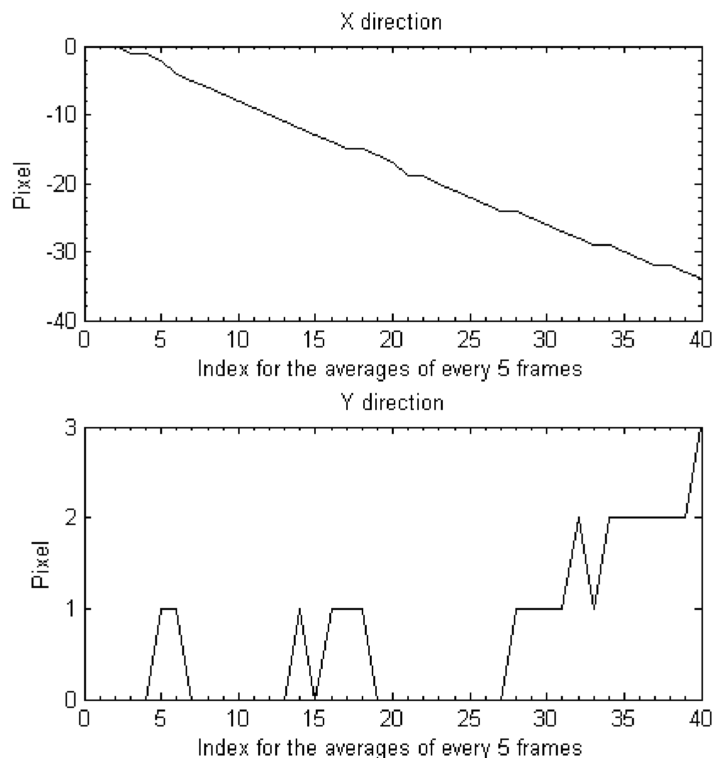

Figure 71. Estimated specimen drift amplitudes in both x- and y- direction of the imaging sensor, calculated using normalized cross correlation applied to the averages of every 5 sequential frames. The x-direction graph shows a substantial drift over time while the y-direction graph shows only slight deviations.

In this experiment, the specimen did not have a carbon coating, so the drift was quite large. The x-direction pixel shifts followed a linear relationship with the frame count (equivalent to the time elapsed). The y-direction pixel shifts were close to zero. Therefore, the observed specimen drift was almost linear along the x-axis of the EM3

sensor and the amplitude of the drift could be deduced from the slope in the x-direction pixel shifts plot.

At high magnifications, the drift correction became more and more important. Any drift during the exposure time of the "analog integration" process in the CCD would simply blur out the details, while the DDD could use the drift correction method to avoid the problem.

6.3.1 Fast Wide-field Mosaic

The high spatial resolution of the DDD indicated that to obtain similar specimen details, the microscope could be operated at much lower magnifications if the DDD was used instead of a CCD camera.

The imaging area of the EM3 prototype was only 2.75 mm x 2.56 mm, very small compared to the total imaging area. Therefore, the DDD system could benefit from the fact that the center of the imaging field has less distortion than the peripheral due to the imperfection of the projection lens of the microscope.

To obtain an image mosaic, the image shift control of the electron microscope optics was utilized to move the electron image around, allowing the EM3 sensor to capture a different area for each exposure. The shift control was carefully set up to ensure an overlap between images, which was used for estimating relative image positions in the final mosaic using normalized cross-correlation. By fixing the first image in a large canvas, all other images were translated according to the relative positions found in the

previous step. A final mosaic image was then assembled. Only x, y translations were considered in the algorithm and no image blending was used for the final mosaic.

As a demonstration, we took 44 images of a 500nm-thick section of mouse cardiac muscle tissue. By manually controlling the image shift of the microscope, each individual image captured a small area, with a 50% overlap region to adjacent images. The final mosaic (Figure 72) was assembled using the steps outlined previously. Although the microscope was operated at a low magnification of only 2500, the myosin bundles were clearly defined within the image.

Since the image shift of the microscope can be easily computer controlled, the entire image mosaic acquisition can be automated and integrated into the process of tomographic data collection. For CCD systems, the same procedure can be used, but the number of images is limited by the range of image shift control. To go beyond the range of the image shift, microscope stage control can be used to further translate the specimen. However, using stage control can create unstable and unpredictable movements which are hard to correct. The waiting time for the stage to stabilize can also add a significant amount of time to the total acquisition for a large mosaic. For a DDD system with the same pixel counts as a CCD system with 15 µm effective pixel size at the same imaging plane, the same range of image shift control on the microscope will provide 8 times more imaging area, due to the small 5 µm pixel size of the DDD system.

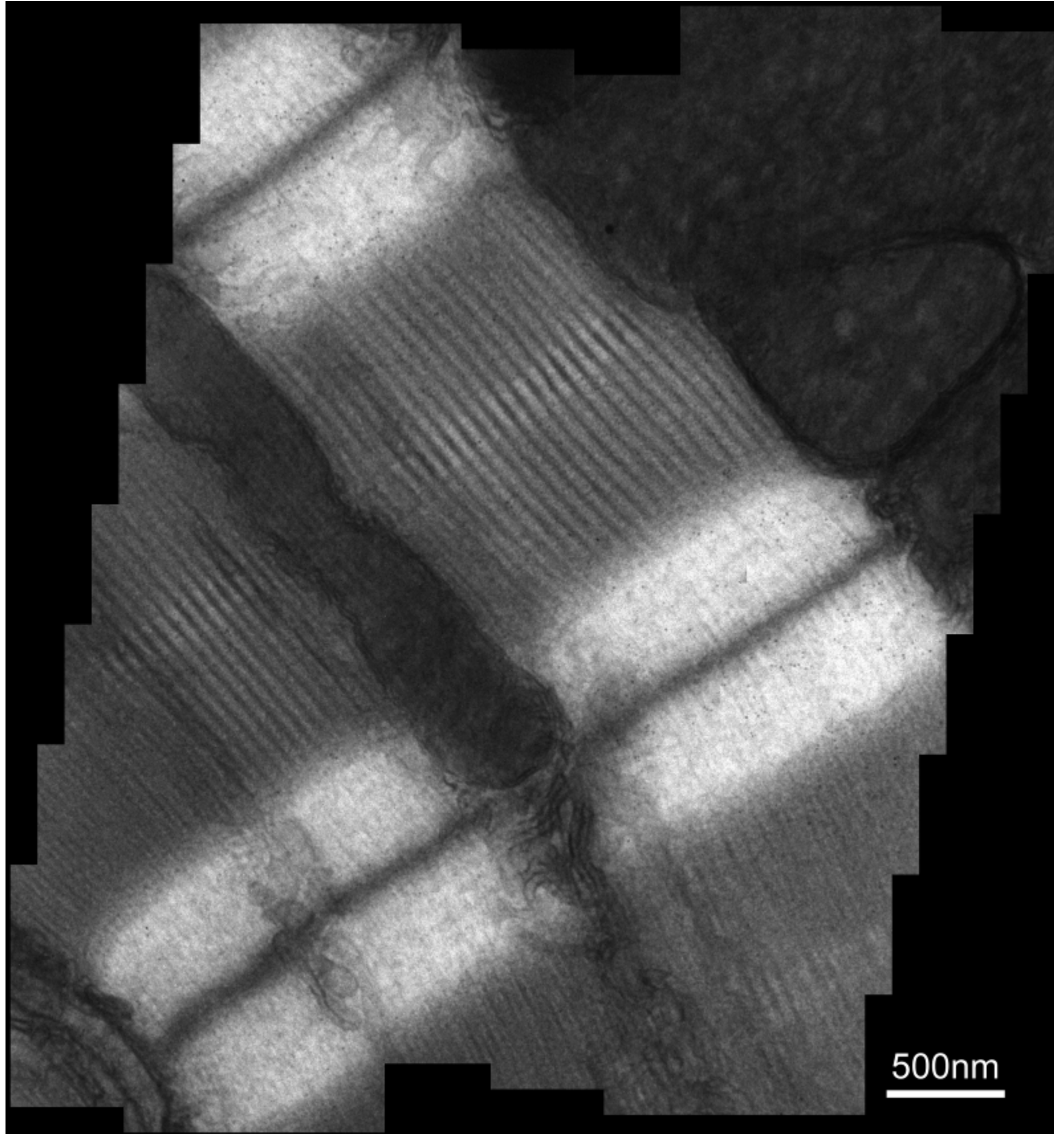

Figure 72. The mosaic image (~2k x 2k) of longitudinal mice cardiac muscle specimen from 44 individual EM3 images, taken at 2500 magnification.

The same image mosaic method was used in conjunction with the electron counting mode in the EM5 to obtain Figure 73. The cross sectional of a mitochondria was imaged at 5000 magnification, combining 27 images. Each image was taken with a total

electron dose of 70 electrons/pixel in 5000 frames using single read difference mode. One of the 27 images is shown in Figure 74.

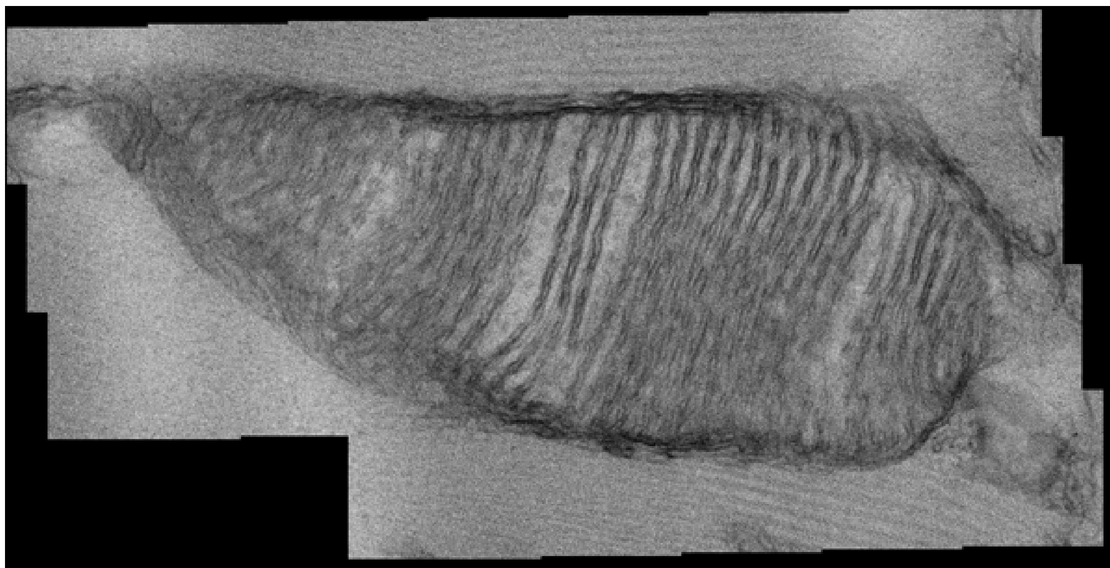

Figure 73. The 1.5k x 3k image mosaic from 27 individual EM5 images constructed using electron counting method.

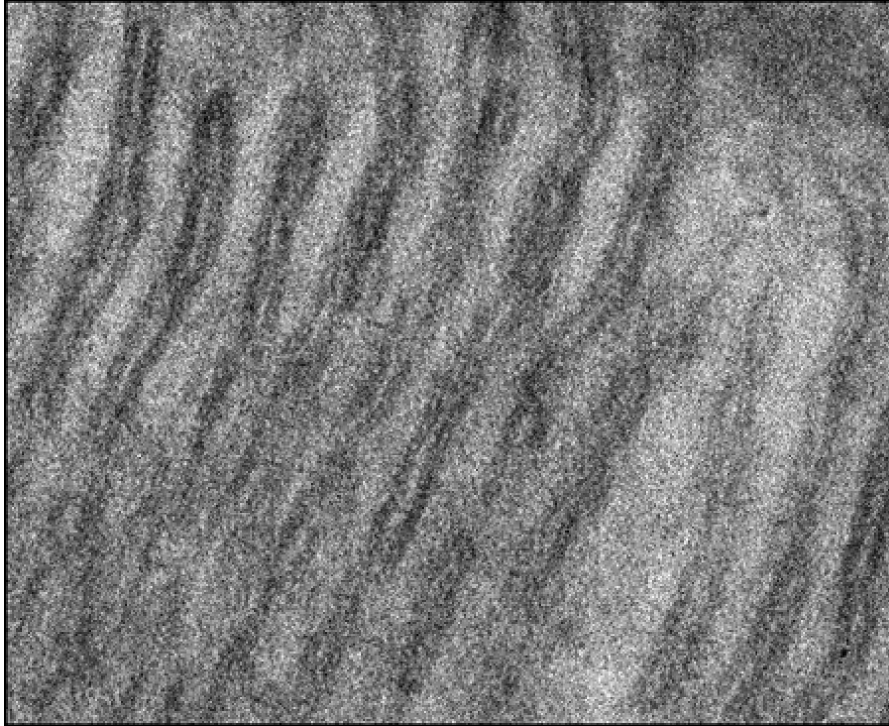

Figure 74. One of the 27 individual images used in the image mosaic in Figure 73.

6.3.2 Electron Tomography

To demonstrate the capability of the Direct Detection Device (DDD) for electron tomography, a dataset was collected using the mouse cardiac muscle specimen.

Using an EM magnification of 5,000x, a single tilt series of 61 images were taken at 1º interval from -30º to +30º. Each image underwent the specimen drift correction procedure before the alignment and reconstruction steps in IMOD (Kremer, Mastronarde et al. 1996). Due to the size of the EM3, the number of gold fiducial particles was not enough for the fiducial alignment step, so only cross-correlation alignment and manual adjustment were applied.

Figure 75 showed a central x-y slice through the reconstructed volume. The myosin bundles appeared as large black dots and the actin filaments were as smaller dots in the cross-sectional region.

By automating image mosaic acquisition at each tilt angle, the DDD system could be an extremely useful tool for large scale structural studies.

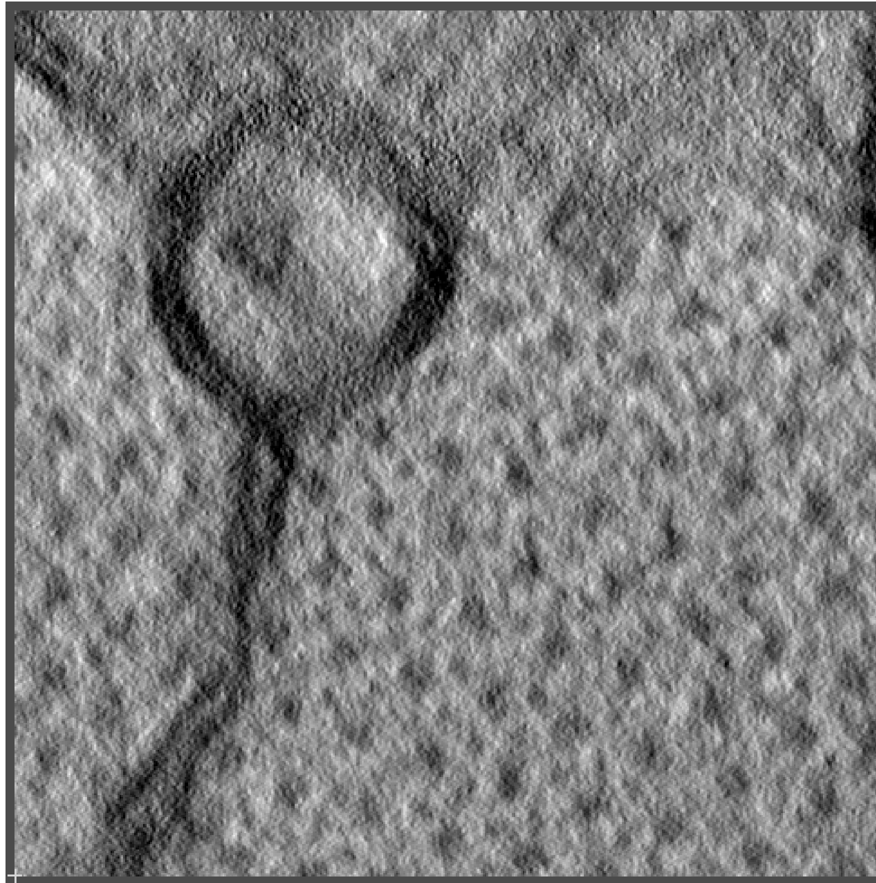

Figure 75. A central x-y slice through the reconstructed cross-sectional cardiac muscle tomographic volume. The total dose at each tile angle is <200 electrons/pixel.

Chapter 7 Summary

7.1 Imaging Benefits from the DDD

Using the DDD system, we have not only proved the feasibility of direct electron detection, but also demonstrated single electron sensitivity and a much improved spatial resolution over scintillator based CCD systems.

The advantages of the DDD are especially important for low dose imaging applications such as cryo-EM. When the electron dose is low, on top of the intrinsic shot noise in the electron image, the variation of energy deposition by the incident electron would introduce extra noise in any sensor that relies on forming the final image by charge integration. Only the electron counting capability of the DDD can reduce this noise. Additionally, when operating the DDD in electron counting mode, the electron beam intensity has to be lowered, which was shown to help reduce the beam induced specimen movement and secondary radiolytic effects such as “bubbling” (Chen, Sachse et al. 2007). With all these benefits, the DDD will help single-particle cryo-EM reach higher resolution.

For electron tomography, the DDD can help reduce the total dose that is needed for a double-tilt or multiple-tilt experiment. The improved signal to noise ratio can also reveal more information in the images. If the DDD image mosaic acquisition can be fully automated, fast wide-field mosaics can be acquired at each tilt angle using only the image shift controls.

7.2 Future Improvements

Referring back to the discussion in section 1.4 about an optimal imaging sensor for TEM, we can see that the DDD system has the potential to fulfill all these requirements. However, for current DDD prototypes, several limitations exist:

Size and Speed: The current DDD prototypes are still small in size compared with current CCD systems. To be more useful, we would need to make a bigger sensor. Unfortunately, with the current DDD design, a larger sensor means lower frame rate. Although specimen drift in modern microscopes are well controlled and drift correction algorithm could be applied, the total image acquisition cannot be too long. Ways to redesign the DDD to achieve high frame rate even with a large size would need to be explored. Higher frame rate will also bring the larger dynamic range, which would make DDD better suited for high-dose applications in materials science.

Spatial Resolution and Wide Field: The backscattering events from the silicon substrate could also be eliminated if the sensor chip was first back-thinned and illuminated from the backside. From Monte Carlo simulation, backside illumination will help with the spatial resolution a little bit. To gain even further improvements in spatial resolution, the pixel size and the thickness of the epitaxial layer would need to be optimized. It is likely that we can use a smaller pixel size, which would be good for wide-field imaging as it will increase the total pixel count in the same imaging area.

References

Agostinelli, S., J. Allison, K. Amako, J. Apostolakis, H. Araujo, P. Arce, M. Asai, D. Axen, S. Banerjee and G. Barrand (2003). "GEANT4—a simulation toolkit." Nuclear Inst. and Methods in Physics Research, A **506**(3): 250-303.

Aikens, R., D. Agard and J. Sedat (1989). "Solid-state imagers for microscopy." Methods Cell Biol **29**: 291-313.

Anelli, G., M. Campbell, M. Delmastro, F. Faccio, S. Floria, A. Giraldo, E. Heijne, P. Jarron, K. Kloukinas and A. Marchioro (1999). "Radiation tolerant VLSI circuits in standard deep submicron CMOStechnologies for the LHC experiments: practical design aspects." Nuclear Science, IEEE Transactions on **46**(6): 1690-1696.

Berger, M. and P. Laboratory (1998). Stopping-power and Range Tables for Electrons, Protons, and Helium Ions, NIST Physics Laboratory.

Bichsel, H. (1988). "Straggling in thin silicon detectors." Reviews of Modern Physics **60**(3): 663.

Bottcher, B., S. A. Wynne and R. A. Crowther (1997). "Determination of the fold of the core protein of hepatitis B virus by electron cryomicroscopy." Nature **386**(6620): 88-91.

Chapman, J., A. Craven and C. Scott (1989). "Electron detection in the analytical electron microscope." Ultramicroscopy **28**: 108-117.

Chauvie, S., S. Guatelli, V. Ivanchenko, F. Longo, A. Mantero, B. Mascialino, P. Nieminen, L. Pandola, S. Parlati and L. Peralta (2004). Geant4 low energy electromagnetic physics.

Chen, J., C. Sachse, C. Xu, T. Mielke, C. Spahn and N. Grigorieff (2007). "A dose-rate effect in single-particle electron microscopy." Journal of structural biology.

Claus, G., C. Colledani, W. Dulinski, D. Husson, R. Turchetta, J. L. Riester, G. Deptuch, G. Orazi and M. Winter (2001). "Particle tracking using CMOS monolithic active pixel sensor." Nuclear Inst.and Methods in Physics Research, A **465**(1): 120-124.

Crowther, R., D. DeRosier and A. Klug (1970). "The Reconstruction of a Three-Dimensional Structure from Projections and its Application to Electron Microscopy." Proceedings of the Royal Society of London. Series A, Mathematical and Physical Sciences (1934-1990) **317**(1530): 319-340.

Danchenko, V., U. Desai and S. Brashears (1968). "Characteristics of Thermal Annealing of Radiation Damage in MOSFET's." Journal of Applied Physics **39**: 2417-2424.

De Ruijter, W. J. and J. K. Weiss (1992). "Method to measure properties of slow-scan CCD cameras for electron microscopy." Rev.Sci.Instrum **63**: 4314-4321.

Fan, G. and M. Ellisman (1996). "Optimization of thin-foil based phosphor screens for CCD imaging in TEM in the voltage range of 80-400 kV." Ultramicroscopy(Netherlands) **66**(1): 11-19.

Fan, G. Y. and M. H. Ellisman (2000). "Digital imaging in transmission electron microscopy." Journal of microscopy **200**(Pt 1): 1-13.

Faruqi, A., R. Henderson and L. Tlustos (2005). "Noiseless direct detection of electrons in Medipix2 for electron microscopy." Nuclear Inst. and Methods in Physics Research, A **546**(1-2F): 160-163.

Faruqi, A. R. and H. N. Andrews (1997). "Cooled CCD camera with tapered fibre optics for electron microscopy." Nuclear Instruments and Methods in Physics Research Section A: Accelerators, Spectrometers, Detectors and Associated Equipment **392**(1): 233-236.

Frank, J. (1992). Electron Tomography: Three-dimensional Imaging with the Transmission Electron Microscope, Plenum Pub Corp.

Frank, J. (2006). Three-dimensional electron microscopy of macromolecular assemblies: visualization of biological molecules in their native state, Oxford University Press, USA.

Frank, J., P. Penczek, R. K. Agrawal, R. A. Grassucci and A. B. Heagle (2000). "Three-dimensional cryoelectron microscopy of ribosomes." Methods in enzymology **317**: 276-291.

Henderson, R. (2004). "Realizing the potential of electron cryo-microscopy." Quarterly reviews of biophysics **37**(01): 3-13.

Janesick, J., J. T. Andrews and T. Elliott (2006). "Fundamental performance differences between CMOS and CCD imagers: Part 1." Proceedings of SPIE **6276**: 62760M.

Jin, L., A.-C. Milazzo, S. Kleinfelder, S. Li, P. Leblanc, F. Duttweiler, J. C. Bouwer, S. T. Peltier, M. Ellisman and N.-H. Xuong (2007). The intermediate size direct detection detector for electron microscopy. Sensors, Cameras, and Systems for Scientific/Industrial Applications VIII, San Jose, CA, USA, SPIE.

Jin, L., A. C. Milazzo, S. Kleinfelder, S. Li, P. Leblanc, F. Duttweiler, J. C. Bouwer, S. T. Peltier, M. H. Ellisman and N. H. Xuong (2008). "Applications of direct detection device in transmission electron microscopy." J Struct Biol **161**(3): 352-8.

Kremer, J. R., D. N. Mastronarde and J. R. McIntosh (1996). "Computer visualization of three-dimensional image data using IMOD." Journal of structural biology **116**(1): 71-76.

Krivanek, O., P. Mooney, G. Fan, M. Leber and C. Meyer (1991). Slow-scan CCD cameras for transmission electron microscopy, Institute of Physics Publishing.

Landau, L. (1944). "On the Energy Loss of Charged Particles by Ionization." J. Physics **8**: 201.

Lata, R., J. F. Conway, N. Cheng, R. L. Duda, R. W. Hendrix, W. R. Wikoff, J. E. Johnson, H. Tsuruta and A. C. Steven (2000). "Maturation Dynamics of a Viral Capsid Visualization of Transitional Intermediate States." Cell **100**(2): 253-263.

Leyris, C., F. Martinez, M. Valenza, A. Hoffmann, J. Vildeuil and F. Roy (2006). Impact of Random Telegraph Signal in CMOS Image Sensors for Low-Light Levels.

Li, S. (2007). Modeling, Design, and Analysis of Monolithic Charged-particle Image Sensors, University of California, Irvine.

McEwen, B. and J. Frank (2001). "Electron tomographic and other approaches for imaging molecular machines." Current Opinion in Neurobiology **11**(5): 594-600.

Meyer, R. R. and A. I. Kirkland (2000). "Characterisation of the signal and noise transfer of CCD cameras for electron detection." Microscopy research and technique **49**(3): 269-280.

Milazzo, A. C., P. Leblanc, F. Duttweiler, L. Jin, J. C. Bouwer, S. Peltier, M. Ellisman, F. Bieser, H. S. Matis, H. Wieman, P. Denes, S. Kleinfelder and N. H. Xuong (2005). "Active pixel sensor array as a detector for electron microscopy." Ultramicroscopy **104**(2): 152-9.

Roberts, P. T. E., J. N. Chapman and A. M. MacLeod (1982). "A CCD-based image recording system for the CTEM." Ultramicroscopy **8**: 385-396.

Ruska, E. (1987). "The development of the electron microscope and of electron microscopy." Reviews of Modern Physics **59**(3): 627-638.

Salvat, F., J. Fernandez-Varea, E. Acosta and J. Sempau (2003). PENELOPE: A Code System for Monte Carlo Simulation of Electron and Photon Transport, Nuclear Energy Agency, Organisation for Economic Co-operation and Development.

Sempau, J., J. Fernández-Varea, E. Acosta and F. Salvat (2003). "Experimental benchmarks of the Monte Carlo code penelope." Nuclear Inst. and Methods in Physics Research, B **207**(2): 107-123.

Speir, J. A., S. Munshi, G. Wang, T. S. Baker and J. E. Johnson (1995). "Structures of the native and swollen forms of cowpea chlorotic mottle virus determined by X-ray crystallography and cryo-electron microscopy." Structure (London, England : 1993) **3**(1): 63-78.

Spence, J. and J. Zuo (1988). "Large dynamic range, parallel detection system for electron diffraction and imaging." Review of Scientific Instruments **59**: 2102.

Thuman-Commike, P. A. and W. Chiu (2000). "Reconstruction principles of icosahedral virus structure determination using electron cryomicroscopy." Micron (Oxford, England : 1993) **31**(6): 687-711.

Turchetta, R., J. D. Berst, B. Casadei, G. Claus, C. Colledani, W. Dulinski, Y. Hu, D. Husson, J. P. Le Normand and J. L. Riester (2001). "A monolithic active pixel sensor for charged particle tracking and imaging using standard VLSI CMOS technology." Nuclear Inst.and Methods in Physics Research, A **458**(3): 677-689.

Wang, X., P. Rao, A. Mierop and A. Theuwissen (2006). Random Telegraph Signal in CMOS Image Sensor Pixels.

Weickenmeier, A. L., W. Nüchter and J. Mayer (1995). "Quantitative characterization of point spread function and detection quantum efficiency for a YAG scintillator slow scan CCD camera." Optik(Stuttgart) **99**(4): 147-154.

Xuong, N. H., L. Jin, S. Kleinfelder, S. Li, P. Leblanc, F. Duttweiler, J. C. Bouwer, S. T. Peltier, A. C. Milazzo and M. Ellisman (2007). "Future directions for camera systems in electron microscopy." Methods Cell Biol **79**: 721-39.

Xuong, N. H., A. C. Milazzo, P. LeBlanc, F. Duttweiler, J. Bouwer, S. Peltier, M. Ellisman, P. Denes, F. Bieser and H. S. Matis (2004). "First use of a high-sensitivity active pixel sensor array as a detector for electron microscopy." Proceedings of SPIE **5301**: 242.